Aspects of the lithium–sulphur dioxide cell

ASPECTS OF THE LITHIUM-SULPHUR
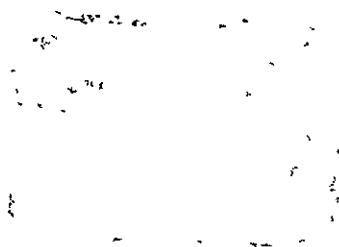DIOXIDE CELL

BY

NEIL FRANCIS HARMAN

A Doctoral Thesis submitted in partial fulfilment of the requirements
for the award of Doctor of Philosophy of the Loughborough University
of Technology.

December 1986

The work described in this thesis has not been submitted, in full or in part, to this or any other institution for a higher degree.

SUMMARY

An open electrolytic cell has been designed and constructed
for use in a dry environment. This was used to investigate the
passivation processes concerned with both the lithium and the
carbon (SO_2) electrodes.

A.c. impedance techniques have been used in both two and
three terminal cell systems in order to study the kinetics of the
electrode processes. Effects of temperature, state-of-charge and
reverse cell operation have been studied.

Computer simulations were made of the growth of crystals on a
flat (Li) surface and the resulting growth transients connecting
current and time were derived. This model was extended to simulate
the porous carbon (SO_2) electrode and the utilisation of the carbon
as a function of the depth of reaction penetration into the
electrode is devised for both potentiostatic and galvanostatic
discharging.

ACKNOWLEDGEMENTS

"Μηδείς ἀγεωμέτρητος εἰσίτω."

ΠΥΘΑΓΟΡΑΣ

CONTENTS

LIST OF SYMBOLS

A	Helmholtz free energy
A	nucleation rate constant
A, A_o	electrode surface area
A	pre-exponential factor
a	ratio of height to radius for a cone
C_i^*	bulk concentration of species i
C_o	bulk concentration
$C_i(z,t)$	concentration of species i distance z from the electrode surface at time t
C_L, C_{dL}	overall double-layer differential capacitance
C_{fixed}	differential capacitance corresponding to a fixed layer
$C_{diffuse}$	differential capacitance corresponding to a diffuse layer
D, D_i	diffusion coefficients
D_C	dielectric constant of diffuse layer
D_D	dielectric constant of compact layer
E	potential measured from reference potential
E_o	reversible electrode potenital
E^*	characteristic potential
$E^\ominus$	standard electrode potential
e	a.c. potential
F	Faraday constant
f	frequency
H	height of cylindrical crystals
i	$\sqrt{-1}$
i_a	anodic current density
i_c	cathodic current density
i_o	exchange current density
J_i	flux of species i
j	$\sqrt{-1}$
k, k_b, k_f, k_L	rate constants
k_f^o, k_b^o	values of k_f, k_b at the reference potential
k^o	rate constant at standard electrode potential
k', k_f', k_b'	pre-exponential factors for k^o, k_f^o, k_b^o
M	relative molecular mass of crystal deposit

M, M_{ads}^{n+}, MX_n	number of the appropriate species
N_i	number of moles of species i
N_o	number of nuclei
n	number of electrons transferred
O, Ox	oxidised species
$P(\ )$	probability of a given event
R, r	radii of growing crystals
R	gas constant
R, Red	reduced species
R_{ct}	charge transfer resistance
R_e	solution resistance
R_{dc}	resistance at D.C. point
S	entropy
S	surface area of a sphere
S_{cap}	surface area of a spherical cap
S_{ext}	fractional extended surface area
T	absolute temperature
t_p	passivation time
u	age of nuclei
V	total volume of overlapped crystals
V_o	total volume of space
V_{ex}	extended volume of crystals (neglecting overlap)
V_2	velocity of growth
x	height above electrode surface
x	depth into electrode
x_o	total depth of electrode
$Z(\omega)$	impedance as a function of frequency
α	charge transfer coefficient
β	charge transfer coefficient for cathodic process.
ΔE	amplitude of a.c. potential
ΔH^a	activation enthalpy at standard electrode potential
ΔH_f^a	activation enthalpy for the forward reaction
ΔH_b^a	activation enthalpy for the backward reaction
ΔI	amplitude of a.c. current
ΔU^{act}	activation energy at constant volume
δ_n	thickness of Nernst layer
ζ	zeta potential
η	overpotential

η	expected fractional coverage
η_D	diffusion overvoltage
η_t	charge transfer overvoltage $(E-E_o)$
θ	charge transfer resistance
θ_{cov}, θ_{uncov}	covered and uncovered surface areas
μ	mean number of nuclei
ξ	surface area of electrode
ρ	density
ν	kinematic viscosity
ω	angular frequency
ϕ	phase lag
ϕ	potential at various points in the double layer

CHAPTER 1

INTRODUCTION

In the late 1950's and early 1960's with the advent of the space programme the need for high energy density batteries became of prime importance. As lithium has the most negative standard electrode potential,

$$E^\ominus : \quad Li^+ + e^- \rightleftharpoons Li, \quad -3.045 \text{ V at } 25°C \qquad (1.1)$$
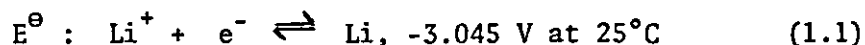
and is the lightest metal, a system based on the lithium anode seemed an obvious choice.

A major problem was the high reactivity of lithium metal, especially with aqueous systems, making the choice of electrolyte and other cell components difficult.

The electrolyte had to be chemically stable with respect to both lithium and the cathode material. A high conductivity was also essential, for the cell to be comparable in performance with contemporary aqueous systems. Although a number of non-aqueous electrolyte solutions were found to have sufficient conductivity, if a suitable solute was used, most combinations were unstable with respect to the lithium anode.

For the few cases which were found to be viable, their stability was attributed to the formation of a protective film on the lithium electrode surface.

For any choice of cathodic reactant the same stability criterion had to be applied. A number of such reactants were identified [1].

Several systems are in current manufacture. The best of the high rate discharge combinations are Li/SO Cl$_2$ and Li/SO$_2$. The Li/SO$_2$ system, is the subject of the discussion presented here.
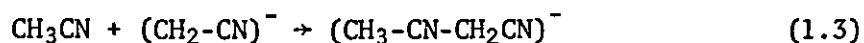
Sulphur dioxide is a good choice as a cathode reactant because of its low equivalent weight, high potential with respect to lithium metal, and relatively low cost. The cell system also performs well over a wide temperature range (-40°C → 70°C).

The technology for the Li/SO$_2$ system was patented in 1969 and 1971 [2,3] and the first practical cells appeared in the early 1970's.

The SO_2 cathode reactant is also a necessary constituent of the electrolyte and facilitates the conductivity of solutions by the relatively high dielectric constant. It is also responsible for the stability of the lithium electrode due to the formation of a film of lithium dithionite ($Li_2S_2O_4$) at the lithium/electrolyte surface [4,5]. The film forms instantly when lithium is introduced to an SO_2 containing solvent.

The aprotic organic cosolvent for the SO_2 considered in this thesis is acetonitrile (CH_3CN), although propylene carbonate has also been used [1].

In the absence of SO_2, acetonitrile reacts with lithium metal according to the following reactions [6] :

$$2Li + 2CH_3CN \rightarrow (CH_2\text{-}CN)^- + Li^+ + CH_4 + LiCN \qquad (1.2)$$

$$CH_3CN + (CH_2\text{-}CN)^- \rightarrow (CH_3\text{-}CN\text{-}CH_2CN)^- \qquad (1.3)$$

SO_2 inhibits these reactions by sharing the non-bonding electrons of the acetonitrile molecule and also by the formation of a passive film on the lithium. The addition of propylene carbonate is also reported to retard these reactions [7].

Lithium salts are added to the electrolyte solution which by dissolving and ionizing increases the conductivity. LiBr provides the best conductivity of the useful salts and is fairly inexpensive.

LiBr is known to react with SO_2 in these electrolyte solutions according to the following reactions [8]

$$8LiBr + 8SO_2 \rightarrow 4Li_2SO_3 + 4SOBr_2 \qquad (1.4)$$

$$4SOBr_2 \rightarrow 2SO_2 + S_2Br_2 + 3Br_2 \qquad (1.5)$$

$$4Li_2SO_3 + 2Br_2 \rightarrow 2Li_2SO_4 + 4LiBr + 2SO_2 \qquad (1.6)$$
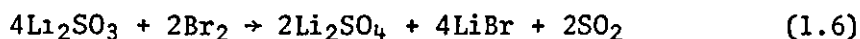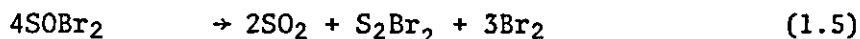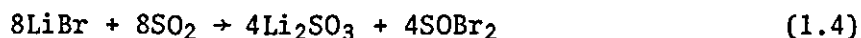
which gives the total reaction

$$4LiBr + 4SO_2 \rightarrow 2Li_2SO_4 + S_2Br_2 + Br_2 \qquad (1.7)$$
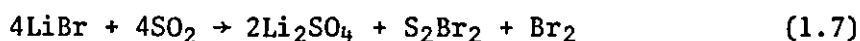
Despite these reactions the Li/SO_2 cell systems have exceptional stability with reported shelf-lives limited only by the short history of the cells.

The cell discharge reaction is generally accepted as [9]

$$2Li \rightarrow 2Li^+ + 2e^- \qquad (1.8)$$

at the anode and

$$2e^- + 2SO_2 \rightarrow S_2O_4^{2-} \qquad (1.9)$$

at the cathode.

The dithionite ion $S_2O_4^{2-}$ is thought to form by dimerization of the SO_2^- radical thus [10]

$$SO_2 + e^- \rightarrow SO_2^- \qquad (1.10)$$

$$2SO_2^- \rightarrow S_2O_4^{2-} \qquad (1.11)$$

The $S_2O_4^{2-}$ then reacts with the Li^+ ions in solution to form insoluble solid $Li_2S_2O_4$ in the pores of the carbon matrix which is used as the inert current collector.

The only cloud on the horizon of lithium sulphur dioxide cells is the poor safety record and this has prevented the wide acceptability of these cells to the present time.

The safety hazards stem from the reactivity and toxicity of the cell contents and the need for cell pressurization. Cells are fabricated with a built-in safety vent in the cell casing which should open and release any internal pressure build up; however, a very sudden pressure increase may still result in explosion. Cells may vent or explode if short-circuited, discharged at a very high rate, overdischarged, charged or heated.

In the first part of this thesis an examination is reported of the whole manufactured cells using a.c. impedance techniques. Further the work is continued to study the passivation of both the lithium and carbon in an open cell system.

In the next section the electrocrystallization of the lithium dithionite on the carbon matrix will be considered. Firstly the general electrocrystallization will be examined and current-time transients derived for three dimensional growth on a flat surface leading to passivation. Finally the porous properties of the carbon using a macrohomogeneous model will be considered and the electrometric responses mathematically simulated.

CHAPTER II

THEORETICAL PRINCIPLES

2.1 The Electrode-Electrolyte Interphase

At the interphase between any pair of conducting   phases there
exists a potential difference the magnitude of which is dependent on
the composition and nature of the two phases.

There are many types of such interphase, but the one we are
concerned with here is that between an electrode and the surrounding
electrolyte solution. The structure of this interphase is of
fundamental importance in electrochemistry as it determines the way
in which electrode reactions proceed.

If we were only interested in the equilibrium properties of this
interphase we could determine the interfacial potential from
thermodynamic principles and there would be no need to know about the
structure of the charge separation. We are, however, interested in
electrode kinetics and the flow of current between the electrode
and solution and to describe this dynamical situation requires
modelling the microscopic structure of the interphase.

The earliest and most primitive model was given by Helmholtz [11]
in 1879 who suggested a layer of ions at the solid surface and a
rigidly held layer of oppositely charged ions in the solution, this
is known as the 'electrical double layer' or just 'double layer'.
This Helmholtz double layer is equivalent to a simple parallel plate
capacitor, see fig. 2.1. This model is basically inadequate because
although the charge on the electrode is confined to the surface the
same is not true of the solution as the thermal motions of liquid
molecules would not sustain a rigid array of charges at the
interphase.

Gouy [12] and Chapman [13] proposed the theory of a diffuse
double layer with a statistical distribution of ions in the electric
field, see fig. 2.2.

There is however a serious defect in the Gouy-Chapman theory in
that it treats the ions as point charges and this leads to very high
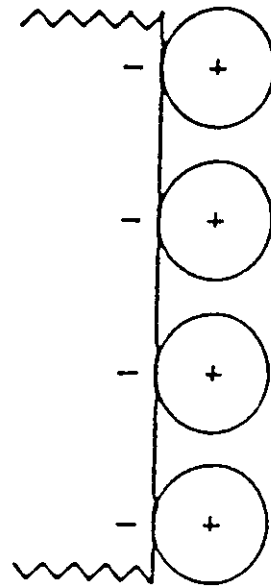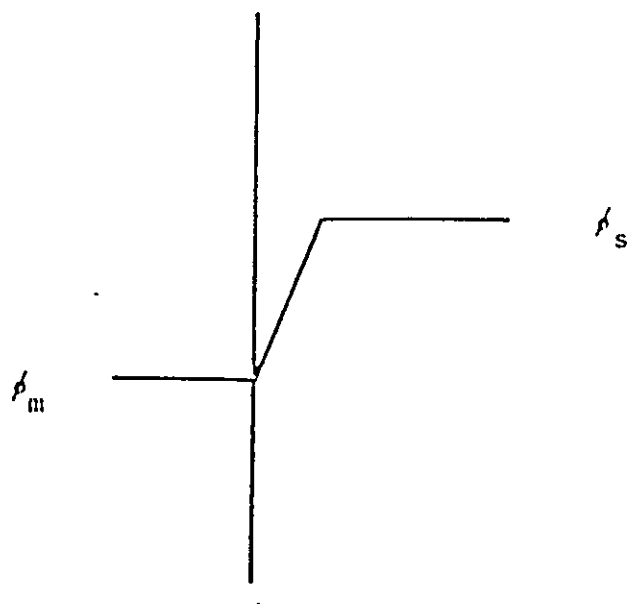values for the charge concentration in the immediate neighbourhood

FIG. 2.1. HELMHOLTZ MODEL OF THE DOUBLE LAYER.

VARIATION OF POTENTIAL WITH DISTANCE THROUGH THE
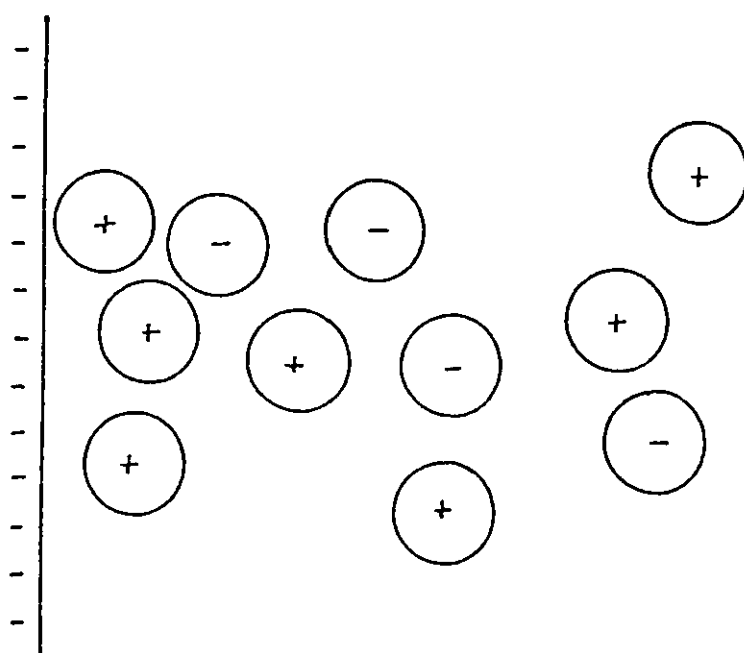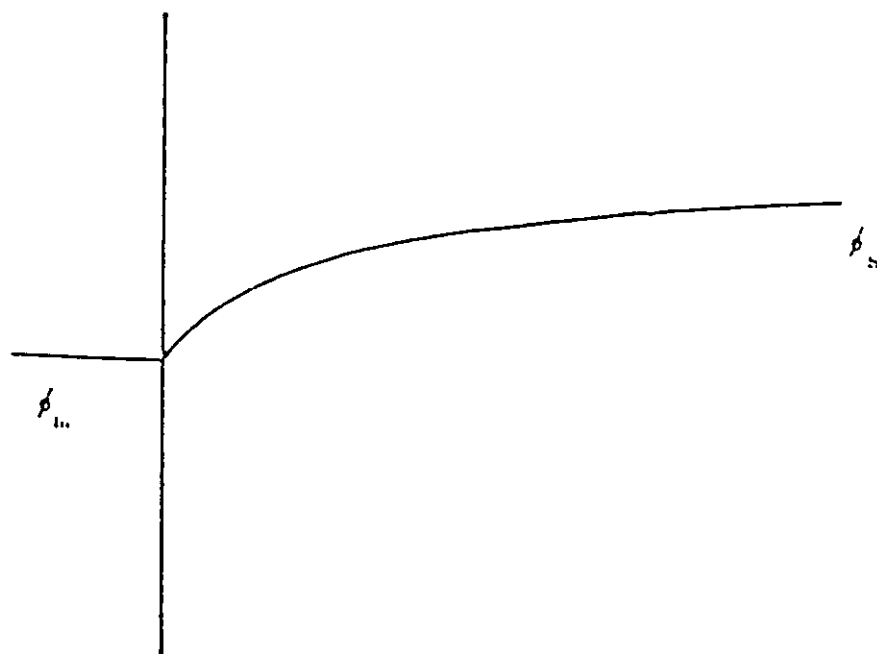INTERFACE PREDICTED BY THE HELMHOLTZ MODEL.

Fig. 2.2. Gouy – Chapman model of the double layer.

Variation of potential with distance through the interface predicted by the Gouy – Chapman model.

of the interphase. Stern [14] provided a suitable correction in the form of an adsorbed layer of ions of finite size and an approach at the electrode limited to a certain critical distance. Hence the double layer can be divided into two regions, one of high field and low dielectric constant next to the electrode due to a row of firmly held ions and beyond this a diffuse layer in which the electrostatic and thermal motions are balanced.

The double layer can thus be treated as two capacitors connected in series:

$$\frac{1}{C_L} = \frac{1}{C_{fixed}} + \frac{1}{C_{diffuse}}$$

C_L = overall double-layer differential capacitance.

C_{fixed} = differential capacitance corresponding to a fixed layer.

$C_{diffuse}$ = differential capacitance corresponding to a diffuse layer.

The potential gradient in the entire double layer has a large component due to the compact layer and a smaller contribution from the diffuse layer, which is called the zeta potential (see fig. 2.3).

Grahame [15] postulated that the compact layer or Helmholtz fixed plane was further divided into two regions. The inner Helmholtz plane consisting of specifically adsorbed ions closest to the electrode surface and the outer Helmholtz plane consisting of normal hydrated ions at their distance of closest approach, see fig. 2.4.

Devanathan et al [16] proposed that the adsorbed solvated cations remained outside a layer of strongly orientated solvent dipoles. The inner solvent layer is penetrated by specifically adsorbed anions and the water molecules are thought to be adsorbed with their negative poles pointing either towards or away from the metal surface, depending on the potential, see fig. 2.5. The Helmholtz model over emphasizes the rigidity of the ionic environment and the Gouy-Chapman model over emphasizes its mobility, but the Stern model combines the two previous models.

It is very important to know the potential profile of the double layer as this will govern the rate at which charges can be moved across from one side of the interphase to the other and so
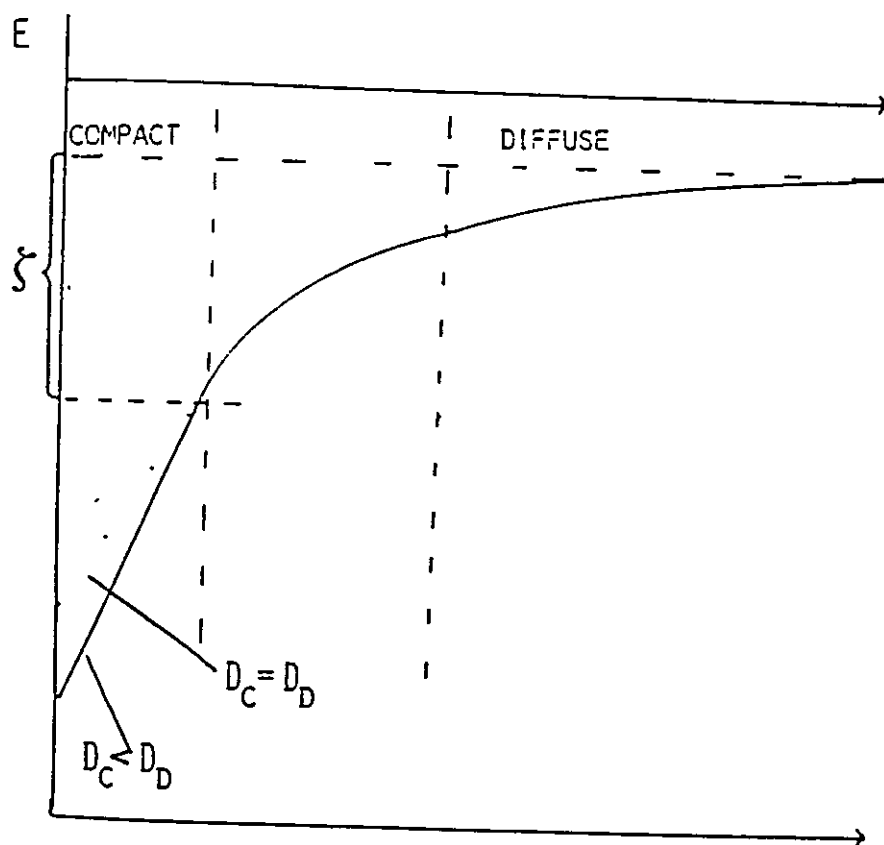
FIG. 2.3. THE STERN MODEL.
D IS THE DIELECTRIC CONSTANT OF THE COMPACT 'C' AND
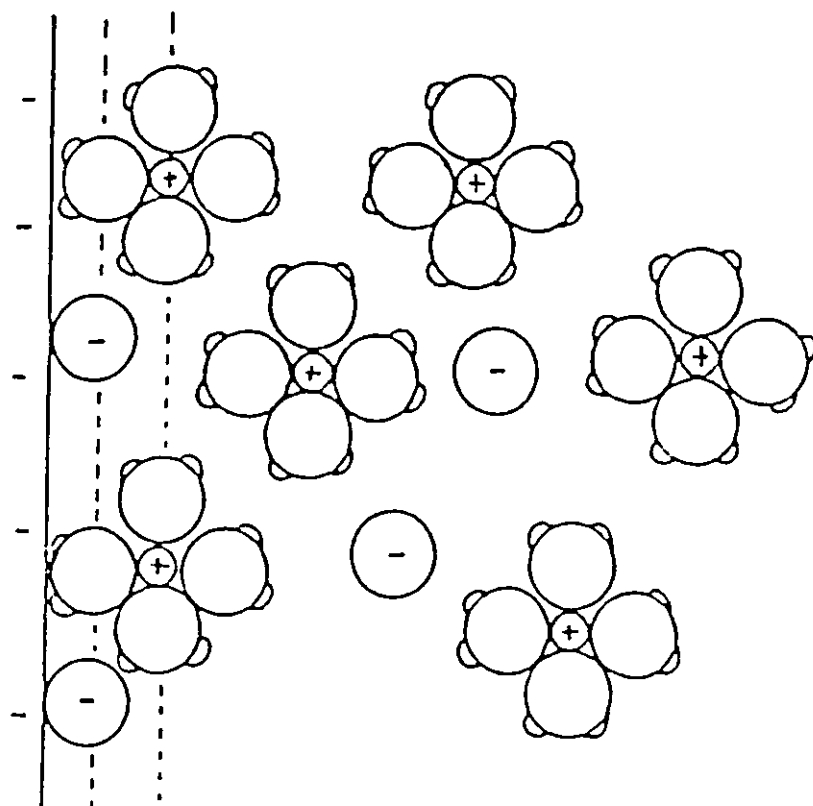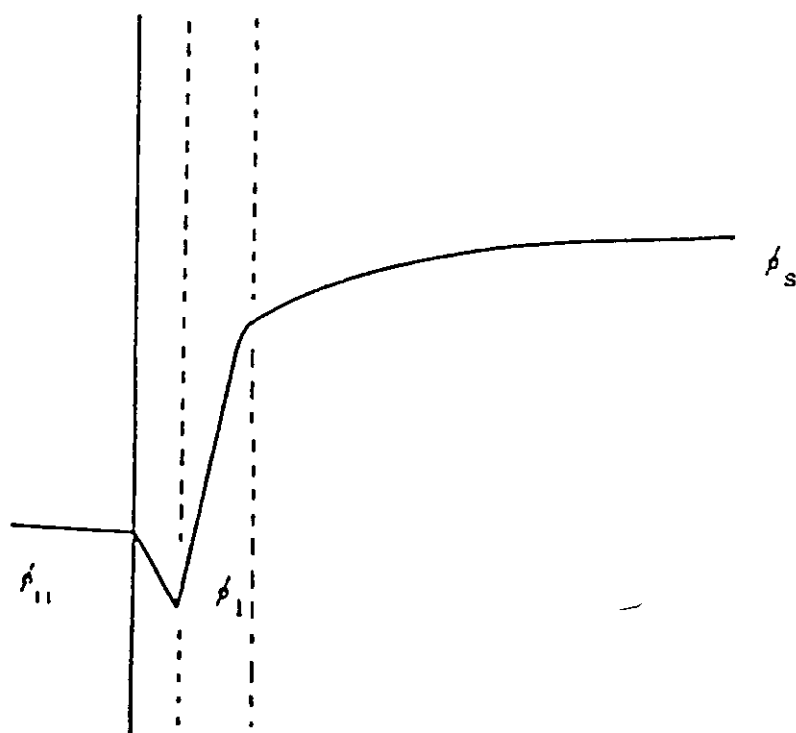DIFFUSE 'D' LAYERS.

FIG. 2.4. GRAHAME MODEL OF THE DOUBLE LAYER.

VARIATION OF POTENTIAL WITH DISTANCE THROUGH THE
INTERFACE PREDICTED BY THE GRAHAME MODEL.

FIG. 2.5. THE COMPLETE MODEL OF THE ELECTRICAL DOUBLE LAYER.
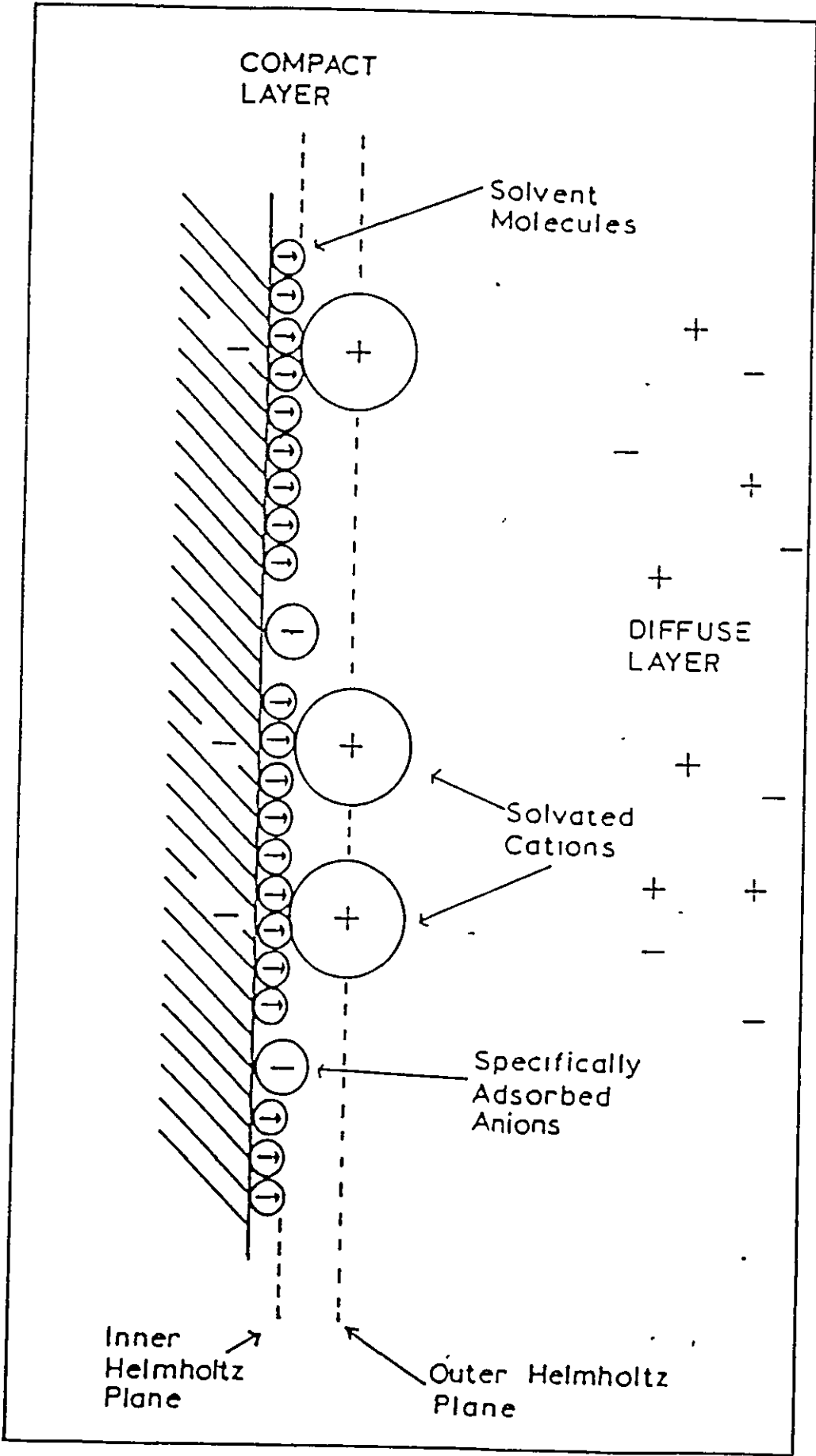
control the rate of electrochemical processes at the electrode. Such deviations, in potential and concentration at the interphase, from those of the bulk electrode and electrolyte give rise to a number of apparent anomalies. The basic concepts have been described by Frumkin [17] and the observed effect is sometimes known as the Frumkin effect.

More recent work done on the interphase structure has been mainly concerned with the orientation of the water dipoles in the fixed layer. Cooper and Harrison [18-22] give details of progress in this field up to 1978.

Although all the theory presented here is for aqueous systems it is assumed to apply for polar non-aqueous systems such as acetonitrile.

2.2 The Charge Transfer Process

The charge transfer process can be represented by the overall redox reaction

$$Ox + ne^- \underset{k_b}{\overset{k_f}{\rightleftharpoons}} Red \qquad (2.2.1)$$

where k_f and k_b are the forward and backward reaction rate constants, and n is the number of electrons transferred.

This electrode process may be split up into a number of consecutive steps:

(i)   mass transport of reactants to the electrode surface.

(ii)   adsorption of reactants on to the surface.

(iii) the surface process.

(iv)   desorption of products.

(v)   transport of products away from the electrode.

Any one of these steps or any combination may be rate determining.

In order to study this redox process we consider a noble metal electrode dipping into a solution containing, usually, both the oxidised (Ox) and reduced forms(Red)of the couple, often in the presence of an excess of an indifferent or supporting electrolyte; such a system ($Hg/KCL_{aq}(1M)$) was used by Grahame [15] in the early investigation of the structure of the double layer.

If the surface process is sufficiently fast, the system will display a readily reproducible open-circuit potential. A net anodic or cathodic process can be made to occur by displacing the electrode potential from this reversible value. The electrode is then said to be polarised, and this polarisation can occur in three ways.

(a) Concentration Polarisation

This occurs when one of the mass transport processes is the rate determining step.

(b) Activation Polarisation

This occurs when one of the surface processes is the rate determining step. This is usually, but not necessarily, an electron transfer step.

(c) Ohmic Polarisation

This is due to the incorporation of an iR drop in the measured potential of the working electrode, and must be made negligibly small, or corrected for, before a kinetic analysis of the experimental results is undertaken.

The extent of polarisation is measured by the overpotential, η

$$\text{where} \quad \eta = \phi_i - \phi_o$$

and ϕ_i is the potential of the working electrode, when the system is sustaining a current of i amperes and ϕ_o is the reversible potential.

The potential being measured on any convenient scale.

2.2.1 The Surface Process

This section deals with kinetics of processes occuring at the surface and in particular the electron transfer process.

All equations derived in this section are based on the assumption that the presence of an excess of indifferent supporting electrolyte in the solution under study allows us to ignore the effect of the diffuse double layer. Parsons [23] shows that even with supporting electrolyte concentrations as high as 1M the effect of the diffuse layer is small, but still present, although the thickness of the diffuse layer is reduced by the supporting

- 7 -

electrolyte. If ϕ_2 is the potential of the closest plane of approach to the electrode surface for the reactant species then the effective potential controlling the rate of the surface process is $\phi_i - \phi_2$ and not ϕ_i. Insufficient data, however, rules out proper correction for ϕ_2.

Some important kinetic equations will now be derived:-

the cathodic and anodic current densities i_c and i_a are given by

$$i_c = k_f \, C_o \, (0,t) \, nF \qquad\qquad (2.2.2)$$

and

$$i_a = k_b \, C_R \, (0,t) \, nF \qquad\qquad (2.2.3)$$

where current densities are per unit electrode area at the electrode surface and $C_i(z,t)$ is the concentration of species i distance z from the electrode surface after time t, so $C_o(0,t)$ is the surface concentration of the oxidised species Ox.

Initial Conditions

(i) $t = 0$; $z \geqslant 0$; $C_o(z,0) = C_o^*$

$$C_R(z,0) = C_R^*$$

C_i^* are the bulk concentration of species i.

(ii) $t \geqslant 0$; $z \to \infty$; $C_o(z,t) \to C_o^*$

$$C_R(z,t) \to C_R^*$$

$z = 0$ is the junction of the diffuse part of the double layer with the bulk of the solution.

The nett current density i is given by

$$i = i_c - i_a \qquad\qquad (2.2.4)$$

so $i = nF \, \{k_f C_o(0,t) - k_b C_R(0,t)\}$ \qquad (2.2.5)

the potential dependent rate constants k_f and k_b are given by

$$k_f = k_f^{\,o} \exp \left\{ \frac{-\alpha nFE}{RT} \right\} \tag{2.2.6}$$

$$k_b = k_b^{\,o} \exp \left\{ \frac{(1-\alpha)nFE}{RT} \right\} \tag{2.2.7}$$

where $k_f^{\,o}$ and $k_b^{\,o}$ are the values of k_f and k_b at the reference potential, E is the potential measured from the reference potential and α is the charge transfer coefficient [24].

More generally α and $(1-\alpha)$ should be α and β with $\alpha + \beta$ not necessarily equal to unity. The physical significance of the transfer coefficients is that α is a fraction which reflects the extent to which the potential displacement E favours the anodic process, and β the fraction which favours the cathodic process. In the case of a unit step, we would expect that $\beta = (1-\alpha)$, but this is not always the case.

So from equations (2.2.5), (2.2.6) and (2.2.7)

$$i = nF \left\{ k_f^{\,o} \exp \left[\frac{-\alpha nFE}{RT} \right] C_O(0,t) - k_b^{\,o} \exp \left[\frac{(1-\alpha)nFE}{RT} \right] C_R(0,t) \right\} \tag{2.2.8}$$

at the reversible electrode potential, E_o the nett current is zero.

$$\text{So} \quad i_c = i_a = i_o \tag{2.2.9}$$

i_o is the exchange current density, there is no concentration gradient at the electrode surface so

$$C_i(0,t) = C_i^*; \quad E = E_o \tag{2.2.10}$$

So from equations (2.2.8), (2.2.9) and (2.2.10)

$$i_o = nFk_f^{\,o}C_O^* \exp \left[\frac{-\alpha nFE_o}{RT} \right] \tag{2.2.11}$$

and

$$i_o = nFk_b^{\,o}C_R^* \exp \left[\frac{(1-\alpha)nFE_o}{RT} \right] \tag{2.2.12}$$

So substituting equations (2.2.11) and (2.2.12) back into (2.2.8) we obtain:-

$$i = i_o \left\{ \exp \left[\frac{-\alpha nF(E-E_o)}{RT} \right] \frac{C_R(0,t)}{C_R^*} - \frac{C_o(0,t)}{C_o^*} \exp \left[\frac{(1-\alpha)nF(E-E_o)}{RT} \right] \right.$$

(2.2.13)

when i is small as it would be for small overpotentials then the bulk concentration is little disturbed at the interphase and

$$C_i(0,t) \simeq C_i^*$$

and equation (2.2.13) reduces to equation (2.2.14). $(E-E_o)$ is defined as the charge transfer overpotential, n_t [25] and (2.2.14) is known as the Erdey-Gruz and Volmer equation [26].

$$i = i_o \left\{ \exp \left[\frac{-\alpha nFn_t}{RT} \right] - \exp \left[\frac{(1-\alpha)nFn_t}{RT} \right] \right.$$

(2.2.14)

If the overpotential is small (2.2.14) reduces to equation (2.2.15) and an approximately linear overpotential-current curve is obtained.

$$i \simeq -i_o \frac{nFn_t}{RT}$$

(2.2.15)

comparison with Ohm's law gives the charge transfer resistance, R_{ct} as

$$R_{ct} = \frac{RT}{i_o nF}$$

(2.2.16)

R_{ct} has dimensions ohms/area, a more rigorous definition for R_{ct} is

$$\frac{1}{R_{ct}} = \left[\frac{\partial i}{\partial n_t} \right]_{C_i, n_t = 0}$$

(2.2.17)

k_f^o and k_b^o are potential independent rate constants and an Arrhenius equation can be written for each.

$$k_f^o = k_f' \exp \left\{ \frac{-\Delta H_f^a}{RT} \right\}$$

(2.2.18)

$$k_b^o = k_b' \exp \left\{ \frac{-\Delta H_b^a}{RT} \right\}$$

(2.2.19)

where k_f^- and k_b^- are the pre-exponential factors and ΔH_f^a and $\Delta H_b^{\dot{a}}$ are the activation enthalpies for the forward and backward reactions at the reference potential.

The potential at which the energy barriers for the forward and backward reactions are the same is known as the characteristic potential E*.

The characteristic potential has been shown to be identical to the standard or normal electrode potential $E^{\ominus}$ [27].

This implies that

$$\Delta H_f^a = \Delta H_b^a = \Delta H^a \qquad (2.2.20)$$

and $\quad k_f^- = k_b^- = k^- \qquad (2.2.21)$

If $E^{\ominus}$ is taken as the reference potential, then equations (2.2.18) and (2.2.19) become

$$k_f^{o} = k_b^{o} = k^o = k^- \exp\left\{\frac{-\Delta H^a}{RT}\right\} \qquad (2.2.22)$$

where ΔH^a is the activation enthalpy for the redox reaction at the standard electrode potential for that reaction and k^o the rate constant.

So equations (2.2.11) and (2.2.12) become

$$i_o = nFk^o C_o* \exp\left\{\frac{-\alpha nFE_o}{RT}\right\} \qquad (2.2.23)$$

and $\quad i_o = nFk^o C_R* \exp\left\{\frac{(1-\alpha)nFE_o}{RT}\right\} \qquad (2.2.24)$

so eliminating $\exp\left\{\frac{nFE_o}{RT}\right\}$ between these equations we get

$$i_o = nFk^o C_R*^\alpha C_o*^{1-\alpha} \qquad (2.2.25)$$

or more fully giving the temperature dependence

$$i_o = nFk^- \exp\left\{\frac{-\Delta H^a}{RT}\right\} C_R*^\alpha C_o*^{1-\alpha} \qquad (2.2.26)$$

- 11 -

The exchange current is therefore proportional to k^o, and can often be substituted for k^o in kinetic equations. k^o can be simply interpreted as a measure of the kinetic capacity of a redox couple. A system with large k^o will achieve equilibrium quickly, whereas one with smaller k^o will take longer.

2.2.2 The Mass Transfer Process

The mechanism of mass transfer can proceed via one of three processes.

(i) Migration

Charged particles in an electric field experience a force, but this is assumed to be negligible in the presence of an excess of indifferent electrolyte.

(ii) Convection

This arises from thermal or mechanical disturbances or can be forced by stirring the solution, rotating the electrode, bubbling gas etc. or it may occur naturally due to differences in density caused by local concentration or temperature differences.

In general convection makes the calculation of concentration very difficult, one exception being the rotating disc electrode which gives rise to a constant concentration gradient at the electrode. In other cases, however, convection must be ignored and this is only really valid when Schmidt's number, ν/D (ν is the kinematic viscosity) is sufficiently high (>>1000).

The assumption is usually made, originally by Nernst [28] that the concentration gradient is located in a layer, known as the Nernst layer, of thickness δ_n, within which the liquid is nearly motionless. Convection is then implicitly taken into account, see fig. 2.6.

This Nernst model that requires transport to be entirely diffusive within the Nernst diffusion layer and entirely convective outside it is physically implausible, of course; it also allows neither the prediction of the thickness of the layer nor its dependence on forced convection, e.g. the rate of stirring.

Experimental values for the thickness of the diffusion layer are typically of the order 5×10^{-4} m for a system subject to natural convection only at room temperature decreasing to values of the order 10^{-5} m for systems subject to forced convection.
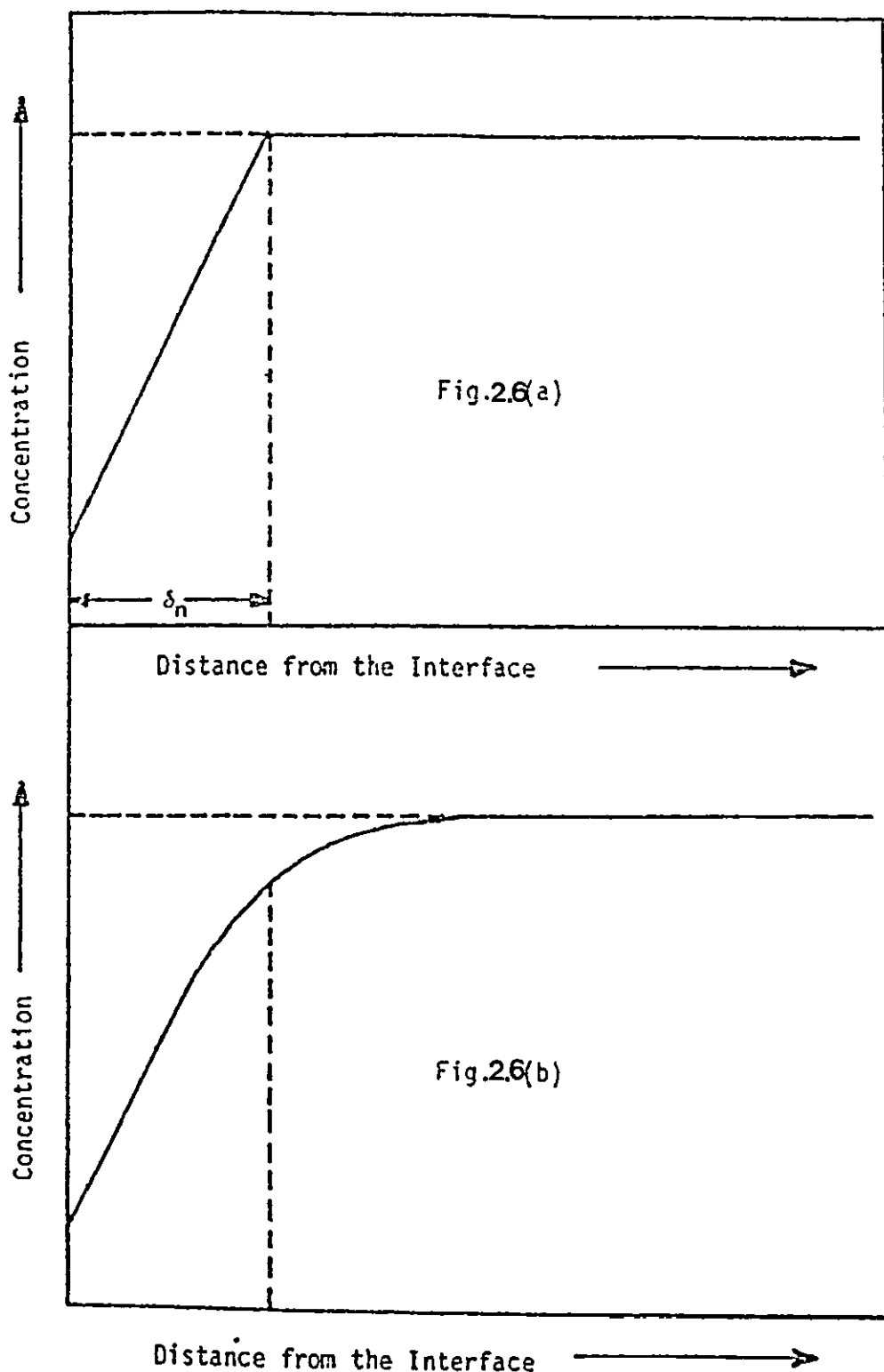
Fig.2.6(a)

δ_n

Distance from the Interface ⟶

Fig.2.6(b)

Distance from the Interface ⟶

Fig. 2.6b The true concentration profile at an
electrode surface.
Fig. 2.6a The Nernst approximation to fig. 2.6b.

(iii) <u>Diffusion</u>

Diffusion occurs whenever concentration differences are set up, and is governed by Fick's two laws.

Fick's first law states that the rate at which   species, i, $\dfrac{dN_i}{dt}$, diffuse through a given area A is proportional to the concentration gradient of the diffusing species

$$\frac{1}{A} \frac{dN_i}{dt} = D_i \frac{\partial C_i}{\partial z}(z,t) = J_i \qquad (2.2.27)$$

this is for one dimensional diffusion D_i is the diffusion coefficient of species i and J_i is the flux.

Time dependent concentrations are governed by Fick's second law,

$$\frac{\partial C_i}{\partial t}(z,t) = D_i \frac{\partial^2 C_i(z,t)}{\partial z^2} \qquad (2.2.28)$$

The Diffusion Overvoltage

The diffusion overvoltage, η_D, is seen when the supply of reactants at the electrode or the removal of the reaction products is the rate determining when current flows.

For an ideally reversible system the rate constant k_f and k_b, as well as the exchange current, i_o, can be considered as infinitely high. Therefore if charge transfer is assumed to be sufficiently fast with respect to diffusion for the condition of quasi-equilibrium to be maintained at the electrode surface, then the boundary conditions at the electrode are given by the Nernst equation.

So the diffusion overvoltage is equal to the difference between the equilibrium potential in the absence of current flow, E_o and the equilibrium potential which forms during current flow as a result of the changed concentrations $C_i(0,t)$ at the electrode surface as opposed to $C_i{}^*$, E_o'

$$\eta_D = E_o' - E_o \qquad (2.2.29)$$

applying the Nernst equation to the electrode surface at equilibrium

$$E_o = E^\theta + \frac{RT}{nF} \ln \frac{C_o{}^*}{C_R{}^*} \qquad (2.2.30)$$

- 13 -

and current is flowing

$$E_0 \doteq E^\ominus + \frac{RT}{nF} \ln \frac{C_O(0,t)}{C_R(0,t)} \qquad (2.2.31)$$

$$\text{So} \quad \eta_D = \frac{RT}{nF} \ln \left[\frac{C_O(0,t)}{C_O{}^*} \quad \frac{C_R{}^*}{C_R(0,t)} \right] \qquad (2.2.32)$$

Strictly speaking the Nernst equation can only be applied to a system at equilibrium, but it is assumed to give a good approximation here.

2.2.3 <u>A.C. Theory</u>

In this section we shall examine the response of the system described above to a small alternating perturbation in the overvoltage, η. Fig. 2.7 shows part of the i-E curve and it demonstrates that for small enough perturbations in E, the curve is approximately linear.

From equation (2.2.14)

$$i = i_0 \left\{ \exp \left[\frac{-\alpha nF\eta_t}{RT} \right] - \exp \left[\frac{(1-\alpha)nF\eta_t}{RT} \right] \right\} \qquad (2.2.14)$$

we see that by small we mean

$$|\eta_t| << \frac{RT}{\alpha nF} \qquad (2.2.33)$$

$$\text{and} \quad |\eta_t| < \frac{RT}{(1-\alpha)nF} \qquad (2.2.34)$$

which gives

$$i = \frac{-i_0 nF\eta_t}{RT} \qquad (2.2.15)$$

If the perturbation in the overvoltage ΔE is written as

$$e = \Delta E \exp (j\omega t) \qquad (2.2.35)$$
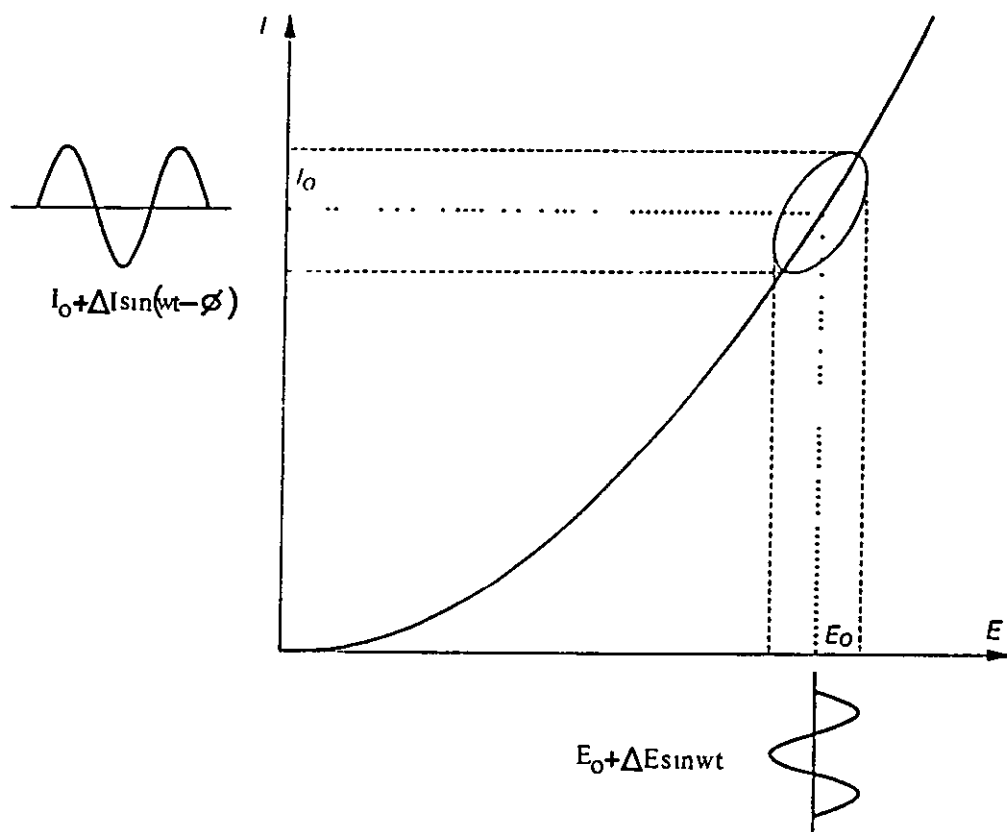
then if the current is

Figure 2.7   A portion of the i-E curve showing its response to small perturbations in E.

$$i = \Delta I \exp\left(j(\omega t - \phi)\right) \qquad (2.2.36)$$

where ΔI, ΔE are the amplitudes and ϕ is the phase lag, ω is the frequency, $j = \sqrt{-1}$ then impedance will be given by

$$Z(\omega) = \left|\frac{\Delta E}{\Delta I}\right| e^{j\phi} \qquad (2.2.37)$$

if the current is not of the above form then the impedance can not be defined in this way.

For the charge transfer resistance we have as before

$$R_{ct} = Z(\omega) = \frac{RT}{i_o nF} \qquad (2.2.38)$$

which is a pure resistance, i.e. $\phi = 0$, and it is not dependent on frequency.

If we now include the double layer capacitance, C_{dl}, the system under this perturbation can be represented by equivalent electric components and the circuit is known as the Randles equivalent circuit [29], see fig. 2.8. R_e is the solution resistance.

This, however, ignores diffusion which will give rise to an impedance. The derivation given below for the impedance due to diffusion belongs originally to Warburg [30] and Kruger [31] and this impedance is commonly known as the Warburg impedance.

2.2.3.1 Theory of the Warburg Impedance

After a perturbation in the current density a steady state concentration is only reached asymptotically with time. Therefore a time dependent current will lead to a concentration distribution which is also time dependent and fluctuates at the same frequency.

It is clear that Fick's Second Law equation (2.2.28) will be of fundamental importance in this derivation

$$\frac{\partial C_j(z,t)}{\partial t} = \frac{D_j \partial^2 C_j(z,t)}{\partial z^2} \qquad (2.2.28)$$

and its solution vital.

If we separate the functions $C_j(z,t)$ into the product of functions of z and t only, and let $C_j(z,t) = C_j{}^* + \Delta C_j(z,t)$
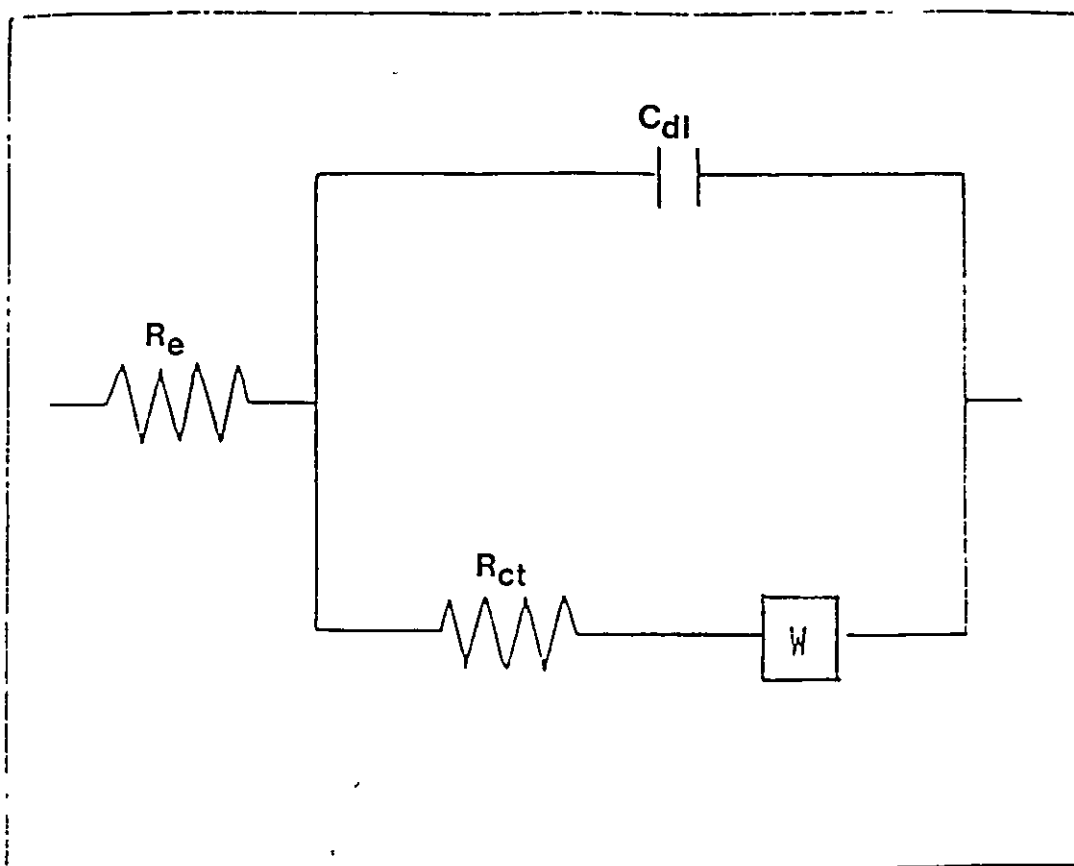
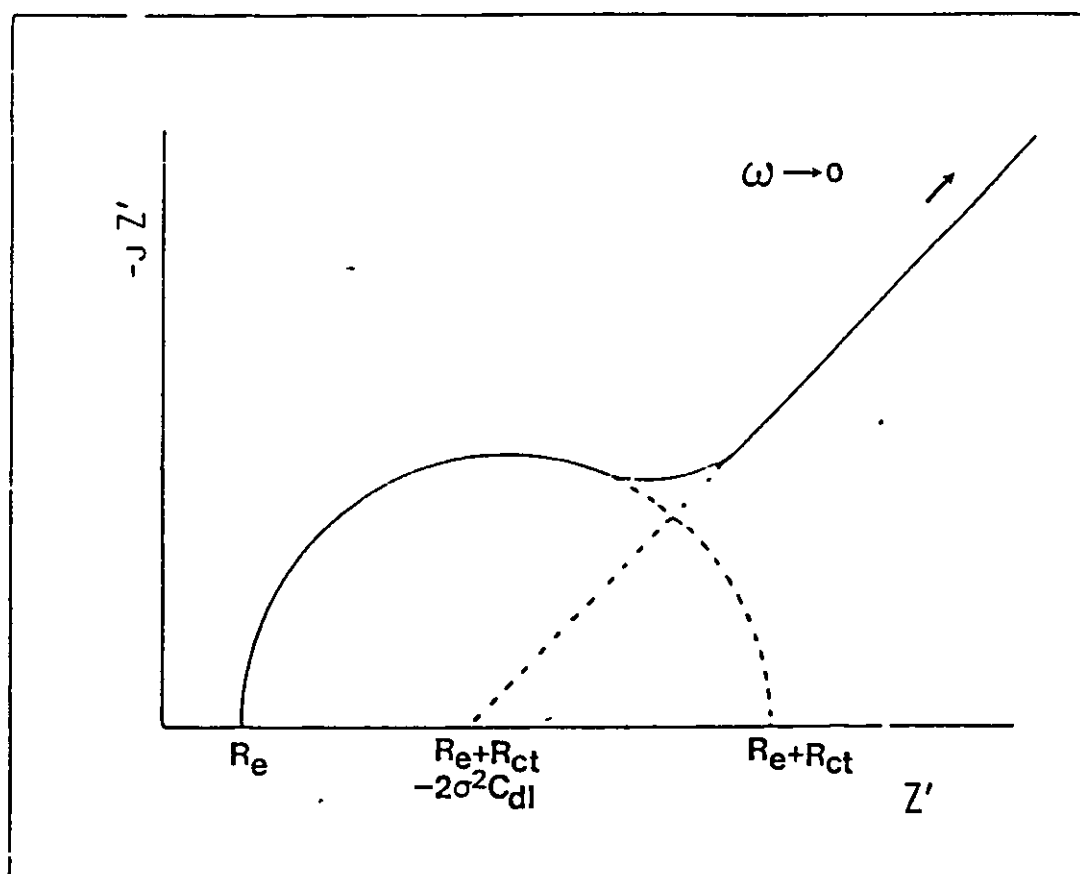Figure 2.8   Randles type equivalent circuit including Warburg component.

Figure 2.9   The complex plane (Sluyter's Plot) for the circuit in Figure 2.8.

$$\Delta C_j(z,t) = \Delta C_{zj}(z)\Delta C_{tj}(t) \qquad (2.2.39)$$

we may be able to find a solution of this form. If we get a physically acceptable solution which fits all the boundary conditions then we do not have to worry about the mathematical uniqueness of the solution, there can only be one physical solution and if we have found one then that must be it. Of course, we may not find a solution of this form, in which case we will have to try a different form.

So substituting for $\Delta C_j(z,t)$, equation (2.2.39) in Fick's Second Law (2.2.28) we get

$$\frac{\partial}{\partial t}\{\Delta C_{zj}(z)\Delta C_{tj}(t)\} = D_j \frac{\partial^2}{\partial z^2}\{\Delta C_{zj}(z)\Delta C_{tj}(t)\} \qquad (2.2.40)$$

which rearranging becomes

$$\frac{1}{\Delta C_{tj}(t)} \frac{\partial}{\partial t}(\Delta C_{tj}(t)) = \frac{D_j}{\Delta C_{zj}(z)} \frac{\partial^2}{\partial z^2}[\Delta C_{zj}(z)] \qquad (2.2.41)$$

As the L.H.S. is a function of t only and the R.H.S. a function of z only, each side must be equal to the same constant, say M.

So we get two differential equations

$$\frac{1}{\Delta C_{tj}(t)} \frac{\partial}{\partial t} \Delta C_{tj}(t) = M \qquad (2.2.42)$$

$$\frac{D_j}{\Delta C_{zj}(z)} \frac{\partial^2 \Delta C_{zj}(z)}{\partial z^2} = M \qquad (2.2.43)$$

both of which can be easily solved to give

$$\Delta C_{tj}(t) = A \exp(Mt) \qquad (2.2.44)$$

and

$$\Delta C_{zj}(z) = B \exp\left(\sqrt{\frac{M}{D_j}}\, z\right) + C \exp\left(-\sqrt{\frac{M}{D_j}}\, z\right) \qquad (2.2.45)$$

where A, B, C are constants.

To get a boundary condition we consider the current i

$$i = \Delta I e^{j\omega t} \tag{2.2.46}$$

from Faraday's Law

$$i = -nFJ_j \tag{2.2.47}$$

and Fick's First Law

$$J_j = D_j \frac{\partial \Delta C_j(z,t)}{\partial z} \tag{2.2.27}$$

the current at the surface of the electrode is given by combining equations (2.2.47) and (2.2.27)

$$i = -nFD_j \left[\frac{\partial \Delta C_j(z,t)}{\partial z} \right]_{z=0} \tag{2.2.48}$$

so combining (2.2.46) and (2.2.48)

$$\Delta I e^{j\omega t} = -nFD_j \left[\frac{\partial \Delta}{\partial z} C_j(z,t) \right]_{z=0} \tag{2.2.49}$$

to find $\left[\frac{\partial}{\partial z} \Delta C_j(z,t) \right]_{z=0}$

$$\Delta C_j(z,t) = A \exp(Mt) \left\{ B \exp\left(\sqrt{\frac{M}{D_j}}\, z \right) + C \exp\left(-\sqrt{\frac{M}{D_j}}\, z \right) \right\} \tag{2.2.50}$$

$$\frac{\partial \Delta C_j}{\partial z}(z,t) = A \exp(Mt) \left\{ \sqrt{\frac{M}{D_j}}\, B \exp\left(\sqrt{\frac{M}{D_j}}\, z \right) - \sqrt{\frac{M}{D_j}}\, C \exp\left(-\sqrt{\frac{M}{D_j}}\, z \right) \right\} \tag{2.2.51}$$

$$\left[\frac{\partial \Delta}{\partial z} C_j(z,t) \right]_{z=0} = A \exp(Mt) \{B-C\} \sqrt{\frac{M}{D_j}} \tag{2.2.52}$$

so substituting this into equation (2.2.49)

$$\Delta I \exp(j\omega t) = -nFD_j A \exp(Mt) \{B-C\} \sqrt{\frac{M}{D_j}} \tag{2.2.53}$$

so M must equal $j\omega$,

and $A(B-C) = -\dfrac{\Delta I}{nF} \sqrt{\dfrac{1}{j\omega D_j}}$ (2.2.54)

For a diffusion layer of infinite thickness which is unsatisfactory at low frequencies as will be discussed later. In this case we get the further boundary condition.

$\Delta C_j \to 0$ as $z \to \infty$

and this implies $B = 0$.

So equation (2.2.54) beocmes

$A.C = \dfrac{\Delta I}{nF} \sqrt{\dfrac{1}{j\omega D_j}}$ (2.2.55)

and susbtituting this into equation (2.2.50) we get

$\Delta C_j(z,t) = \dfrac{\Delta I}{nF} \sqrt{\dfrac{-j}{\omega D_j}} \{\exp(j\omega t)\}\{\exp(-\sqrt{\dfrac{j\omega}{D_j}} z\}$ (2.2.56)

this variation in concentration at the electrode surface gives a variation in the diffusion overvoltage, η_D according to equation (2.2.32)

$\eta_D = \dfrac{RT}{nF} \ln\left[\dfrac{C_0(0,t)}{C_0{}^*} \dfrac{C_R{}^*}{C_R(0,t)}\right]$ (2.2.32)

and $\quad C_0(0,t) = C_0{}^* + \Delta C_0(0,t)$ (2.2.57)

$C_R(0,t) = C_R{}^* + \Delta C_R(0,t)$ (2.2.58)

and putting $z = 0$ in equation (2.2.56) to get

$\Delta C_j(0,t) = \dfrac{\Delta I}{nF} \sqrt{\dfrac{-j}{\omega D_j}} (\exp(j\omega t))$ (2.2.59)

and from this we can get $\Delta C_0(0,t)$ and $\Delta C_R(0,t)$ and susbstitute these values into equations (2.2.57) and (2.2.58)

So
$$C_O(0,t) = C_O{}^* + \frac{\Delta I}{nF} \sqrt{\frac{-j}{\omega D_O}} \exp(j\omega t) \qquad (2.2.60)$$

$$C_R(0,t) = C_R{}^* + \frac{\Delta I}{nF} \sqrt{\frac{-j}{\omega D_R}} \exp(j\omega t) \qquad (2.2.61)$$

and equation (2.2.32) becomes

$$\eta_D = \frac{RT}{nF} \left\{ \ln\left[1 + \frac{\Delta C_O(0,t)}{C_O{}^*}\right] - \ln\left[1 + \frac{\Delta C_R(0,t)}{C_R{}^*}\right] \right\} \qquad (2.2.62)$$

as $\frac{\Delta C_i}{C_i{}^*}$ will be small we can make the approximation

$$\ln(1+x) \simeq x - \tfrac{1}{2}x^2 + \tfrac{1}{3}x^3 +$$
$$\ln(1+x) \simeq x \qquad (2.2.63)$$

and this gives

$$\eta_D = \frac{RT}{nF} \left\{ \frac{\Delta C_O(0,t)}{C_O{}^*} - \frac{\Delta C_R(0,t)}{C_R{}^*} \right\} \qquad (2.2.64)$$

so substituting for $\Delta C_O(0,t)$ and $\Delta C_R(0,t)$ from equations (2.2.60)
and (2.2.61) we get

$$\eta_D = \frac{RT}{nF} \left\{ \frac{1}{C_O{}^*\sqrt{D_O}} - \frac{1}{C_R{}^*\sqrt{D_R}} \right\} \frac{\Delta I}{nF} \sqrt{\frac{-j}{\omega}} \exp(j\omega t) \qquad (2.2.65)$$

$$\sqrt{-j} = e^{-j\pi/4} \qquad (2.2.65)$$

so this becomes

$$\eta_D = \frac{RT}{n^2 F^2} \left\{ \frac{1}{C_O{}^*\sqrt{\omega D_O}} - \frac{1}{C_R{}^*\sqrt{\omega D_R}} \right\} \Delta I \exp\{j(\omega t - \pi/4)\} \qquad (2.2.66)$$

rewriting equations (2.2.35), (2.2.36) and (2.2.37) we get

$$i = \Delta I \exp(j\omega t) \qquad (2.2.67)$$

$$e = \Delta E \exp(j(\omega t + \phi)) \qquad (2.2.68)$$

and
$$Z(\omega) = \left|\frac{\Delta E}{\Delta I}\right| e^{j\phi} \qquad (2.2.37)$$

in this case we have

$$e = n_D \tag{2.2.69}$$

and
$$\Delta E = \frac{RT}{n^2 F^2} \left\{ \frac{1}{C_o * \sqrt{\omega D_o}} - \frac{1}{C_R * \sqrt{\omega D_R}} \right\} \Delta I \tag{2.2.70}$$

and
$$\phi = -\frac{\pi}{4} \tag{2.2.71}$$

So
$$Z(\omega) = \frac{RT}{n^2 F^2} \left\{ \frac{1}{C_o * \sqrt{\omega D_o}} - \frac{1}{C_R * \sqrt{\omega D_R}} \right\} \exp\left(\frac{-j\pi}{4} \right) \tag{2.2.72}$$

and this is the Warburg Impedance. It has a phase lag of 45° and so its equivalent circuit element is a resistor and capacitor of equal magnitude impedance in series. The magnitude of the resistor and capacitor also vary with frequency as $\omega^{-\frac{1}{2}}$.

The Randles equivalent circuit can now be modified to include the Warburg Impedance, see fig. 2.8. The Warburg Impedance can be written as

$$W = \sigma \omega^{-\frac{1}{2}} - j \sigma \omega^{-\frac{1}{2}} \tag{2.2.73}$$

where
$$\sigma = \frac{\sqrt{2}}{2} \frac{RT}{n^2 F^2} \left\{ \frac{1}{C_o * \sqrt{D_o}} - \frac{1}{C_R * \sqrt{D_R}} \right\} \tag{2.2.74}$$

and the total impedance can be written as

$$Z = R_e + \left\{ j\omega C_{dl} + \left[R_{Ct} + \sigma\omega^{-\frac{1}{2}} - j\sigma\omega^{-\frac{1}{2}} \right]^{-1} \right\}^{-1} \tag{2.2.75}$$

$$= R_e + \frac{(R_{Ct} + \sigma\omega^{-\frac{1}{2}} - j\sigma\omega^{-\frac{1}{2}})}{(j\omega C_{dl})(R_{Ct} + \sigma\omega^{-\frac{1}{2}} - j\sigma\omega^{-\frac{1}{2}}) + 1} \tag{2.2.76}$$

separating real and imaginary parts

$$= R_e + \frac{(R_{Ct} + \sigma\omega^{-\frac{1}{2}}) - j(\sigma\omega^{-\frac{1}{2}})}{(1 + \omega^{\frac{1}{2}}\sigma C_{dl}) + j(\omega C_{dl} R_{Ct} + \omega^{\frac{1}{2}} C_{dl}\sigma)} \tag{2.2.77}$$

multiplying top and bottom by the complex conjugate.

- 20 -

$$= R_e + \{[(R_{Ct}+\sigma\omega^{-\frac{1}{2}})(1+\omega^{\frac{1}{2}}\sigma C_{dl})-(\sigma\omega^{-\frac{1}{2}})(\omega C_{dl}R_{Ct}+\omega^{\frac{1}{2}}C_{dl}\sigma)]$$
$$- j[(\sigma\omega^{-\frac{1}{2}})(1+\omega^{\frac{1}{2}}\sigma C_{dl})+(R_{Ct}+\sigma\omega^{-\frac{1}{2}})(\omega C_{dl}R_{Ct}+\omega^{\frac{1}{2}}C_{dl}\sigma)]\}$$
$$/\{(1+\omega^{\frac{1}{2}}\sigma C_{dl})^2+(\omega C_{dl}R_{Ct}+\omega^{\frac{1}{2}}C_{dl}\sigma)^2\} \tag{2.2.78}$$

$$= R_e + \{(R_{Ct}+\sigma\omega^{-\frac{1}{2}})-j(\sigma\omega^{-\frac{1}{2}}+2\sigma^2C_{dl}+R_{Ct}{}^2\omega C_{dl}+2R_{Ct}\omega^{\frac{1}{2}}\sigma C_{dl})\}$$
$$/\{(1+\sigma\omega^{\frac{1}{2}}C_{dl})^2+\omega^2(R_{Ct}C_{dl}+\sigma\omega^{-\frac{1}{2}}C_{dl})^2\} \tag{2.2.79}$$

Two limiting cases are now considered.

(a) When charge transfer is important.

This is at high frequencies ($W\to0$) or when diffusion is unimportant ($D_i\to\infty$; $\sigma\to0$; $W\to0$) and the electroactive species are always at their Nernstian concentration at the electrode surface. Equation 2.2.79 reduces to

$$Z = R_e + \frac{R_{Ct} - j\omega R^2{}_{Ct}C_{dl}}{1 + \omega^2R_{Ct}{}^2C_{dl}{}^2} \tag{2.2.80}$$

as $\sigma\to0$

which if plotted in the complex plane as a function of frequency gives a semicircle, see fig. 2.9, the radius of semicircle has numerical value R_{Ct} or $^1/\omega^*C_{dl}$ where ω^* is the frequency in Hz at the maximum of the semicircle.

This type of complex plane plot is normally known as a Sluyter's plot [32,33].

(b) When charge transfer is unimportant compared with diffusion, i.e. when $\omega\to0$, equation 2.2.79 reduces to

$$Z = R_e + R_{Ct} + \sigma\omega^{-\frac{1}{2}}-j(\sigma\omega^{-\frac{1}{2}}+2\sigma^2C_{dl}) \tag{2.2.81}$$

which again plotting in the complex plane as a function of frequency gives a straight line at an angle of 45° to the real axis, see fig. 2.9. · Fig. 2.9 shows the combined effects of charge transfer and diffusion. The actual spectrum obtained will depend on the relative values of R_{Ct} and σ.

2.2.3.2 Impedance for a diffusion layer of finite thickness

As was mentioned earlier the above approach may not give the correct low frequency behaviour as convection was ignored and the diffusion layer was assumed to have infinite thickness.

A treatment which takes account of convection by making use of the Nernst approximation, see 2.2.2 (ii), fig. 2.6, was given originally by Llopis [34] and gives the following new expression for the Diffusion of Warburg Impedance $Z(\omega)$

$$Z(\omega) = \frac{RT}{\sqrt{2}n^2F^2}(1-j)\omega^{-\frac{1}{2}}\left\{\frac{1}{C_O{}^*\sqrt{D_O}}\tanh\left[\delta_N\sqrt{\frac{(j\omega)}{D_O}}\right] - \right.$$

$$\left.\frac{1}{C_R{}^*\sqrt{D_R}}\tanh\left[\delta_N\sqrt{\frac{(j\omega)}{D_R}}\right]\right\} \qquad (2.2.82)$$

$$\tanh x \to 1 \text{ as } x \to \infty$$

so it can be seen that as $\delta_N \to \infty$, $Z(\omega)$ reduces to the old Warburg impedance, which is convenient. It also reduces to the old Warburg impedance as $\omega \to \infty$ and therefore has the same high frequency dependence.

To find the low frequency limit or D.C. point

$$\tanh x \to x \text{ as } x \to 0$$

So $Z(\omega)$ reduces to, $\omega \to 0$

$$\frac{RT}{\sqrt{2}\ n^2F^2}(1-j)\omega^{-\frac{1}{2}}\left\{\frac{1}{C_O{}^*\sqrt{D_O}}\delta_N\sqrt{\frac{j\omega}{D_O}} - \frac{1}{C_R{}^*\sqrt{D_R}}\delta_N\sqrt{\frac{j\omega}{D_R}}\right\} \qquad (2.2.83)$$

So

$$\underset{\omega\to 0}{Z(\omega)} = \frac{RT}{n^2F^2}\left[\frac{1}{C_O{}^*D_O} - \frac{1}{C_R{}^*D_R}\right]\delta_N \qquad (2.2.84)$$

which is a purely real resistance and as one would expect the impedance returns to the real axis as the frequency tends to zero, which is in contrast to the old Warburg impedance which tended to infinity at 45° to real axis as $\omega \to 0$.

The point at which the impedance returns to the real axis is the pure resistance R_{dc},

$$R_{dc} = \frac{RT}{n^2F^2} \left[\frac{1}{C_o^* D_o} - \frac{1}{C_R^* D_R} \right] \delta_N + R_e + R_{Ct} \quad (2.2.85)$$

2.2.3.3 The Effect of the Electrode Surface Characteristics on the Impedance Spectrum

The basic assumption in all the previous derivations has been that the electrode surface is perfectly flat and homogeneous physically and chemically.

This state of the electrode surface will never be achieved in practice, except perhaps for the mercury electrode, for the following reasons.

(a) The surface of the electrode may be composed of different crystals faces and have dislocations and impurities, which may all give rise to different electrochemical behaviour.

(b) The surface of the electrode may be partly covered with for example oxides or adsorbed molecules and ions.

(c) The surface of the electrode will almost certainly have some degree of roughness and may be pitted by discharge or may even be porous.

Also the electrode may participate in the electrode reaction so its physical and chemical structure may change with time.

De Levie has given a comprehensive review of porous and rough electrodes [35].

From a general point of view it can be shown that if the local interfacial impedance of the wall of the pore is Z then the global impedance of the pore is $\sqrt{Z}$. This would have the effect that instead of the impedance spectrum being a semi-circle and a Warburg line at 45°, it would be a quartercircle and a line at 22½°. The spectrum may, however, have an intermediate form between these two extremes, which would indicate an electrode surface somewhere between being perfectly flat and being completely porous.

A film on the electrode surface may also modify the impedance spectrum, by acting as a capacitor in series with the rest of the circuit elements, this causes the low frequency

part of the spectrum to leave the real axis at a greater angle. The combination of all these effects may make the spectrum difficult to interpret.

CHAPTER III

THE USE OF THE A.C. IMPEDANCE TECHNIQUE TO OBTAIN THERMODYNAMIC DATA
FOR THE CELL REACTION

3.1 Experimental Procedure

3.1.1 A.C. Impedance Apparatus

The impedance measurements were made using a Solartron 1250
Frequency Response Analyser (F.R.A.) in conjunction with the 1186
Electrochemical Interface. The F.R.A. was controlled by a Kemitron
3000 computer, which was also used for the acquisition of data,
which was then stored on disk for subsequent plotting and analysis.
The experimental set up is shown schematically in fig. 3.1.

As no reference electrode was available in the cells under test
REI was connected to SE.

3.1.2 Details of Cells Used

The cells used in this investigation were the Vidor Eternacell
(Crompton Parkinson Ltd., South Shields), size G4 equivalent size
½AA, capacity 0.4 Ah, rated load 18 mA, weight 8g, diameter 14.2 mm,
height 27.9 mm, volume 4.4 cm^3 and size G52 equivalent size C,
capacity 3.2 Ah, at a current of 135 mA, weight 44 g, diameter 25.6 mm,
height 49.5 mm, volume 25.6 cm^3. The cell consists of a lithium
anode, separator and an inert cathode current collector spirally
wound with the anode connected to the outer can and the cathode
current collector to the metal pin in the glass to metal seal. The
current collector consists of carbon material acetylene-black -
specific surface area 76 m^2/g - on an aluminium mesh with a P.T.F.E.
binder, at which the cathodic reaction

$$2SO_2 + 2e^- \rightleftharpoons S_2O_4{}^{2-} \qquad (3.1)$$
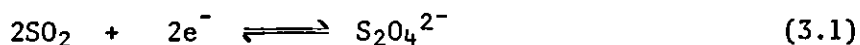
takes place. The electrolyte consists of LiBr and SO$_2$ dissolved in
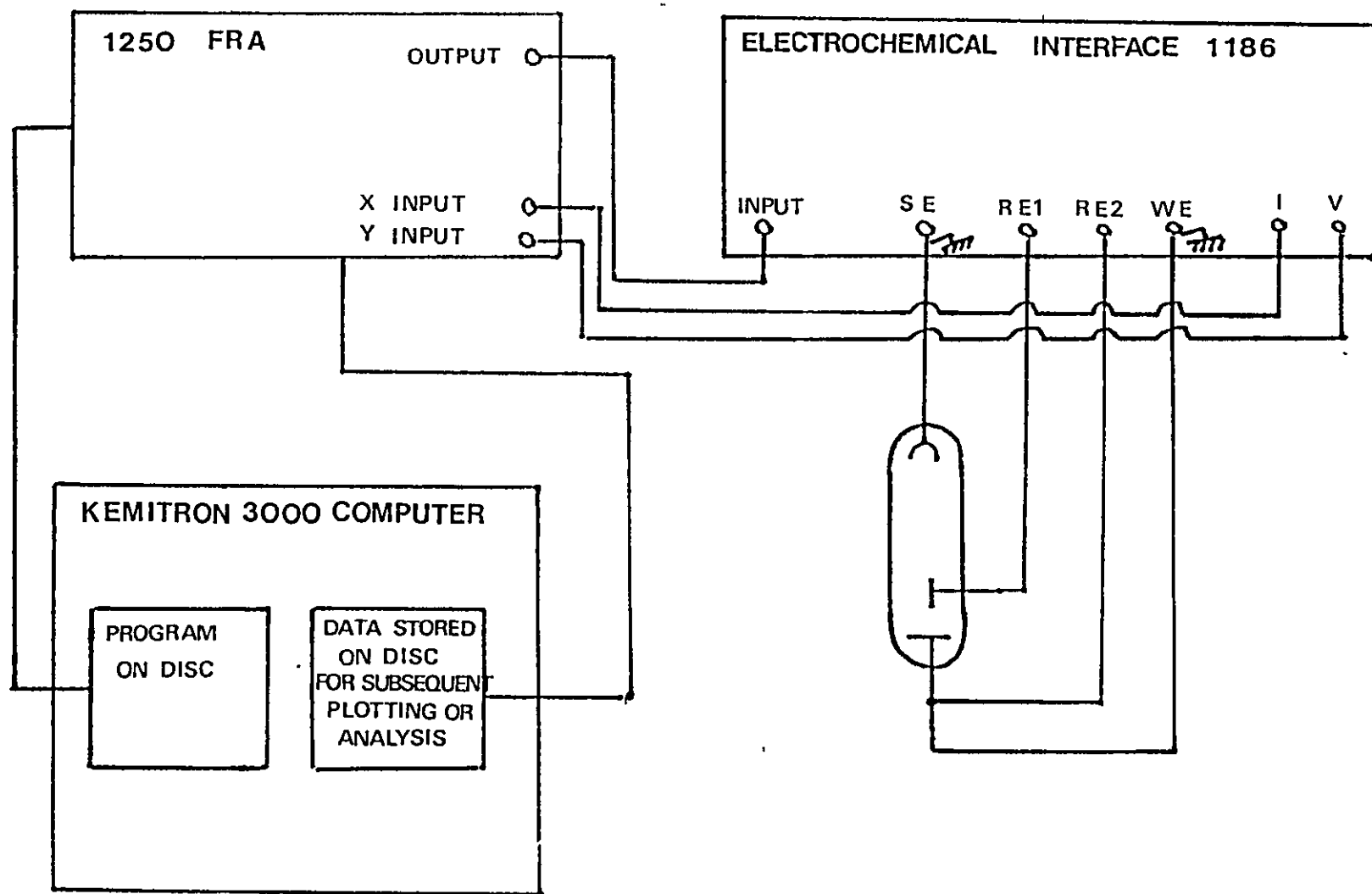acetonitrile which results in an internal cell pressure of approximately

Figure 3.1   Schematic representation of experimental set up.

60 PSI at room temperature. The SO_2 forms a protective film of lithium dithionite $Li_2S_2O_4$ on the lithium which inhibits any reaction with the acetonitrile and parasitic corrosion of the anode on open circuit and accounts for the extremely long shelf-life of these cells. A further consequence of this dithionite film is a voltage delay on discharge after a period of storage.

All the cells used in this investigation were in the new, undischarged state.

3.1.3 Procedure

Each cell was placed in a constant temperature environment (a glass container immersed in a water bath) and left for several hours to equilibrate before any measurement was made.

The impedance spectrum of the cell was then recorded and when this had been completed the open circuit voltage was measured. The temperature was then changed by a few degrees and allowed to equilibrate again before the whole procedure was repeated. None of the integration facilities of the F.R.A. was used so each measurement was taken over just one cycle and the frequency sweep was continued until the first semicircular part had been completed after, typically, only a few minutes. This procedure gave sufficient accuracy as only the diameter of the semicircle was required for the eventual analysis of results. The fequency was swept from 60 kHz to 60 mHz with ten steps per decade.

3.2 Results

Fig. 3.2 shows how the impedance spectra of a typical cell changes with temperature and Fig. 3.3 shows how the open circuit potential varies over the same temperature range.

The charge transfer resistance, θ, is obtained from the diameter of the semi-circular shapes in the impedance spectra. These shapes were slightly flattened semi-circles which is probably due to the fact that the lithium electrode has some roughness and is not ideally smooth [35]. Regarding the curves as circular sections, the diameter and hence θ can be readily obtained graphically using simple geometric techniques. This does not give an absolute value for θ, but it is sufficient for our purposes here.
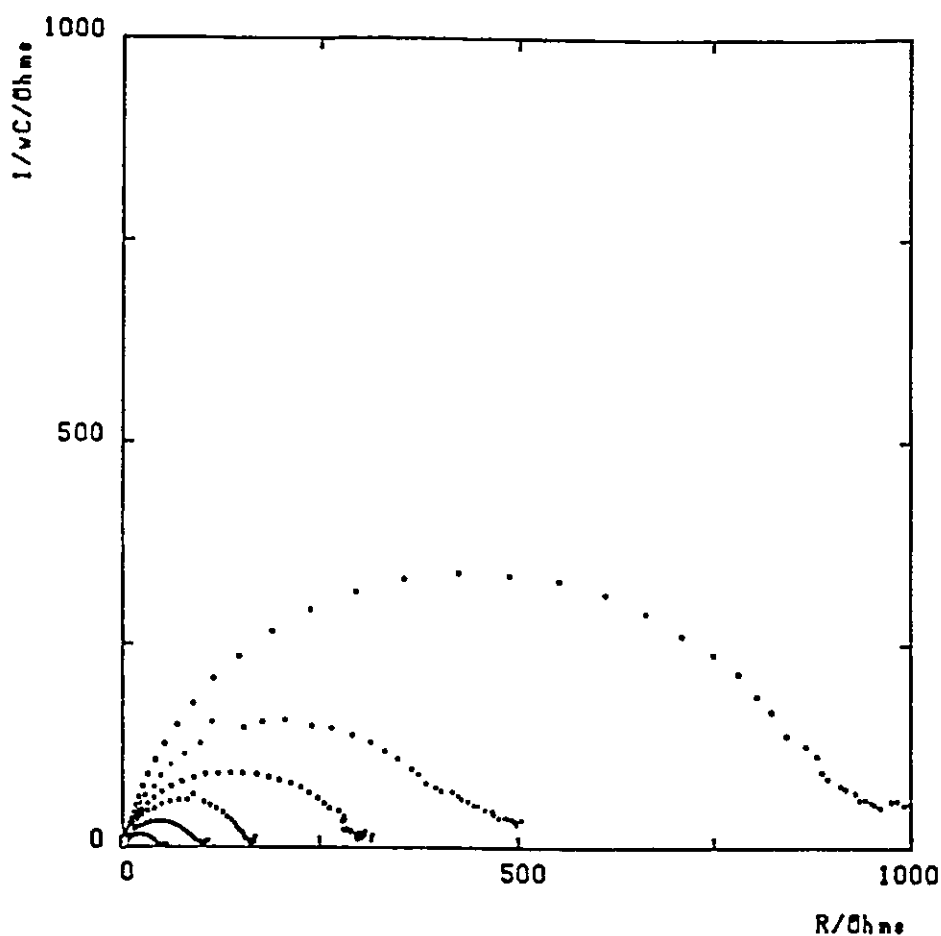
Figure 3.2

Impedance loci for the same cell at six different temperatures showing how the diameter of the semi-circle increases with decreasing temperature. In all loci the frequency sweep goes from 60 kHz to 60 mHz with ten steps per decade. The temperature for the largest locus is -1.8°C and the temperatures go 4.2, 7.6, 14.0, 20.0 and 24.4 as the loci decrease in size.
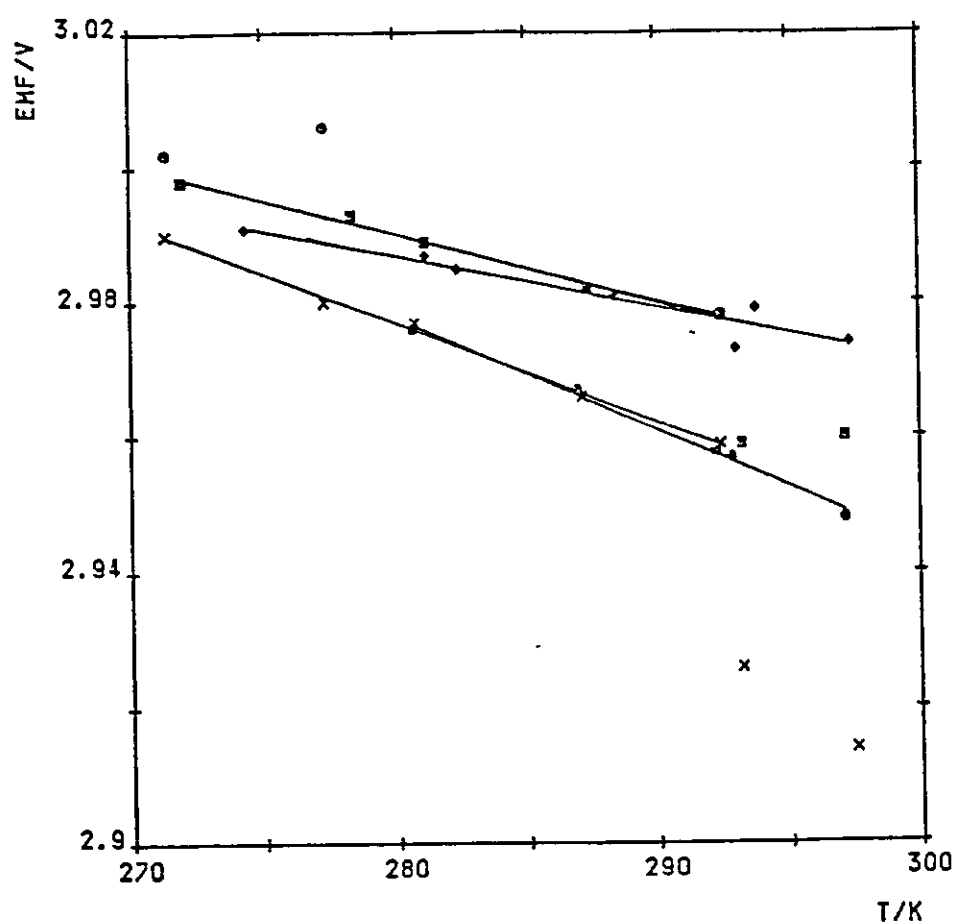
Figure 3.3

Plots of EvT for several cells. The slopes were calculated using the linear portions where possible but it can be seen that the plots give neither good straight lines nor parallel slopes.

3.3 Discussion

For the reaction

$$O + ne^- \longrightarrow R \qquad (2.2.1)$$

the exchange current density i_o is given by

$$i_o = nF \, k^o \, C_O^{1-\alpha} \, C_R^{\alpha} \qquad (2.2.25)$$

and

$$i_o = \frac{RT}{nF \, R_{ct}} \qquad (2.2.16)$$

where   n   is the valence charge number

         F   the Faraday constant

         k^o the specific equilibrium rate constant

         C_O concentration of O in (2.2.1)

         C_R concentration of R in (2.2.1)

         R_{ct} specific charge transfer resistance ($R_{ct} = \xi \times \theta$)

         α charge transfer coefficient

         ξ surface area of electrode

the anodic reaction can be written as

$$2Li + S_2O_4^{2-} \longrightarrow Li_2S_2O_4 + 2e^- \qquad (3.2)$$
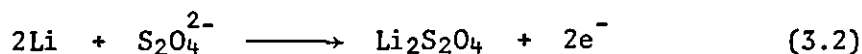
and equations 2.2.25 and 2.2.16 become

$$i_o = 2F \, k^o \, C_{Li_2S_2O_4}^{1-\alpha} \, C_{Li}^{2\alpha} \, C_{S_2O_4^{2-}}^{\alpha} \qquad (3.3)$$

and

$$i_o = \frac{RT}{2F\theta\xi} \qquad (3.4)$$

As k^o is a rate constant, an Arrhenius equation

$$k^o = A \exp\left\{ -\frac{\Delta U^{act}}{RT} \right\} \qquad (3.5)$$

can be written where A is the pre-exponential factor and ΔU^{act} is the activation energy at constant volume. Since the cell is a closed vessel, the pressure is certainly not constant but varies from 10 to 60 PSI in the temperature range used. Equations 3.3 and 3.5 are then combined and the logarithm is taken to give

$$\ln \left\{ 2FA\ c_{Li_2S_2O_4}^{1-\alpha}\ c_{Li}^{2\alpha}\ c_{S_2O_4^{2-}}^{\alpha} \right\} - \frac{\Delta U^{act}}{RT} = \ln \left\{ \frac{RT}{2F\theta} \right\} - \ln\xi$$

(3.6)

For the same cell in the same state of charge the only variables are T and θ. So equation (3.6) indicates that a plot of $\ln\left\{\frac{RT}{2F\theta}\right\}$ vs. $^1/T$ should give a straight line of slope $-\frac{\Delta U^{act}}{R}$. The results of this plot for each cell are shown in Table 3.1 and the plots themselves in Fig. 3.4. The slopes for each cell are in fairly close agreement with a mean value of -8600 ± 500 which gives a value of ΔU^{act} as 72 ± 4 kJ mol^{-1}.

The variation of the open circuit potential with temperature (from which the thermodynamics of the reaction is obtained) was also investigated and the results are shown in Fig. 3.3.

Since

$$\left(\frac{\partial A}{\partial T}\right)_V = -S$$

(3.7)

and $\qquad \Delta A = -EF$ (3.8)

where A is the Helmholtz free energy, S is the entropy and E is the equilibrium potential.

We have

$$\left(\frac{\partial E}{\partial T}\right)_V = \frac{\Delta S}{2F}$$

(3.9)

So plotting E vs. T should give a straight line of slope $\frac{\Delta S}{2F}$ for the present 2-electron process. The results of this plot are shown in Table 3.1. The mean value of these slopes is $(-1.6 \pm 0.2) \times 10^{-3}$ VK^{-1}. So $\Delta S = -300 \pm 40$ J mol^{-1} K^{-1}. As can be seen, these plots have linear portions. Occasionally the potential was observed to drop suddenly and then recover. This was interpret ed as corresponding to the rupturing of the passivating film caused by the performing of the impedance experiment (experimental programme - see above) followed by a slow repassivation. This is supported by observations of the low
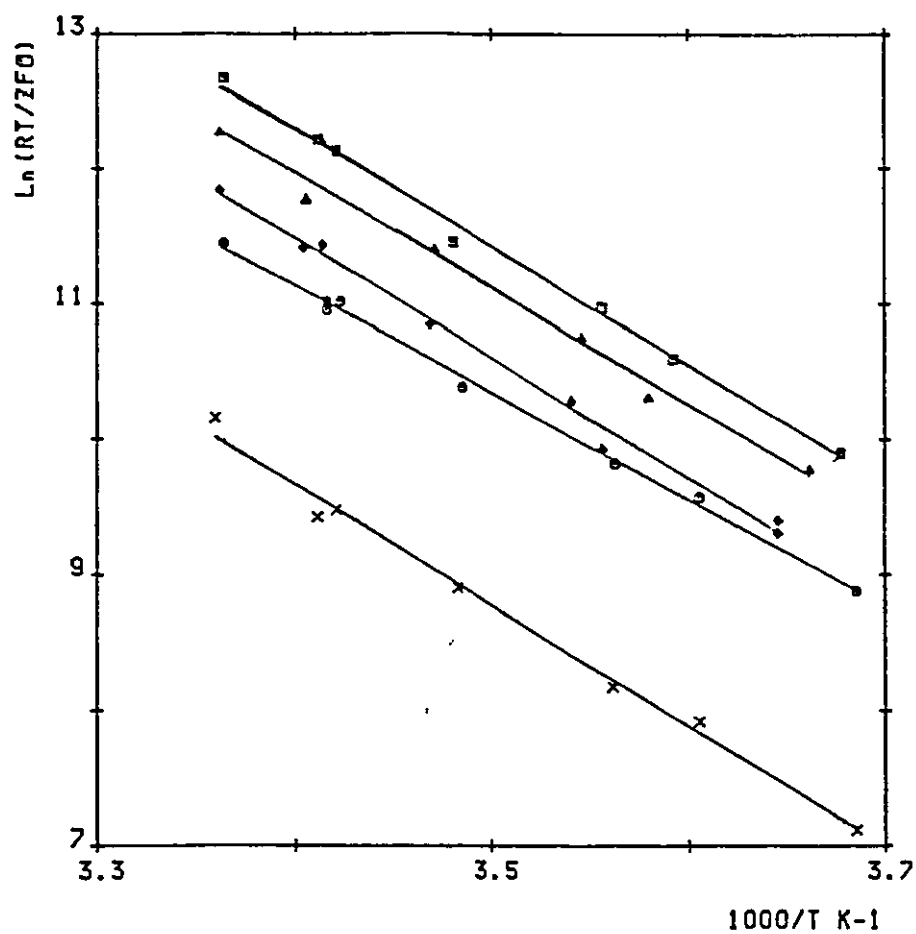
Figure 3.4

Plots of ln (RT/ZFθ) vs ^{1}/T for five cells all showing good fits to a straight line and nearly parallel slopes.

frequency electrode impedance. The slope of the Warburg line coming off from the high frequency semi-circle was observed to fall when the potentials dropped and then increased when the potential recovered to a value greater than 45° which indicates the presence of a film. It was not possible to ascertain the cause for the behaviour in this sequence of experiments. The outcome of this is that the values of the slopes for each cell are not always in very close agreement and thereby reduces the confidence which can be placed in the values of ΔS calculated.

It is interesting that, inspite of the uncertainties inherent in the thermodynamic estimations, the kinetic charge transfer resistance, θ, is independent of these variations in potential as all the cells gave very good straight line plots defining the characteristic activation energy, moreover these energies agree very well with each other.

3.4 Conclusions

Results indicate that, although the open circuit potential is occasionally uncertain due to film formation and subsequent disturbance on the anode, the charge transfer resistance, θ, seems to be relatively insensitive to these variations and this indicates that the properties of the cell in use, i.e. when current is being drawn, will have considerable predictability over an extended temperature range.

TABLE 3.1

CELL	VK^{-1} EvT $\times 10^{-3}$	ln (RT/ZFθ) v ^{1}/T
A	-0.77 ± 0.3	-8900 ± 800
B	-1.02 ± 0.1	-8800 ± 700
C	-3.29 ± 0.7	-8600 ± 1800
D	-1.68 ± 0.2	-7900 ± 500
E	-1.47 ± 0.1	-8900 ± 900
mean	-1.6 ± 0.2	-8600 ± 500

Summary of slopes of the plots of EvT and ln(RT/ZFθ) v ^{1}/T for
five cells. Cells A, B and C are G52 size and D and E are G4 size.

CHAPTER IV

THE USE OF THE A.C. IMPEDANCE TECHNIQUE TO INVESTIGATE CELLS AT
DIFFERENT STATES OF CHARGE

4.1 Introduction

Hughes et al [36,37] have reported an impedance study of small
Li/SO$_2$(C) cells (LO 32 S units manufactured by Duracell Batteries Ltd.)
containing an acetonitrile based electrolyte solution over a range of
states of charge.

The cell behaviour was described on the evidence of a relatively
simple impedance locus (out-of-phase component of the electrode
impedance displayed against the in-phase component). The assumption
that the lithium was the more irreversible of the two electrodes was
considered to be correct since the impedance data conformed to a
simple Randles conversion for charge-transfer followed by diffusion in
solution. Moreover the changes in the impedance with reactant
concentration varied in the manner expected for a system in which the
lithium dominated the cell behaviour. Specifically from the change
in the charge transfer resistance, θ, (corrected for the effective
anode area) as the cell discharged, an estimation of the charge
transfer coefficient for the Li$^+$/Li exchange in the acetonitrile-SO$_2$
solution (0.37) was made. (The product θC_{dL} of the apparent charge
transfer resistance θ and the double layer capacitance C_{dL} was found
to be a very good assessment of the residual capacity of the cell.

It has since emerged, from monitoring the performance of other
commercially produced Li-SO$_2$(C) cells, that the previously reported
behaviour [36] is not consistent throughout the range of manufacturers.
For example, differences in the impedance of comparable units produced
by Crompton Parkinson Ltd. included an elongation in the charge
transfer semi-circle. This, together with the appearance of an
additional shape in the complex plane plot suggested that the
controlling mechanism of these cells' behaviour might be consistent
with a porous electrode at which adsorption was a significant process.
It was decided that the most convenient was to obtain a detailed
study of the system was to incorporate a third (reference) electrode
within the cell and so obtain the component (impedance) behaviour of
both electrodes.

4.2 Experimental Procedure

The experimental set up for measuring the impedance spectra was
the same as that described in the previous chapter except the
reference electrode input to the 1186 Electrochemical Interface REI
was connected to the reference electrode of the cell instead of
being shorted to the counter electrode input SE (see Fig. 3.1).

The cells used were Vidor Eternacell size G20 (capacity 7.5 Ah,
rated load 1000 mA) specially modified to contain a lithium reference
electrode. This was introduced into the cell via glass seals on the
plane end of the cy,lindrical unit so that it lay tightly sandwiched
between the anode and cathode but isolated from both by the micro-
porous polypropylene separator. As such, it formed a rather complex
thin layer cell.

The cells were discharged galvanostatically at 1A for periods of
30 min. and allowed to equilibrate for three days before any impedance
measurements were made.

The impedance spectra of the anode with respect to the reference
electrode, and the cathode with respect to the reference electrode,
were obtained after each discharge step. In this way, 15 states-of-
charge were investigated. In order to confirm that the third
electrode was behaving as a true reference electrode, the two
spectra were added together point by point, vectorially, and compared
with the impedance of the whole cell. Fig. 4.1 for the undischarged
cells shows this to be the case.

4.3 Results and Discussion

Figure 4.1 shows that the anode and cathode impedances which go
to form the total cell impedance are of the same order of magnitude
although, in general, that of the cathode was somewhat greater. Thus
these particular cells were rate-controlled by both anode and cathode
and it is not possible to ignore either electrode in a consideration
of the cell behaviour.

The impedance plots of the cathode with respect to the
reference were fitted to a model using the Taylor theorem approach
[35] and the component processes isolated [38,39]. The model
consisting of a Randles circuit modified for electrode roughness and
porosity used by Hughes [36] did not give a sufficiently good fit in
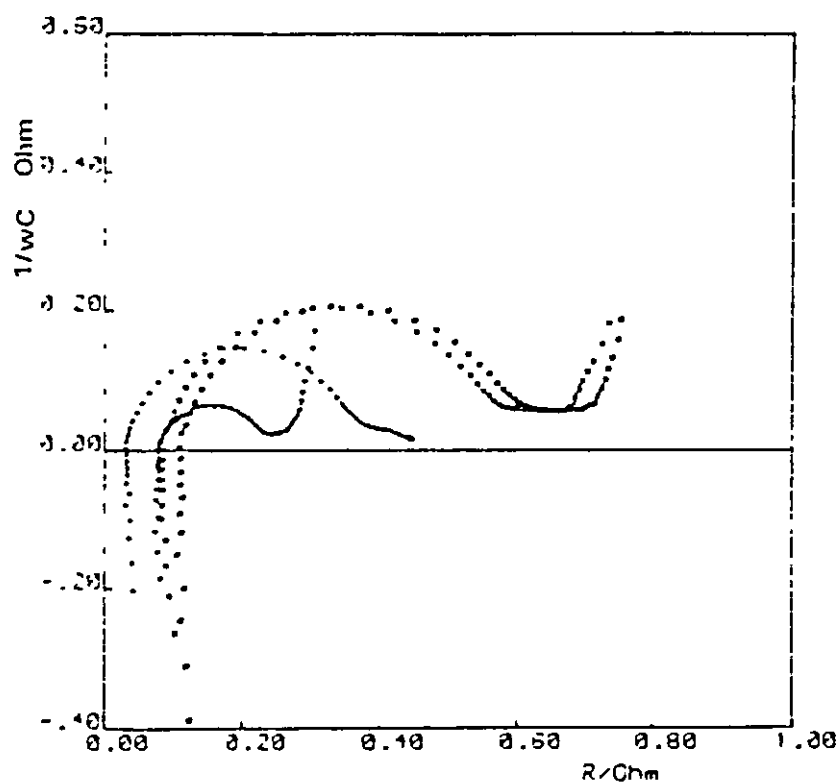the present cases. The best fit was found by modifying this model

Figure 4.1   Cell and Electrode Impedances

+ —— Li/Ref.

∇ —— C/Ref

X —— Li/C cell

☐ —— Impedance sum Li/Ref + C/Ref. (Slight difference from
link cell impedance due to experimental self perturbation).

to incorporate adsorption on the cathode surface [40]. The presence
of a dielectric film on the surface [39] was represented by a series
capacitance C_s. It was not found necessary to associate a resistance
parallel with C_s in order to decompose our results (for an electrode
perturbation greater than the 3 mV used in these experiments or for
frequencies approaching d.c. operation this would have been necessary).
A series inductance was also added to account for effects which arise
from the cell geometry and internal connections. A circuit analogue
for this model is shown in Fig. 4.2.

The isolation of the 9 circuit elements demanded that as many
frequency values as (reasonably) possible to be investigated. In this
case 60 were used, which gave sufficiently precise values of the
components to be estimated with an acceptable least squares variance
of the computed values.

Fig. 4.3 shows a typical example of the experimental data with a
fitted curve. The validity of the model was confirmed by the
excellence of the fits obtained for all states of charge.

Computed equivalent circuit component values are given in Table
4.1.

The variations of the components as charge is withdrawn from the
cell is interesting and yields information regarding the cathodic
processes. The double layer capacitance, C_{dL}, has an initially low
value corresponding to the presence of an intruding film of lithium
dithionite on the surface. This masking film very rapidly breaks on
discharge to yield a relatively constant active surface. The value
of C_{dL} rises to a maximum of $\sim 4 \times 10^{-2}$F just before the cell is
completely discharged, then falling to a value of 3×10^{-3}F. This
great increase in electrode capacitance towards the cell exhaustion
point possibly indicates the break-up of the cathode; the intrusion
into the inner regions of the carbon crystallites leading to the
final passivation of the electrode. This picture is supported by the
parameters C_s, R_p, C_p which all indicate the break-up of the cathode
structure as available charge in the cell is exhausted.

The charge transfer resistance, θ, is complementary to the
series and double layer capacitances C_s and C_{dL}. Initially high,
indicating the presence of a retarding film, θ rapidly falls on the
removal of charge from the cell becoming more or less constant at
0.05Ω throughout the whole of the region of useful discharge. This
again suggests that the initially protective film is readily removed
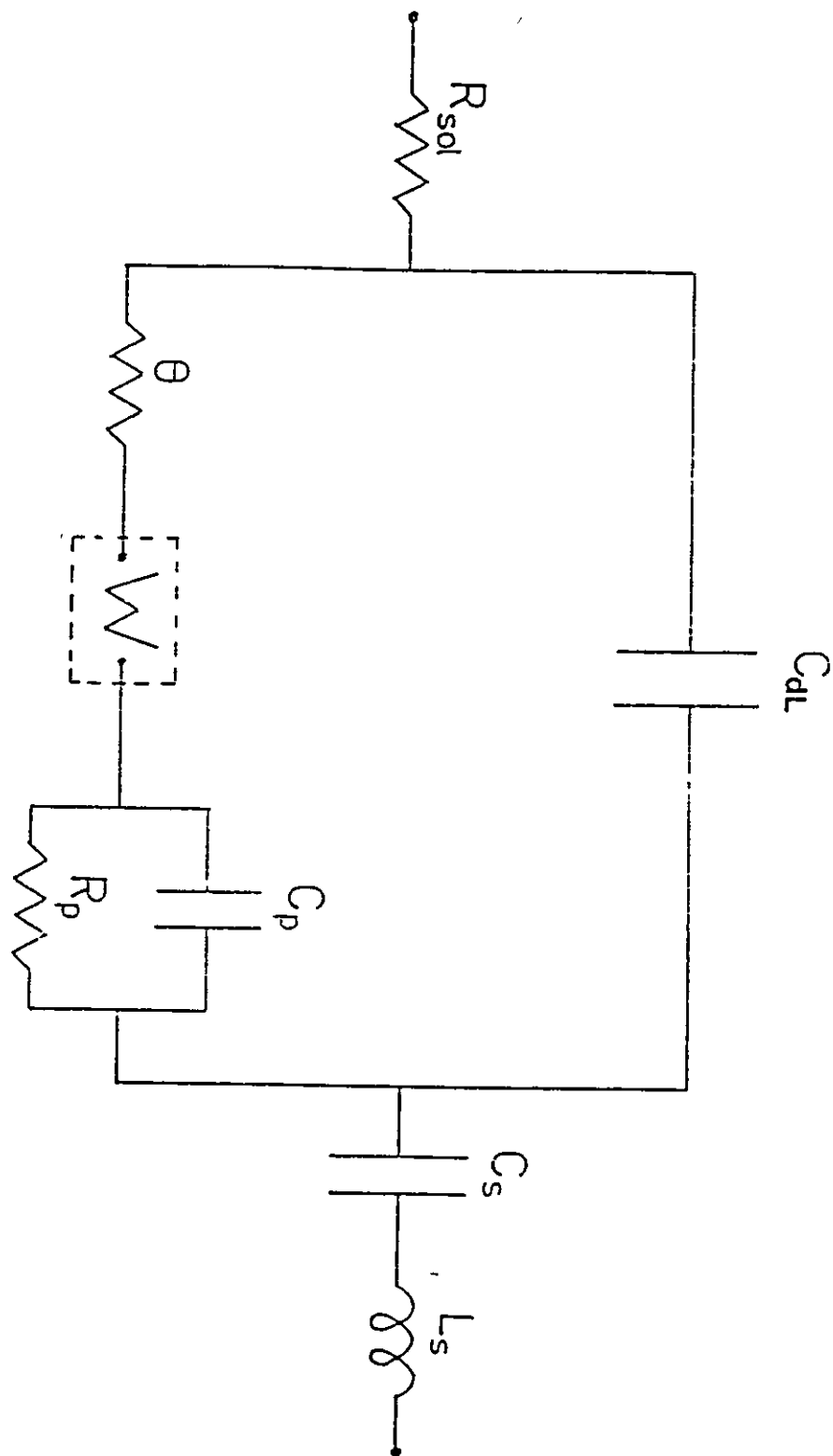and that the reduction of SO_2 occurs at a surface of approximately

Figure 4.2   The Analogue for the Carbon Electrode

θ - charge transfer resistance

C_{dL} - double layer capacitance

R_{sol} - solution resistance

W   - Warburg impedance

C_S - film capacitance

L_S - contact inductance

C_P - "intermediate" reaction capacitance

R_P - "intermediate" reaction resistance
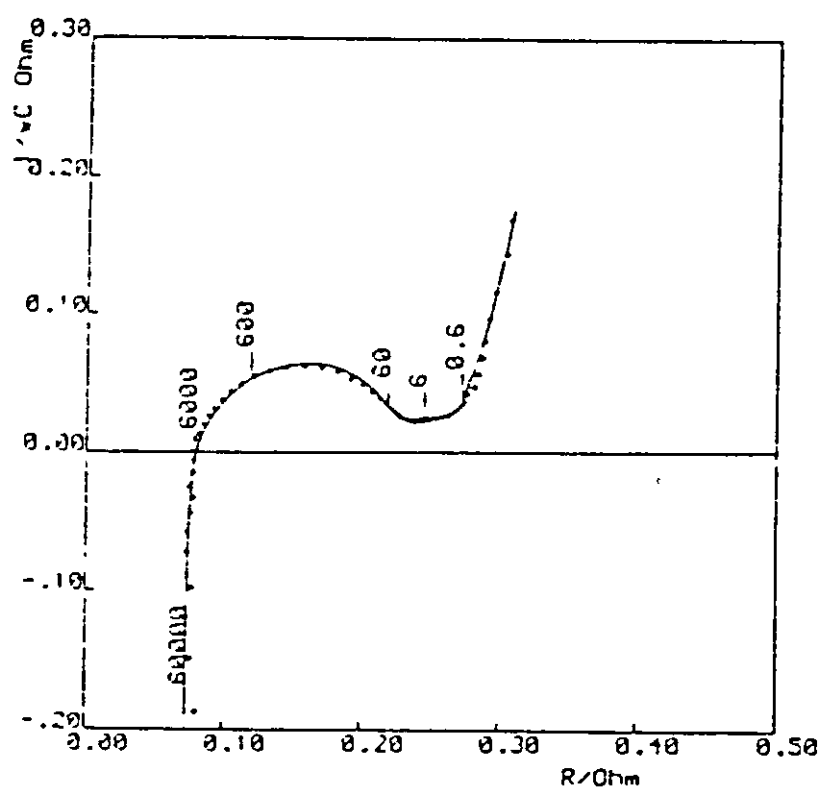
Figure 4.3   Typical Curve Fitted to the Experimental Data for the
              Cathode

+   Experimental points
___   Computed curve

constant active area. This picture is again confirmed by σ the
Warburg coefficient which written for:

$$O + ne^- \rightleftharpoons R, \qquad\qquad (2.2.1)$$

$$\sigma = (\sqrt{2}/2)(RT/n^2F^2)[C_O\sqrt{D_O})^{-1} - (C_R\sqrt{D_R})^{-1}] \qquad (2.2.74)$$
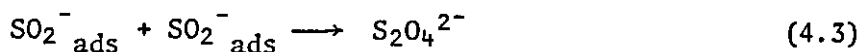
for the present system in which $Li_2S_2O_4$ is fairly insoluble and the
other reactants are in excess this equation becomes:

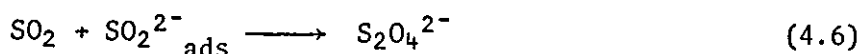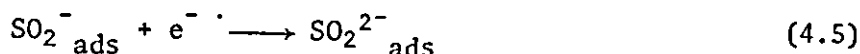$$\sigma = (1/\sqrt{2})(RT/n^2F^2)(AC_R\sqrt{D_R})^{-1}. \qquad\qquad (4.1)$$

Where C_R and D_R represent the concentration and diffusion coefficient
of $S_2O_4^{2-}$ and A is the effective area of the electrode. In the
present case the diffusing area of the electrode is relatively low
initially and on discharge rises to a fairly constant value.

The inductive component of the electrode impedance is clearly a
complex quantity. This, in our opinion, is most likely linked to
physical geometric modifications within the cell which occur as a
consequence of volume changes within the carbon. This material is
disposed on an aluminium mesh and it is reasonable to ascribe the
major part of the inductive component to this source.

The need for the parallel (Rp-Cp) circuit in the analogue
representation is interesting for it was not needed in the earlier
investigations [36]. It represents the presence of some process in
the cathode reaction which exerts a significant current control in
the experimental frequency range. The presence of an adsorbed
intermediate such as SO_2^- or SO_2^{2-} at the electrode or reactions of
the type

$$SO_2 + e^- \longrightarrow SO_2^-{}_{ads} \qquad\qquad (4.2)$$

$$SO_2^-{}_{ads} + SO_2^-{}_{ads} \longrightarrow S_2O_4^{2-} \qquad\qquad (4.3)$$

or

$$SO_2 + e \longrightarrow SO_2^-{}_{ads} \qquad\qquad (4.4)$$

$$SO_2^-{}_{ads} + e^- \longrightarrow SO_2^{2-}{}_{ads} \qquad\qquad (4.5)$$

$$SO_2 + SO_2^{2-}{}_{ads} \longrightarrow S_2O_4^{2-} \qquad\qquad (4.6)$$

would imply the observed reaction model, however, it is not possible in this investigation to decide which of these (or others) is the appropriate mechanism. However, the interesting point is in the qualitative differences between this and the previous investigation indicates significant behaviour differences among the various available carbons (and catalysed carbons). A final point which arises from the work is, that whilst the product θC_L was a useful parameter for residual capacity assessments for certain cell types it was very insensitive in this case (Table 4.1).

4.4 Conclusions

(i) The impedances of both anode and cathode are of the same order.

(ii) The cathode could be represented by a complex model based on charge-transfer and diffusion with allowance for adsorption and electrode films.

(iii) At high frequencies the geometry of the system gives rise to an inductive branch in the impedance locus.

(iv) Initially the cathode is covered by a thin layer, probably of $Li_2S_2O_4$. This is partially removed on discharging.

(v) There is evidence of serious cathode disruption when the cell has been drained of useful charge.

(vi) There is strong evidence for adsorbed intermediates on the porous carbon cathode matrix.

TABLE 4.1
Computed equivalent circuit component values as a function of charge removed.

Charge removed (A h)	R_{sol} (10² Ω)	θ (Ω)	C_{dl} (10³ F)	σ (10² Ω s⁻¹ᐟ²)	Roughness factor (γ)	C_s (F)	L_s (10⁸ H)	R_p (10² Ω)	C_p (F)	$θC_{dl}$ (10⁴ S)
0	3 3	0 62	0 5	13 1	0 620	33 0	68 3	13 5	0 1	3 6
0 5	5 5	0 11	8 5	3 6	0 460	16 0	68 0	1 5	2 1	9.9
1 0	7.5	0 05	14 0	2 0	0 540	14.5	56 0	1 0	0 5	7.5
1 5	6 6	0 07	8 5	2 4	0 685	16 5	57.2	1 5	0 3	6 0
2 0	6.1	0 07	9 6	2 2	0 665	15 0	59 2	1 5	0 3	6 0
2 5	6 7	0 08	3 0	3 0	0 885	18 0	65 0	1 5	0 55	7 2
3 0	6 2	0 07	10 0	2 8	0 700	18 0	53 5	3 0	0.01	2.7
3 5	8 5	0 05	10 0	2 2	0 710	18 5	54.4	1.5	0.7	7.3
4 0	6 4	0 05	10 5	2 8	0 700	19 0	54.4	1 0	0.8	6 0
4 5	6 6	0 035	12 0	2 0	0 685	20 5	66.4	1 0	1 2	6.1
5 0	7 1	0 06	11 0	2 9	0 680	17 5	53 5	0 5	2 3	5.1
5 5	6 8	0 03	16 5	2 2	0 640	21 5	56 2	1 5	1 5	7.2
6 0	6 3	0 06	16 5	1 4	0 585	19 0	62 2	1 0	2 7	4.7
6 5	6 4	0 02	41 0	4 8	0 475	21 5	61 2	3 0	1.7	10.1
7 0	8 2	0 035	3 0	29 4	0 700	63 0	51 8	2 0	7 3	7 0
								31 0	1 6	1.1

CHAPTER V

THE USE OF THE A.C. IMPEDANCE TECHNIQUE TO INVESTIGATE PROCESSES IN
CELLS AFTER CHARGING

5.1 Experimental Procedure

In order to investigate the effects of charging on both anode and
cathode cells with reference electrodes, identical to those described
in the previous chapter, were used.

The procedure for the obtaining of the impedance spectra was also
the same as the previous chapter.

The cells were charged galvanostatically at rates ranging from
1 ampere to 6 amperes for periods up to 30 minutes.

The impedance spectra and open circuit potentials were
obtained before charging and at various recovery times afterwards.

Only charging at the highest rate of 6 amp when cells would get
very hot and eventually vent or explode caused any safety hazard.

5.2 Results and Discussion

On charging the open circuit potential increased from 2.99 V for
a new cell to 3.50 V, which was independent of the total charge
passed provided it was at least 1 A minute. The potential then
decayed over a period of several days to its original value of 2.99 V.

Figs. 5.1 - 5.2 show spectra for a new cell and fig. 5.3 - 5.4
show spectra typical of many obtained after different amounts of
charging and recovery times (between which there was very little
variation).

Even though the potential may have returned to its original value
the impedance spectra did not return to those of the new cell, and
in fact, performing the impedance experiment caused the cell potential
to rise to the value after charging.

Comparing the spectra of a cell before and after charging
several quite dramatic changes can be seen to have occurred:

(1) The size of the anode spectrum is now much smaller and is no
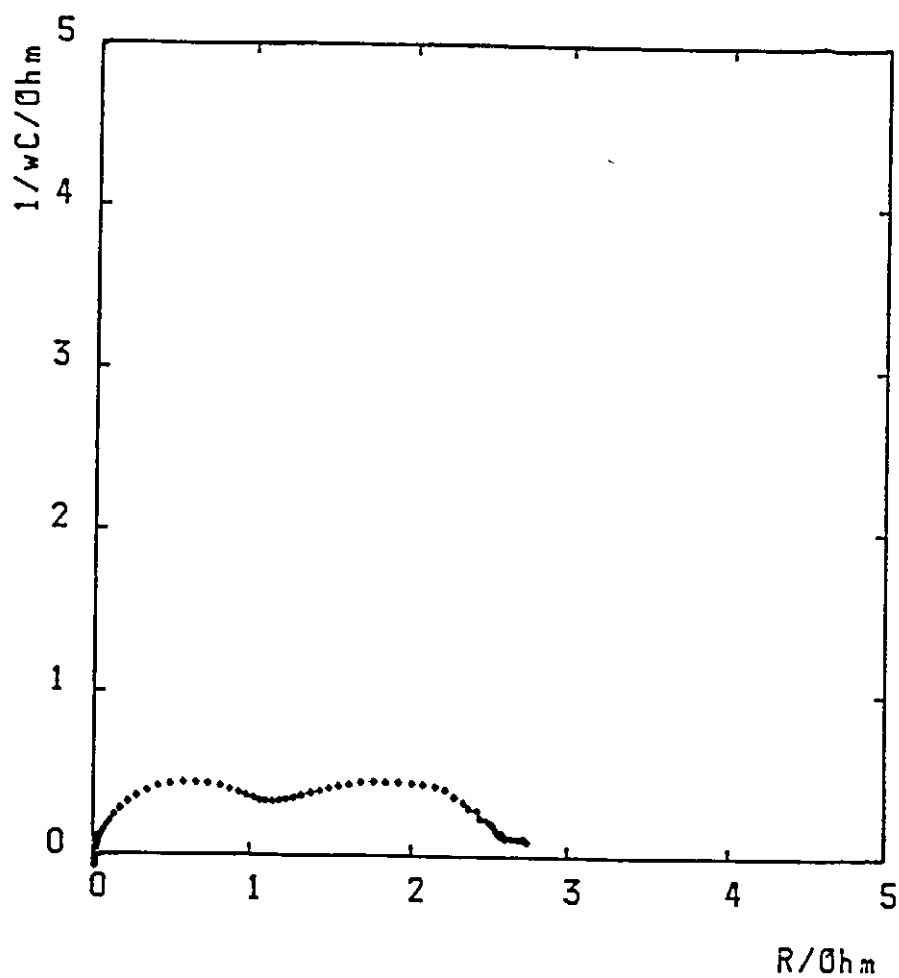longer significant compared to the cathode.

Figure 5.1

Impedance spectrum for the anode with respect to the reference
for a new cell. The frequency sweep in this and all other spectra
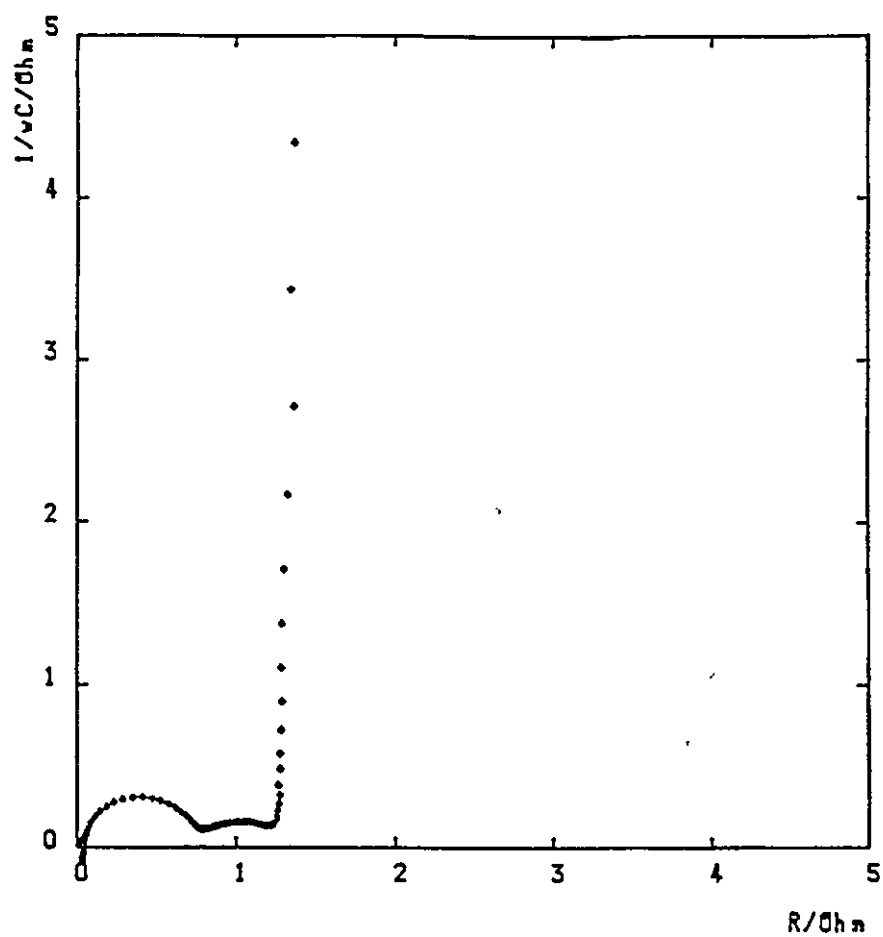goes from 60 kHz with ten steps per decade.

Figure 5.2

Impedance spectrum for the cathode with respect to the reference for a new cell.
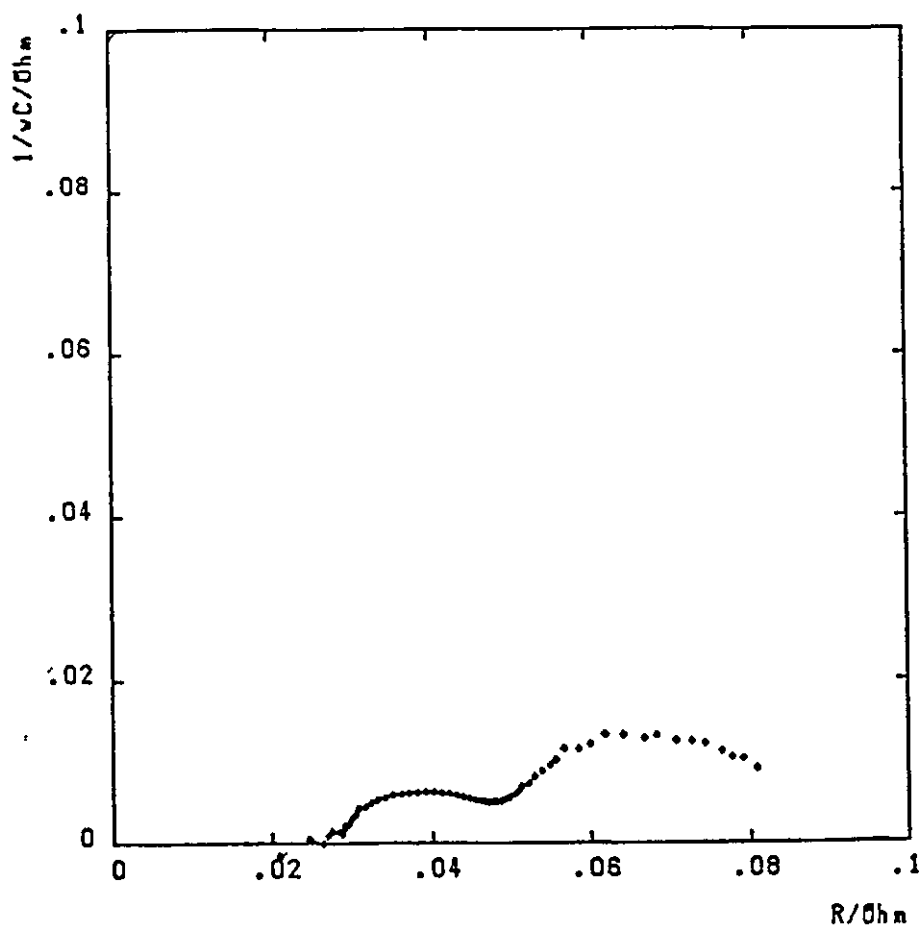
Figure 5.3

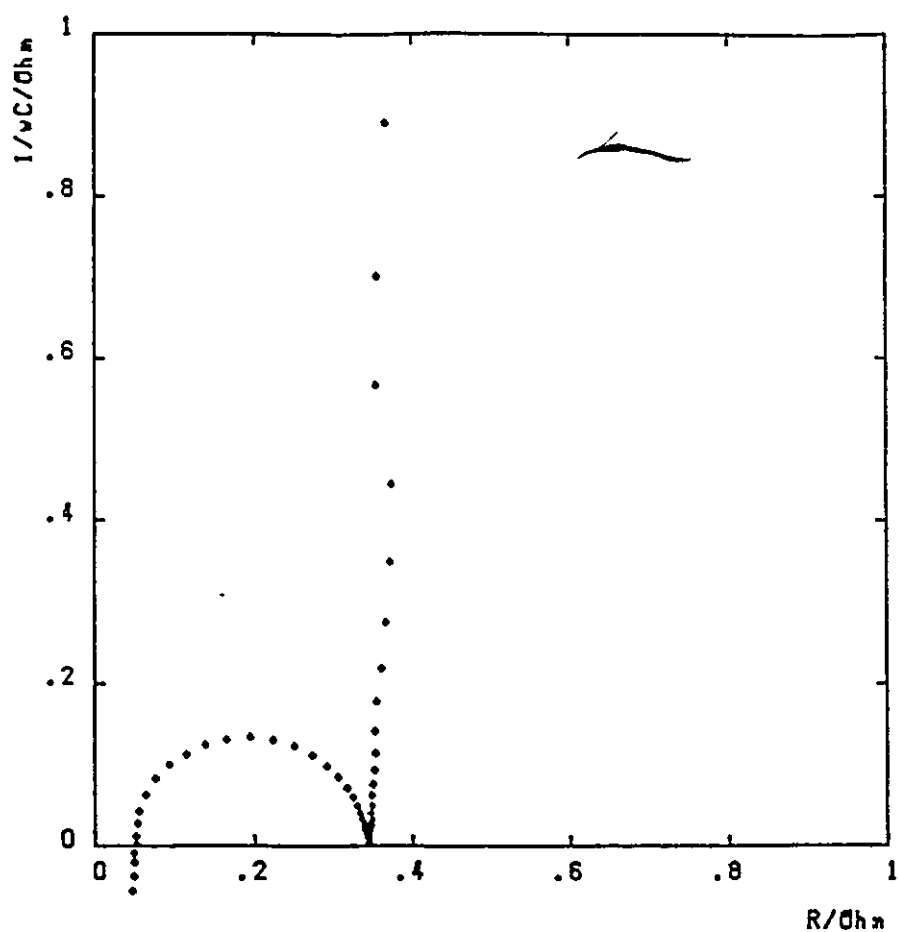   As Fig. 5.1 except for the cell being charged slightly.

Figure 5.4

    As Fig. 5.2 except for the cell being charged slightly.

(ii) The cathode spectrum is also reduced in size, but not by as much as the anode. Another difference is that the spectrum now consists of one semi-circle instead of two.

The anode is a simple metal/metal ion exchange across the metal solution interphase in a thin layer cell. Thus a semi-circle is followed by a Warburg shape which returns to the real axis at low frequency. The diameter of the semi-circle is quite large before any charge is removed from the cell; after this has occurred the diameter shrinks considerably. This can be interpreted if a film of lithium dithionite initially masks the electrode and is stripped away as soon as reductive charge passes across the electrode.

The cathode behaviour clearly shows evidence for two processes which constitutes the electrode process which is blocked for one of the electrode species. This latter conclusion follows from the vertical line which constitutes the impedance plot at low frequency. This is almost certainly associated with the difficulty of reconverting the dithionite ion back to SO_2. Thus the sulphur dioxide reaction is a two-step process, the second stage involving the production of an intermediate.

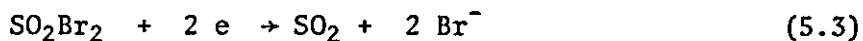The reaction at the carbon electrode, which occurs when the electrode is oxidised anodically must initially be

$$2 \ Br^- \ \rightarrow \ Br_2 + \ 2 \ e^- \qquad\qquad (5.1)$$

Since no dithionite is available for oxidation, the bromine is removed by reaction with SO_2 present in the electrolyte,

$$SO_2 \ + \ Br_2 \ \rightarrow \ SO_2Br_2 \qquad\qquad (5.2)$$

to form sulphuryl bromide which itself provides an effective depolariser for the lithium system. The reduction of sulphuryl halides is very complex. Numerous products which affect the stability of the system have been reported. However, it seems likely that the main depolarising reactions at the electrode are

$$SO_2Br_2 \ + \ 2 \ e \ \rightarrow SO_2 + \ 2 \ Br^- \qquad\qquad (5.3)$$

and

$$Br_2 \ + \ 2 \ e \rightarrow 2 \ Br^- \qquad\qquad (5.4)$$

It is probably reaction (5.3), with SO_2Br_2 adsorbed at the carbon electrode, that provides the relatively stable open circuit potential of 3.50 V. The overall reaction at this high potential is therefore

$$SO_2Br_2 \;+\; 2\ Li \;\underset{\leftarrow}{\rightarrow}\; SO_2 \;+\; 2\ LiBr \qquad\qquad (5.5)$$

The impedance spectra will clearly be affected by the presence of these oxybromine species and the changes observed in these spectra are due to this cause. It is not possible to check unequivocally the identity of the bromine species (which may indeed by transitory) in the present experiments.

The charge transfer resistance, R_{ct}, is given by equations 2.2.16 and 2.2.25

$$R_{ct} \;=\; RT/(n^2F^2k^oC_R{*}^\alpha C_o{*}^{1-\alpha}A) \qquad\qquad (5.6)$$

So for the reaction at the cathode (5.3) the charge transfer resistance will be given by

$$R_{ct} \;=\; RT/(2^2F^2k^o[SO_2Br_2]^{1-\alpha}[SO_2]^\alpha[Br^-]^{2\alpha}A) \qquad\qquad (5.7)$$

The high concentration of LiBr and SO_2 within the cell will ensure a relatively small value for R_{ct}. For the new cell (uncharged) the reaction at the cathode is

$$2S\ O_2 \;+\; 2e^- \;\rightleftharpoons\; S_2O_4{}^{2-} \qquad\qquad (1.9)$$

and R_{ct} will be given by

$$R_{ct} \;=\; RT/(2^2F^2k^o[SO_2]^{2(1-\alpha)}[S_2O_4{}^{2-}]^\alpha A) \qquad\qquad (5.8)$$

the concentration of $[S_2O_4{}^{2-}]$ will be very low, causing R_{ct} to be large.

Comparison of figures 5.2 and 5.4 does indeed show that the diameter of the first semi-circle and hence the charge transfer resistance is smaller for the charged cell.

Comparison of the impedance spectra at the anodes, figures 5.1 and 5.3, shows there is about a fifty-fold decrease in the size of this impedance spectrum after charge and this can only really be

- 39 -

explained by a fifty-fold increase in effective area of the lithium electrode due to the removal of film, probably $Li_2S_2O_4$. The other semi-circle in both impedance spectra of the anode, is probably the Warburg impedance returning to the real axis.

5.3 Conclusions

The fact that it is possible to charge the Li/SO_2 system from its 'fully' charged' state in comparative safety, provided that care is taken, suggests that the further activation of the Li/SO_2 cell is a commercial possibility.

CHAPTER VI

THE RAPID ESTIMATION OF IMPEDANCE USING PSEUDO-RANDOM NOISE

6.1 Introduction

Previous publications [41-43] have shown that the impedance data
of electrolytic cells can be used to yield useful electrode kinetic
and stored charge assessment data. The hardware designed for the
measurement of different parameters indicating these characteristic
quantities for a range of cells have been described [44,45]. These
tests were based on impedance measurements at one or two frequencies.
More accurate and reliable estimations could be made, if there is
more data available over a range of frequencies, around a specific
portion of the cell impedance spectrum, as recently observed [46] in
the case of sealed lead-acid cells with specific aircraft applications.
The equipment used for this purpose should be compact and produce the
impedance data over the required frequency range within a short time.
The conventional impedance measurement apparatus operating at single
frequencies as Frequency Response Analysers (FRA) would be bulky,
too slow and expensive for this purpose.

Since the perturbation signal generated by an FRA is
sinusoidal, the impedance data obtained during a single measurement
would be limited to a specific frequency and the duration of the
measurement should at least be equal to the time period of the A.C.
signal. The execution time of a frequency sweep would therefore be
equal to the sum of sampling times the FRA spends at each individual
frequency. · If the perturbation signal contained a number of
frequencies, as in the case of random noise, the cell voltage and
current response acquired over the time period of the lowest frequency
component of the signal would provide cell characteristics of more
than one frequency in a single data acquisition. The number of
frequencies studied will be equal to the number of harmonics
contained in the perturbation signal and will range from the
frequency of the fundamental up to the highest harmonic, which in
turn depends on the duration of the data acquisition. The subsequent
impedance calculations via the Fourier Transformation of cell

response are carried out without the need for the cell being
connected to the apparatus. The processing time depends on the
lengths of the data arrays, efficiency of the computational algorithms
and the hardware but not on the number of frequencies contained in the
signal. Since the total time required is independent of the number of
frequencies unlike the single frequency sinusoidal measurement, the
use of random noise seems to be advantageous in the cases where the
speed of measurement is important.

Mini-computers have been employed previously [47-49] for this
purpose, using different random noise techniques [50-52]. Due to
high costs and large sizes, it is not possible to incorporate these
computers and noise generators into test equipment. In this chapter
the implementation of random noise impedance measurements on a Z80
based 64 k byte micro-computer is described. It was also envisaged
that such a system could eventually be installed in a unit
dedicated for general on-line applications.

6.2 Instrumentation

The hardware for the measurement of impedance using random noise
should consist of a noise generator, a potentiostat for the perturbation
of the cell potential and a recorder for the acquisition of the
voltage and the current response of the cell as a function of time.
The time domain cell responses have to be transformed to the frequency
domain via a Fourier Transform prior to the calculation of the
impedance and this demands sufficient computational capability
associated with the experimental set-up. As prototype test equipment
for the implementation of this technique an electrochemical interface
(Solartron 1186) was used as the potentiostat and the noise generation,
data acquisition and the computations were carried out on a Z80 based
micro-computer (Kemitron 3000) equipped with a 12 bit bipolar
digital to analogue converter (DAC) with full scale output of ± 1.023V
and settling time 1ns and two 12 bit bipolar analogue to digital
converters (ADC) with adjustable gain amplifiers (x 10, 100, 1000)
with full scale input of ± 10.23V and conversion time 25 μs operating
under Digital Research CP/M environment. Start conversion input of
both ADC's were connected together such that start conversion command
given to one of the ADC's would also activate the other, enabling
the simultaneous reading of the voltage and current across the test
cell. The voltage output of the DAC was connected to the external

input (x1) of the potentiostat via a variable low pass filter (Barr and Stroud Ef2) which was tuned above the highest frequency component in the noise signal to avoid the steps of the 'stair case' type of digitally generated wave forms. Fig. 6.1 shows a schematic diagram of the apparatus used in this work. In the actual application however, a dedicated unit can be built around a micro-processor associated with an EPROM and a single card potentiostat with sufficient power.

6.3   Run Procedure

Prior to the experiment the open circuit voltage of the cell was backed by the polarisation control of the potentiostat and the d.c. levels of the voltage and current output signals were minimised using the built in controls of the 1186 interface. A number sequence representing a suitable random noise signal was created in the computer memory as described below or by the reading in of a previously created set of numbers from the magnetic disc. The data acquisition cycle consisted of the output of the above numbers through the DAC to perturb the cell potential and the simultaneous recording of the cell voltage and current response via the two ADC's and the procedure was repeated for all the numbers in the sequence. The period of the data acquisition, hence the frequency of the fundamental harmonic of the noise voltage was varied by the insertion of variable time delay between the output and input of voltages. The cell response data may be averaged, at the expense of time, to minimise errors due to parasitic noise by the repeated execution of the data acquisition cycle, after which the experiment ends and the cell may be disconnected.

The subsequent computation involved the Fourier transform of the two real valued data arrays containing the time domain representation of the cell voltage and current responses via a Fast Fourier Transform (FFT) algorithm to obtain the amplitude and phase of the respective signals as complex data at individual harmonics in the frequency domain. The cell impedance was calculated by the complex division of the frequency domain voltage data by current at each of the harmonics. Even though it was possible to calculate the impedance at all the harmonics resulting after the FFT, impedance calculations were limited to those harmonics originally incorporated in to the noise signal as the magnitudes at other harmonics were too small and contained mainly rounding off errors.
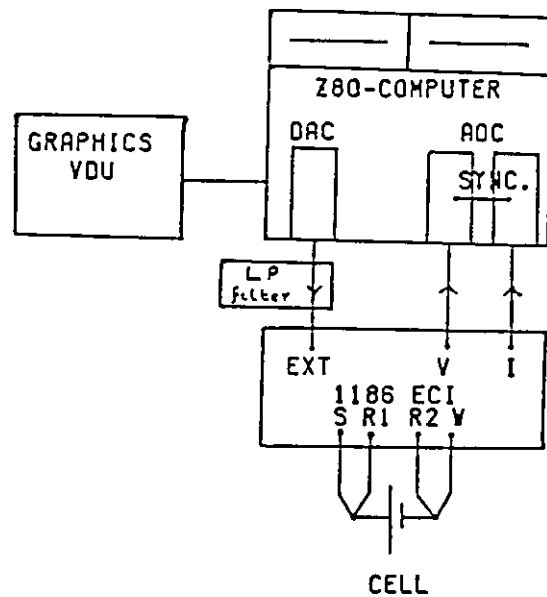
Figure 6.1   Experimental schematic diagram.

6.4   Theory

6.4.1   Fast Fourier Transform (FFT)

The Fourier transform of a set of N time domain numbers x_t, t = 0, 1,..N-1, is a set of N frequency domain components x_f, f = 0, 1..N-1, where

$$x_f = \sum_{t=0}^{N-1} x_t \cdot \exp(-i2\pi ft/N) \qquad (6.1)$$

and the inverse transform is defined as,

$$x_t = 1/N \sum_{f=0}^{N-1} x_f \cdot \exp(i2\pi ft/N) \qquad (6.2)$$

where $i = (-1)^{\frac{1}{2}}$. The Fourier transform calculated directly from equation 6.1 would involve N^2 number of complex multiplications and additions requiring about 800 seconds for a 512 point transform on a 8 bit micro-computer. In addition two data arrays x_t and x_f have to be created, increasing the storage requirements of the programme. An algorithm involving fewer computational steps, operating entirely within the array x_t to replace its original contents by the Fourier transformed values of x_f has been developed by Cooley and Tukey [53]. This required the splitting of the N numbers of x_t in to two N/2 long number sequences and the combination of the Fourier transform of the two half sequences to obtain the required result involving $(N^2+N)/2$, almost half the original number of operations. If N is an integer power of 2, i.e. $N=2^M$, then repeated splitting of the half sequences till they contain only one number and since the Fourier transform of a single number is the number itself, the total number of mathematical operations can be reduced to NM. In this case the repeated splitting of the data array reduces to the shuffling of data with their 'bit reversed' addresses within the data array as shown below for an array of 8 data points.

Original order	Binary	Reversed	Shuffled order
0	000	000	0
1	001	100	4
2	010	010	2
3	011	110	6
4	100	001	1
5	101	101	5
6	110	011	3
7	111	111	7

This shows that the data originally stored in location 1, for example must be exchanged with location 4 and so on. The shuffled numbers are manipulated according to the basic FFT algorithm involving a complex multiplication followed by an addition or a subtraction on pairs of points and the process is repeated M times. As the basic operation involved only 2 points, this is called the radix 2 FFT. The processing time can be reduced by the use of radix 4,8 etc. algorithms at the expense of programme memory. An important special case arises when the time domain number sequence is entirely real, as the cell voltage and current responses encountered in this work. The N element real valued data array can then be treated as a complex array of $N/2$ elements and the FFT of this followed by further $N/2$ operations [54] would enable the Fourier transformation of the real number sequence involving $(MN+N)/2$ operations compared to the original N^2. This procedure makes the computational time for a 512 point data array 100 times faster and does not require additional memory for the storage of intermediate and final results as all calculations are done within the original data array. Hence an FFT algorithm of radix 2 was adopted in this work for the Fourier transformation of the cell voltage and current data arrays.

6.4.2 Synthesis of Random Noise

The theory of FFT shows that the time taken for the transform depends on the number of data points in the time domain sequence. In view of the computational economy, both speed and storage, it is preferable to deal with smaller data arrays. However, according to the sampling theorem, all frequency components completely characterizable by any data acquisition process should contain at least

two points per cycle. Presence of higher harmonics containing less than 2 points per cycle in the time domain would give rise to erroneous frequency components called 'aliasing' during the FFT, which will be interpreted as a series of low frequency components. Thus for the perturbation signal to contain at least two decades of frequencies from the fundamental to the 100th harmonic, it should be made up of a minimum of 200 data points. Since the accuracy of the high frequency data increases with the number of points defining a cycle (>2), it was decided to include at least 4 points in the highest harmonic, making the data array contain 400 points. Since this number also should be an integer power of 2, the data arrays in this investigation contained 512 points making the highest harmonic to be the 128th.

The FFT of a 512 point time domain sequence would always give 512 components in the frequency domain with the lowest frequency and the frequency separation equal to the inverse of the data acquisition period. Whenever the time domain data contain incomplete number of cycles of a particular harmonic, its Fourier transform will consist of a principal component and a set of side bands which can interfere with actual components present in the data. This error known as 'leakage' can be easily avoided in the case of digitally generated wave forms by the exclusive use of integral numbers of harmonics in the signals.

In accordance with the foregoing remarks integers in the range 1-128 were used as harmonic numbers for the calculation of 512 point number sequence representing the noise signal. In order to give equal significance to all the frequency components their amplitudes were kept constant and each harmonic was associated with a random number in the range 1-360 as the phase angle. The calculation involved the summation of the function Sin (ωt + α) where ω is the angular frequency and α the phase angle for each of the harmonics over a period of 512 time intervals. Even though this procedure is relatively simple, the time taken for the calculation depends on the number of harmonics included in the signal and will be about 45 seconds for 15 harmonics. This may be unsuitable if the signal should contain more harmonics and repeatedly synthesised prior to the measurements. A more efficient method would be to represent the harmonics in the form of frequency domain data and perform the inverse Fourier transformation to obtain the required time domain data. This was done by placing zeros in a 512 element complex array and making the real and imaginary parts of the

elements corresponding to the required harmonics to be Cos α and Sin α respectively. The time taken for the inverse Fourier transformation of this array was about 11 seconds and independent of the number of harmonics present. Hence the latter method was used in this work for the calculation of the random noise signal. Either the real or imaginary parts of the resulted complex array can be used as the time domain sequence and the two differed only by a phase angle of 90°.

In order to avoid errors due to Faradaic non-linearity it is important to use low perturbation signal amplitudes, typically about 5 mV. Hence the time domain number sequence was scaled such that amplitude associated with each of the harmonic was 5 mV. Failure to impose this limit renders the interpretation of the impedance data impossible using the generally accepted electrochemistry theory and introduces frequency components of second and higher order harmonics in the current response. The second difficulty can be solved in conventional impedance measurements by the use of tuned amplifiers and signal correlation techniques. But since more than one frequency is studied in measurements with random noise, the coincidence of higher order harmonics with frequencies originally present in the noise signal will reduce the accuracy of the Fourier transformed data. This may be avoided by the use of prime numbered harmonics for the generation of the noise signals, limiting the choice of harmonics in this work to be 29 primes in the range 3-113. Since the signal amplitude was also kept below 5 mV, the choice of primes was only a precautionary measure. The superimposition of over 20 frequency components of amplitude 5 mV can give rise to peak-to-peak voltages over 100 mV in the composite wave form and depending on the impedance of the test system and the sense resistor it may produce current signals beyond the input limit of the ADC. It may even be the case with the voltage sensing ADC under higher amplification. By the careful choice of sense resistor and ADC gains it is possible to overcome these difficulties. In this work, purely for technical convenience, a sense resistor of 10 Ohm and fixed ADC gains of 10 were used limiting the number of 5 mV frequency components to be used in the noise signal to about 20. Hence most measurements reported in this work were carried out using a noise signal made out of 15 prime numbered harmonics evenly spread in the range 3-113. All these limits depend on the number of data points chosen for the arrays and on the choice of hardware and they may be extended to suit any particular application.

6.4.3 Computer Software

The main programme for the control of random noise experiments was written in MICROSOFT FORTRAN 80(F80) and the modules for the execution of the FFT and the data acquisition were written in Z80 ASSEMBLER with calls to mathematical routines of the F80 library FORLIB. The programme offered the options to

(a) generate the number sequence corresponding any random noise signal,

(b) read noise data from disc, and

(c) measure impedance.

It also had the facility to perform the FFT of data at intermediate stages and their graphical display. For reasons described earlier in theory the lengths of data arrays were restricted to 512.

For the generation of the random noise number sequence any number of harmonics in the range 1-256 with a choice of prime, even, odd or mixed numbered harmonics was available. The values of random phase angles were obtained from an arbitrary position of an array containing 256 random numbers in the range 1-360, which enabled the generation of different noise signals for successive experiments. It also had the facility to save the noise data on disc for subsequent use. The disc access time was reduced by the saving of only half the data array as integer numbers and during the read operation the remaining half was filled with the reflection about the abscissa of the first half. Since this was possible only with odd numbered harmonics, noise signals containing even numbered harmonics could not be saved and had to be generated prior to the measurements. Prior to the disc write, the real data were converted to integers by the multiplication of a suitable scale factor such that the highest number in the sequence contained at least 4 significant figures. The relevant details of the noise signal, viz. scale factor, harmonic numbers, etc. used for the generation of the data were also written into the disc file to be recorded by the programme during a subsequent disc read operation.

The impedance run option could be selected only after the generation or disc reading of the noise data. The programme operated through a menu for the control of experimental parameters such as the signal amplitude, ADC gains, sense resistance of the potentiostat and the number of data acquisition cycles to be executed. The menu also controlled the period of the data acquisition cycle via a parameter

defining the time delay of the data acquisition and displayed the minimum and maxium frequencies that could be covered with the currently generated noise signal in conjunction with the selected time delay. This allowed the convenient selection of the delay to suit a particular experiment and an indication of the setting of the low pass filter. The impedance measurements could be carried out as an 'auto run' where the data acquisition was automatically followed by the FFT of the signals and the impedance calcuation or as 'stepwise run' where the data could be graphically examined after each of the above stages. Prior to the data acquisition the random noise data sequence was scaled according to the required signal amplitude and converted to 12 bit integers for the direct loading in to the registers of the DAC. During the data acquisition these integers were used for the generation of the voltage signal (DAC) which was applied across the cell. Next the programme entered the time delay loop of required length and issued the start conversion command for one of the ADC's which activated the simultaneous reading of cell voltage and current response. The resulting 12 bit ADC data were stored in memory as signed integer numbers and the data acquisition was continued for 512 points. If more than one data acquisition cycle was entered, the programme repeated the procedure while performing a memory addition on the cell response data. Since the maximum ADC input was 4097 and the maximum permissible 16 bit integer was 32767, the maximum number of data acquisition cycles that could be entered was limited to 8 and the acquisition could be terminated at the end of any completed cycle by the press of a key on the console. At the end of the data acquisition the cell response data were transfered to the real elements of two complex arrays of length 512 and performed the FFT operation on the current and voltage data in the time domain. The computational time for each 512 point FFT was about 8 seconds. The cell impedance at the harmonics used for the generation of the noise data was calculated by the complex division of the corresponding frequency domain cell voltage data by current data and displayed in the form of a Sluyter's plot. The actual frequencies associated with the harmonics were calculated from the frequency of the fundamental (inverse of the data acquisition period). The time taken for the acquisition of a single cell response in the absence of additional time delay was 142 µs making the minimum data acquisition period containing 512 points to be 73 ms and hence the fastest possible fundamental frequency to be 13.7 Hz. Thus by the use of the 128th

harmonic, the highest frequency achieved in this work was 1754 Hz.
By the use of maximum time delay possible under the present software,
the lowest frequency achieved was 5 mHz. It should be noted
however, that the range of the frequencies covered in a particular
experiment was always limited to about two decades of frequencies.

6.5 Results and Discussion

Fig. 6.2 is a graphical representation of a random noise signal
made out of 15 prime numbered (3,5,7,11,13,19,23,31,41,53,67,79,89,
101 and 113) harmonics, each associated with an amplitude of 1000 mV
and random phase. Fig. 6.3 is its FFT up to the 120th harmonic
showing 15 peaks of equal heights at the respective harmonics. This
signal was scaled down to 10 mV and the time delay was chosen such
that the sampling period was 0.103 s and the frequency range was 29-
1092 Hz corresponding to the 3rd and 113th harmonic respectively.
The low pass filter was set at 1400 Hz and impedance measurements
were carried out on a Li/SO$_2$ cell (Vidor G 52/12). The impedance
spectrum of this in the range 2kHz-5mHz measured with a Solartron
1250 FRA is shown in Fig. 6.4. The voltage and current across the
cell as measured with the ADC's in response to the random noise
signal are shown in Fig. 6.5 and 6.6 respectively. Even though the
voltage across the cell should be identical to the computer
generated noise signal the two wave forms in Fig. 6.2 and 6.5
differ in minute detail from one another. This is due to the signal
modification, especially in phase caused by the electronic circuitry
and it is incorrect to assume that the two are the same. This fact
is clearly seen in the FFT of the cell voltage Fig. 6.7, which still
shows the 15 peaks at the expected harmonics as in Fig. 6.3, but with
unequal moduli. The gradual decline of the heights at higher harmonics
is mainly due to the finite frequency cut-off of the low pass filter
and the random variation of peak heights at the lower end which may be
due to the signal modification in the potentiostat. This was the
actual voltage signal across the cell and the recorded current signal
would be the actual cell response for the applied noise signal.
Since the impedance was calculated from the division of the actual
cell voltage by the current, the above mentioned instrumental artefacts
did not have any effect on the final result. However, if the cell
voltage was assumed to be the same as the original number sequence
used for the generation of the noise voltage, it is necessary to
calibrate the impedance data using reference cells [47].
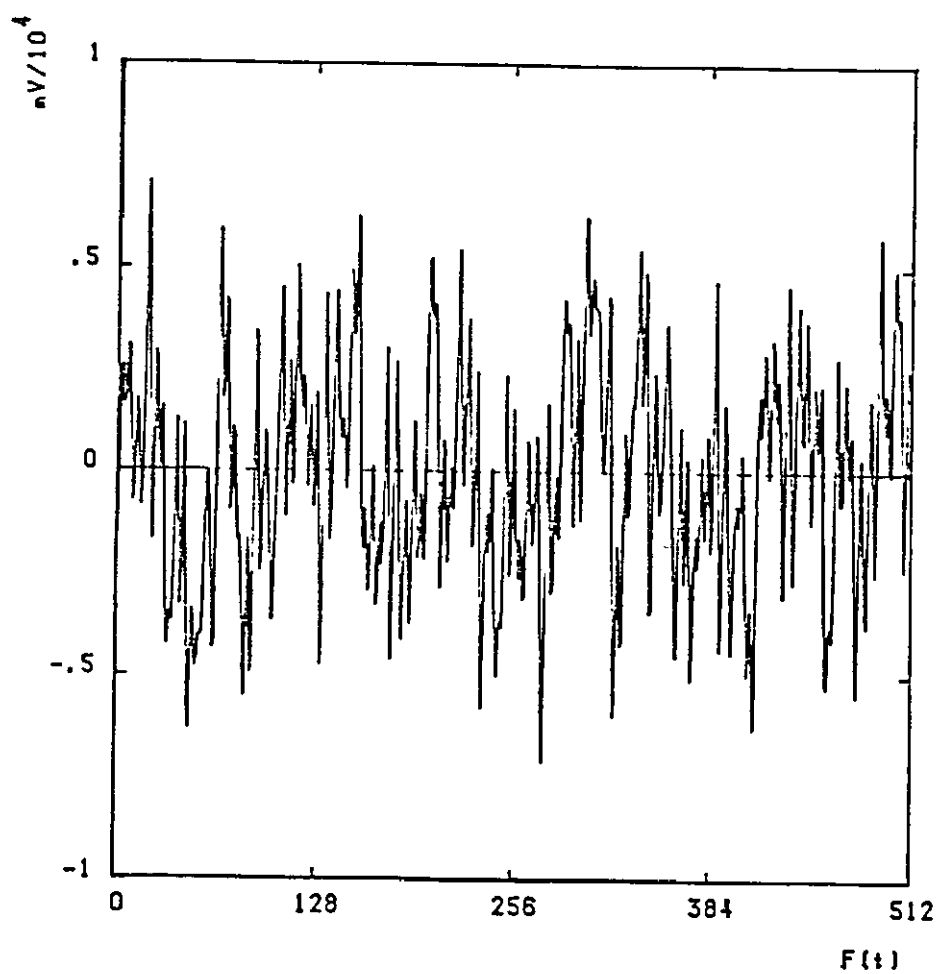
Figure 6.2   Noise signal containing 15 prime numbered harmonics
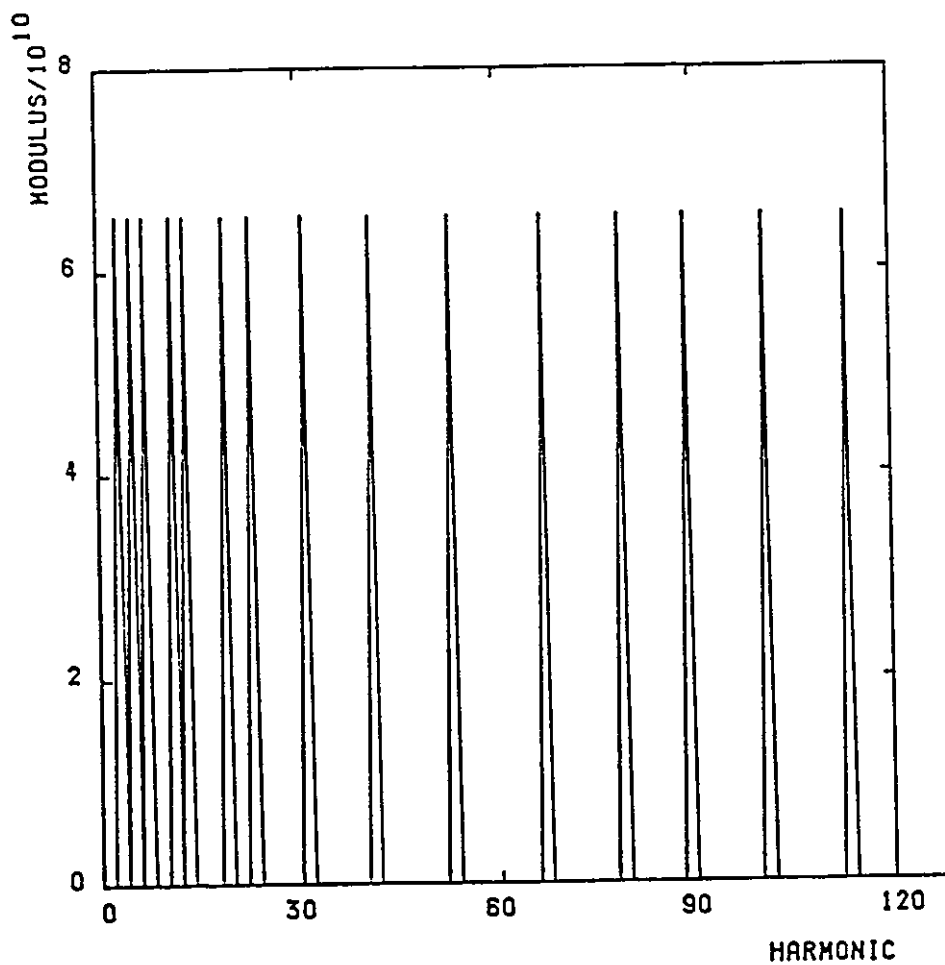   between 3 and 113.
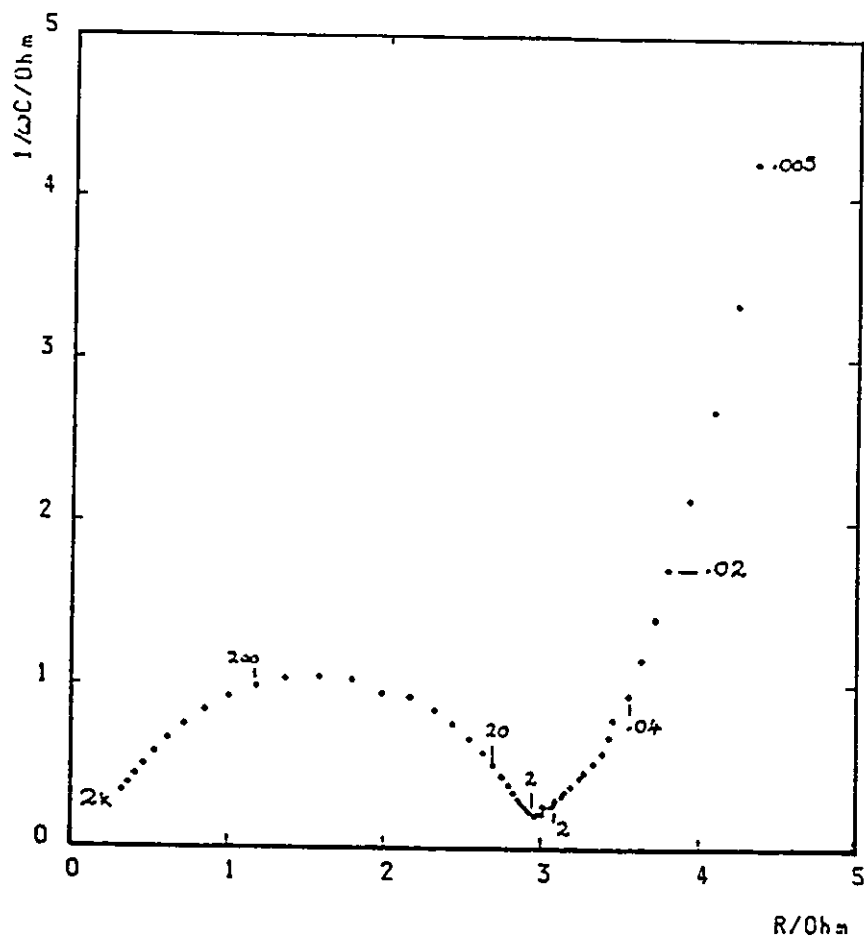
Figure 6.3   FFT of the signal in Fig. 6.2.

Figure 6.4   Impedance spectrum of the Li/SO$_2$ cell as measured with the FRA.
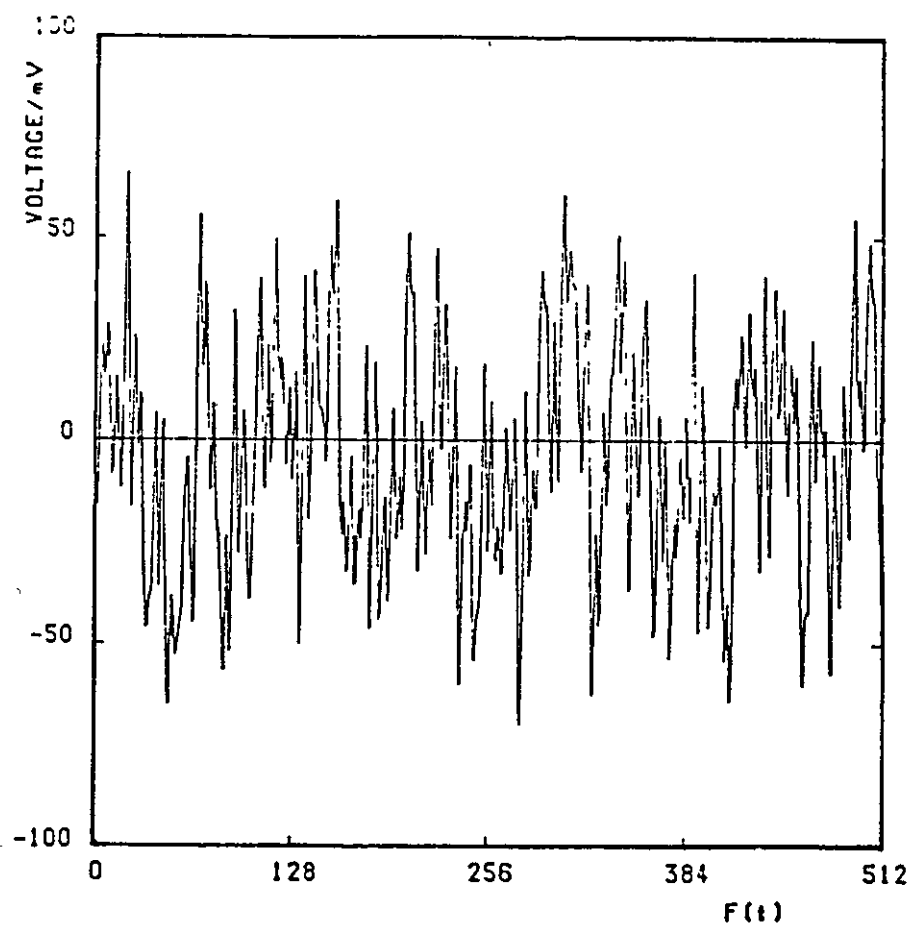
Figure 6.5   Cell voltage response corresponding to the noise signal
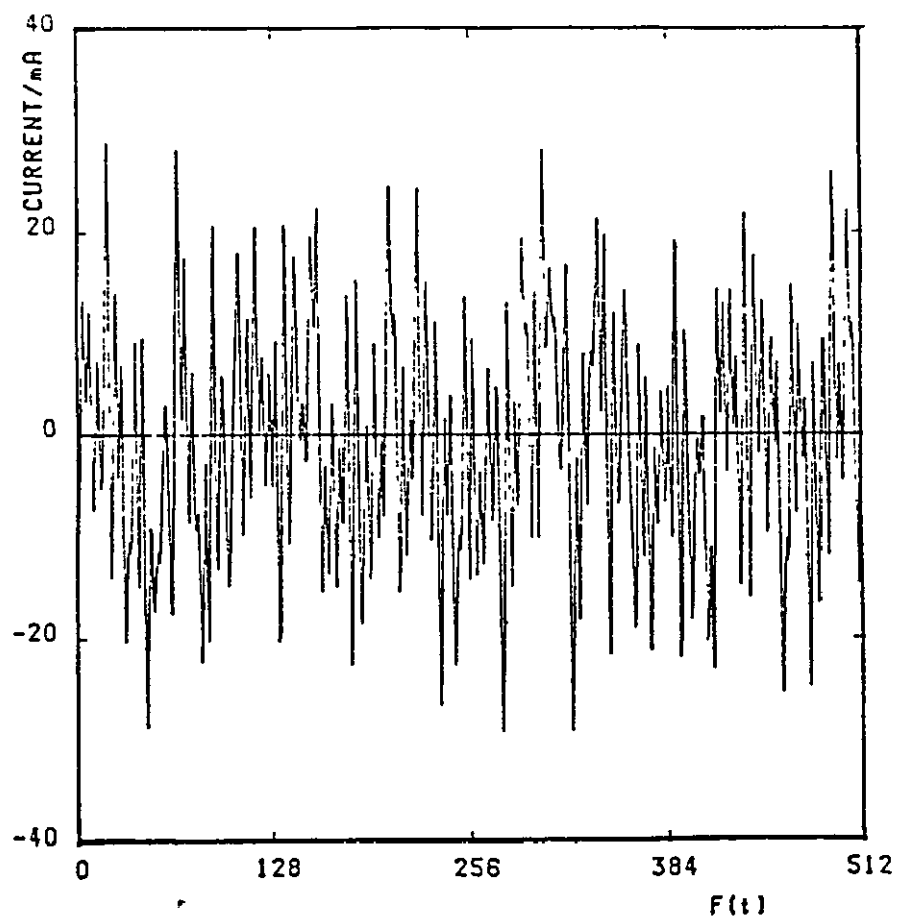in fig. 6.2;   signal amplitude 10 mV;   time period 0.103s.

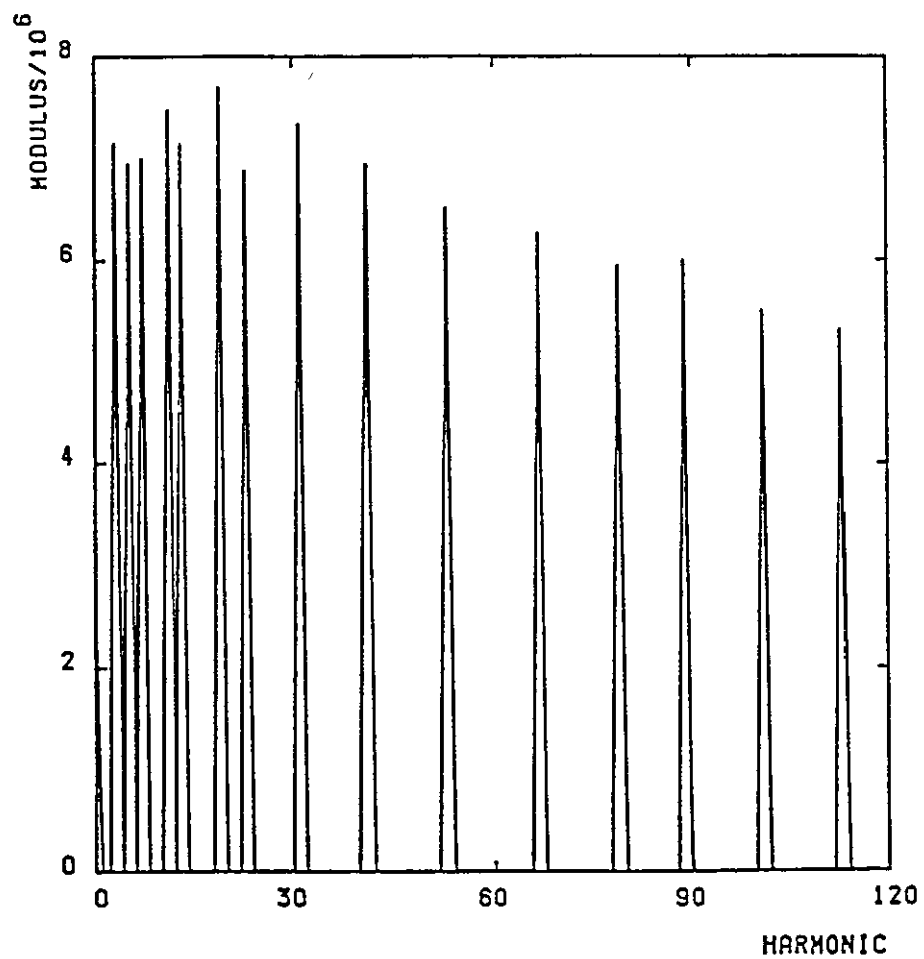Figure 6.6   Cell current response corresponding to Fig. 6.5.

Figure 6.7   FFT of the cell voltage up to the 120th harmonic.

The cell current response Fig, 6,6, differed significantly from the applied noise voltage and the FFT of the current in Fig, 6.8 shows the 15 frequency components at the expected harmonics. As the cell impedance increases at lower frequencies the cell current should be lower and this is demonstrated by the decline of peak heights at the lower harmonics in the FFT. The relatively small peak at the zeroth harmonic present in both FFTs correspond to the d.c. levels of the voltage and current outputs of the potentiostat and do not interfere with the true a.c. characteristics of the cell. Even though the two FFTs only show peaks at the expected 15 harmonics, it should be noted that the magnitudes of the moduli at other harmonics were non zero; however, these were negligible compared with the main peaks. Impedance data calculated at these harmonics were not totally errorneous, but scattered around the expected values. It may be possible to increase the accuracy of these data by averaging over a large number of data acquisition cycles. However, the impedance calculations in this work were only confined to the harmonics originally present in the noise signal.

Fig. 6.9 shows the cell impedance spectrum calculated from the FFTs of the cell response over a single data acquisition cycle at the 15 harmonics. The data acquisition time was 0.103s and the resulting impedance data agree well with the data obtained with the FRA (Fig. 6.4). Since the cell response contains a larger number of cycles at high frequency compared to the 3 cycles at the lowest harmonic, the accuracy of the high frequency data should be better than that of the lower. Fig. 6.10 is the impedance obtained with the same noise signal over 8 cycles of data acquisition showing a marginal increase in the accuracy, especially at high frequencies. When the signal amplitude was lowered to 5 mV, the accuracy of the impedance data obtained (Fig. 6.11) with one data acquisition cycle was comparable with 8 cycles of the 10 mV noise showing the importance of the region of Faradaic linearity. Fig. 6.12 shows the errors associated with the cell impedance spectrum in the range 8-300 Hz obtained without the low pass filter in the output signal of the computer, Any sinusoidal voltage signal digitally generated by a DAC contains discrete voltage steps which can by interpreted as the sum of the actual sine wave and a high frequency saw tooth wave form corresponding to the Nth harmonic where N is the number of points defining the signal. This does not manifest itself in the voltage response of the cell as it is in phase with the sampling and is zero
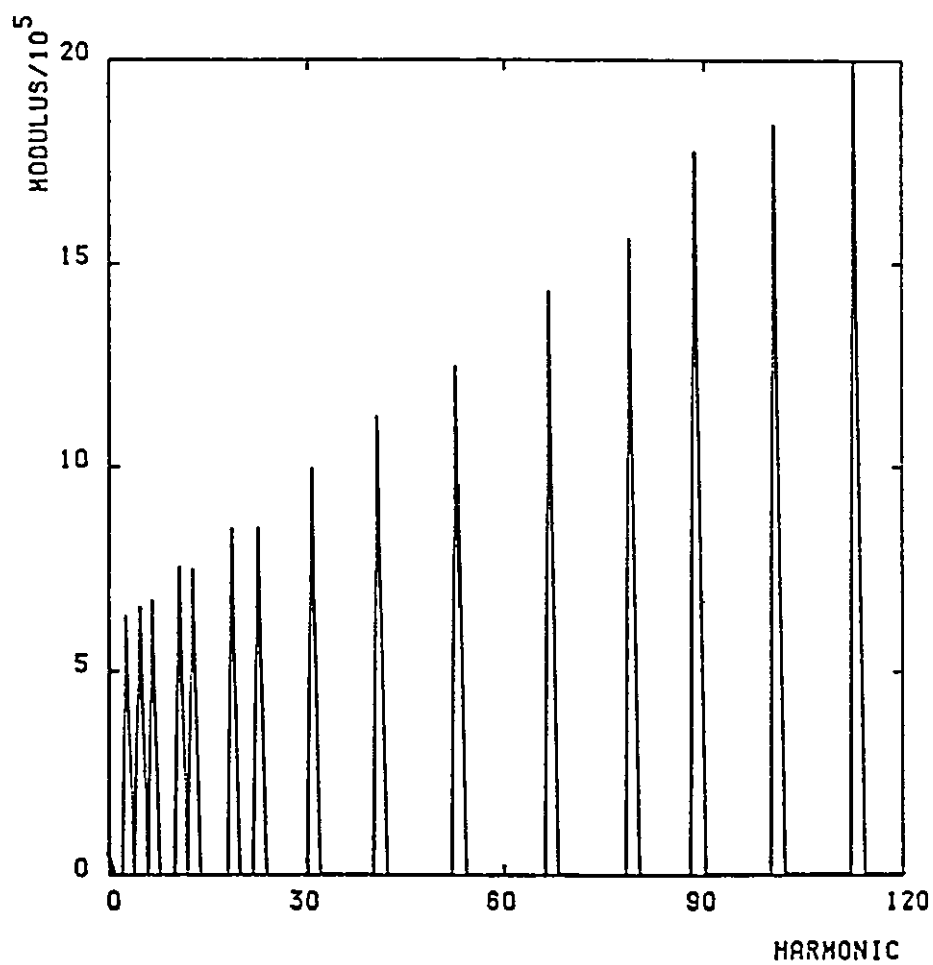
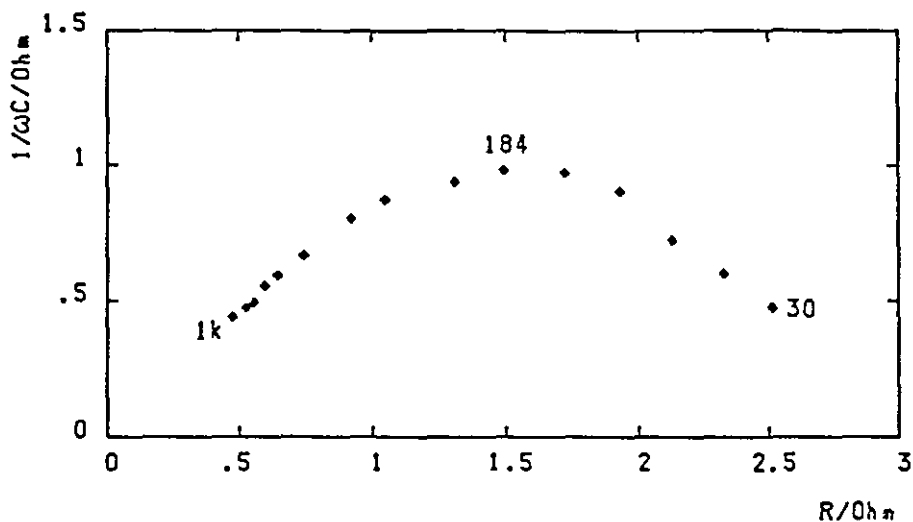Figure 6.8   FFT of the cell current corresponding to Fig. 6.7.

Figure 6 9   Impedance data obtained with 1 data acquisition cycle of the cell responses in Fig. 6.5 and 6.6.
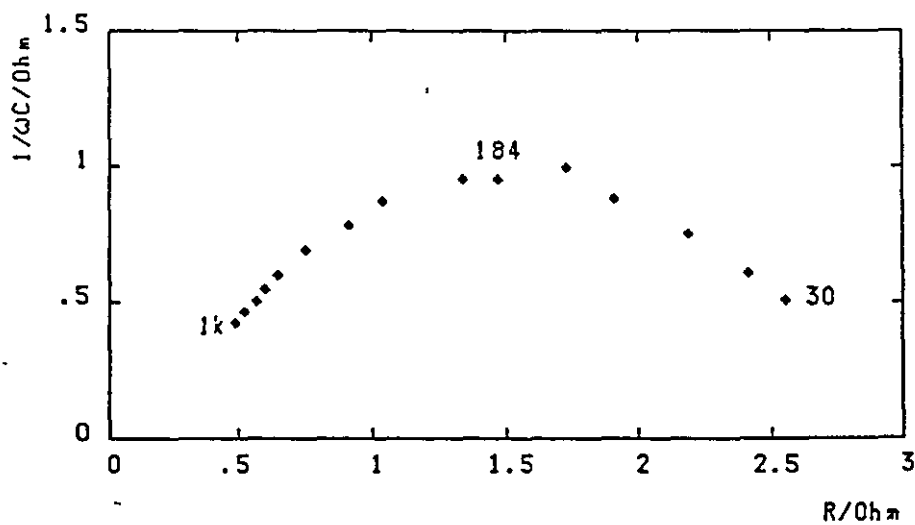

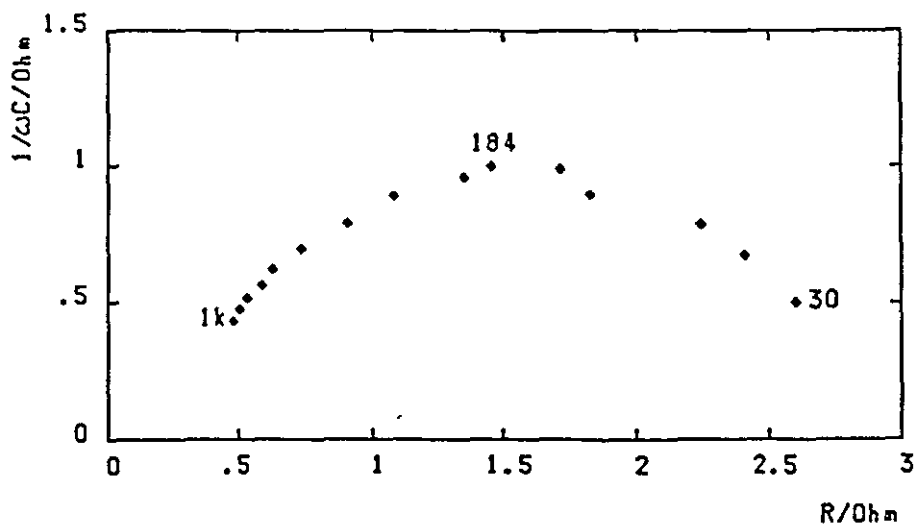Figure 6.10   As in Fig. 6.9; 8 data acquisition cycles.

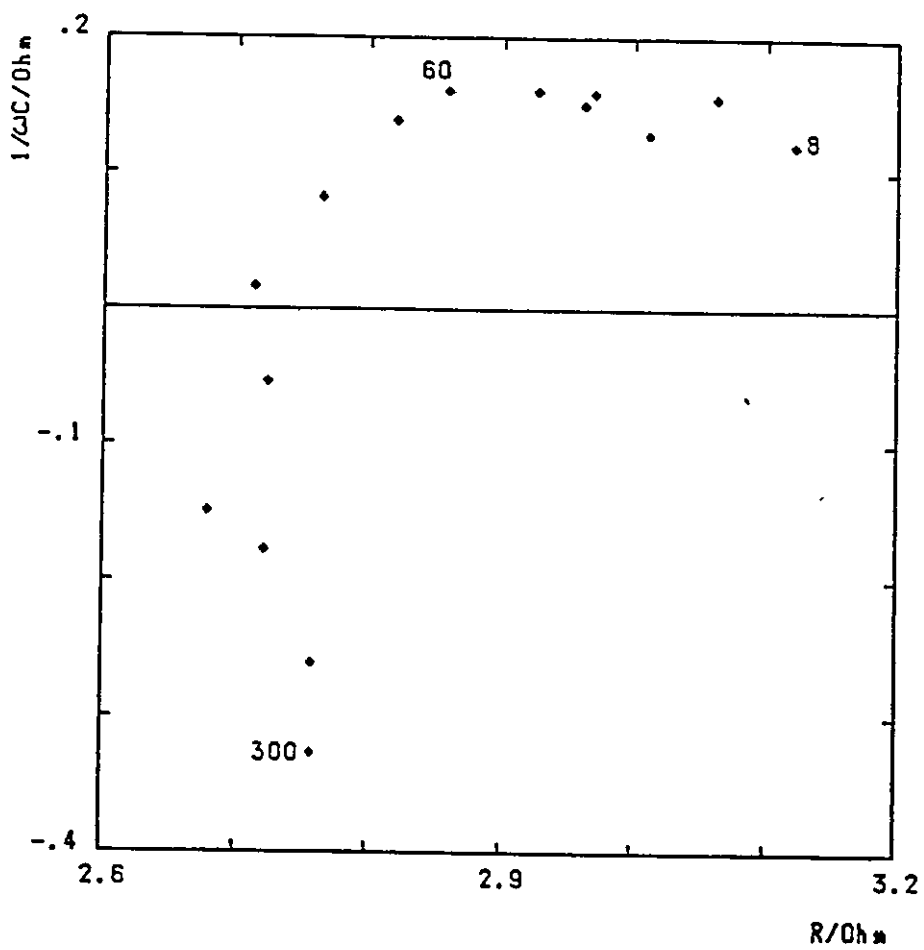Figure 6.11 As in Fig. 6.9; signal amplitude of 5 mV.

Figure 6.12   Impedance data obtained without the use of low pass
              filter.

on every reading. However, due to the complex impedance of the cell
the current response contains contributions from this saw tooth wave
form leading to erroneous impedance data. Thus the actual frequencies
associated with the data in Fig. 6.12 do not correspond to the
frequencies calculated according to the sampling rate and the impedance
data contain contributions from the actual theoretical frequency and
an undefined higher frequency. Fig. 6.13 shows the impedance data
obtained over the lowest possible frequency range with the same noise
signal. The data acquisition was carried out with the maximum time
delay over a single cycle of period 201 seconds and in spite of the
scatter, the data agree in general with that of the FRA. The main
cause for this scatter was the electronic noise introduced into the
signals at the amplification stages prior to the ADC and the error
with the increase of amplifier gain. When working with low signal
voltages it was essential to use certain levels of signal amplification
to improve the resolution of the data and due to the poor signal-to-
noise ratios associated with the amplifiers even the gain of 10 used
in this work seems excessive. These errors may be rectified by the
use of better amplifiers or ADCs of higher resolution.

When dealing with low impedance cells as the high ampere hour
storage cells more care has to be taken with the signal strengths.
As high currents are involved during the perturbation of the cell, the
voltage signals are necessarily limited by the maximum current output
of the potentiostat. In the case of the Solartron 1186 interface this
limit was 0.5 Amps and as a result the composite noise signal was
restricted to a value well below 5 mV during the impedance measurements
of 25 Ampere hours sealed lead acid cells of average impedance about
20 mOhm. This was also a problem during the impedance measurements
with the FRA and special calibration techniques [5] had to be adopted.
When dealing with low level noise signals the problem is further
amplified as it makes the amplitudes of individual frequency components
less than 0.5 mV resulting in poor signal resolution. The impedance
data obtained for the 25 Ampere hour cell reflected the inadequacies
of the hardware and it was not possible to get meaningful data above
7 Hz. Even though the low frequency data generally agreed with data
obtained from the FRA, they contained gross errors due to poor signal-
to-noise levels. Hence for the measurement of low impedances it is
essential to use a potentiostat with a high current capability and
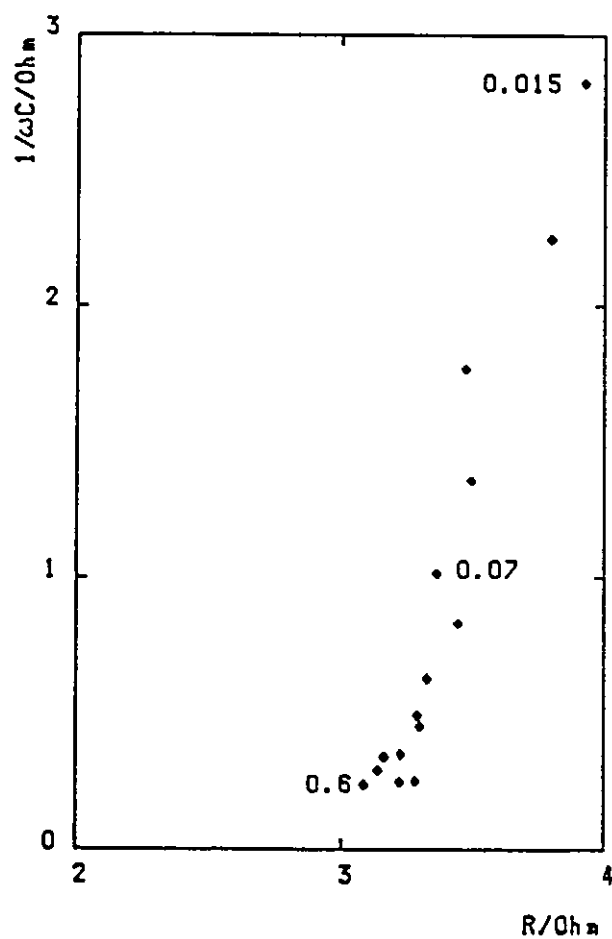DACs of higher resolution.

Figure 6.13 As in Fig. 6.9; time period 201 s; frequencies in the range 15-600mHz.

6.6 Conclusions

- 53 -

(1) The pseudo-random noise technique has been applied successfully for the rapid estimation of impedance. Spectral measurements in the range 5 mHz-2 kHz have been obtained within the period of the lowest test frequency in a 2-decade observation slot (window).

(2) The technique is based on a micro-processor and is ideal for measurements on cells under conditions when space and time are limited; for example in-situ operational battery residual capacity estimations.

(3) Work is continuing on the generation of a dedicated unit capable of avoiding the limitations of the present work.

CHAPTER VII

THE ANODIC PASSIVATION OF THE LITHIUM ELECTRODE

7.1 Introduction

The optimum performance of a cell from a weight and volume basis would be achieved when the lithium and SO_2 are completely utilized at the end of the discharge and at the same time the pores of the carbon matrix become completely blocked with solid discharge product.
Safety considerations also dictate that excess lithium or SO_2 remaining at the end of discharge is undesirable [56-61].

One of the main factors which prevent this ideal state of affairs is the onset of passivity.

This is due to the anodic dissolution of lithium which establishes a concentration gradient in the solution with the highest lithium ion concentration at the electrode surface. With the continued passage of current the concentration increases until a solubility limit is reached at the anode surface, causing a layer of a lithium salt to be laid down, which effectively screens the metal surface from further attack.

Passivity of this type was first investigated systematically by Müller [62] who referred to it as "Bedeckungs Passivität" or "cover passivity" to distinguish it from chemical passivity.

Unlike chemical passivity the deposited layer may dissolve in time as the concentrations of species at the surface return to their bulk values in the cell by diffusion or convection, perhaps allowing further discharge of the cell.

Until relatively recently it was generally assumed that lithium could not be passivated by anodic polarization. However, James [63] reported this phenomenon for lithium in propylene carbonate and $SOCl_2$ electrolyte solutions at room temperature. He later concluded [64] that this was due to the accumulation of anodic dissolution products in the pores of a surface layer formed on the metal during storage at open circuit.

Zlatilava et al [65] have also reported this phenomenon for Li in acetonitrile + 30% SO_2 solutions for LiBr for the temperature range (-10 to -30°C).

"Cover Passivity" has been extensively studied for other metals, for example zinc in alkaline solutions [66-71], Ni [72], Fe and Cr [72] in acid solutions and Pb in aqueous sulphuric acid [74-76].

In this chapter it will be shown that lithium can exhibit this passivation phenomenon in LiBr/Acetonitrile/SO_2 solutions at room temperature at high current densities and is therefore an important factor in the efficiency and safety of high rate Li/SO_2 cells.

The effect of interruptions in the polarisation, which may be important for some applications of these cells is also examined.

7.2 Theoretical Principles

The problem of concentration changes at an electrode subject to semi-linear diffusion was discussed by Sand [77] who showed that if diffusion is the only mode of mass transport, then the time, t_p, for a limiting concentration to occur at the electrode for current, i, is given by an equation of the form:

$$i \sqrt{t_p} = \frac{nFC_p}{2} \sqrt{\pi D} \tag{7.1}$$

where

n is the number of electrons involved in the process,

F is the Faraday constant,

D is the diffusion coefficient,

C_p is the concentration of the passivating species at the electrode surface at passivation minus the initial concentration.

For the case of interrupted polarisation, an equation of the form

$$i_2 \sqrt{t_3} + i_1 (\sqrt{t_1+t_2+t_3} - \sqrt{t_1+t_2}) = nF \ C_p \sqrt{\pi D}/2 \tag{7.2}$$

can be derived [74-75]. Where an initial current i_1 amps flows for t_1 seconds, is discontinued for t_2 seconds and then another i_2 is passed until passivation for t_3 seconds.

7.3 Experimental Procedure

The derivations of the above equations make the assumption that diffusion is restricted to one dimension and such effects such as convection are negligible.

To ensure these assumptions were as reasonable as possible a simple cell was designed and is shown in Fig. 7.1.

A is the counter electrode, in this case a roll of the commercially manufactured carbon cathode material.

B is a tube to allow the cell to be topped up with electrolyte.

C is the reference electrode, in this case either lithium or silver wire in a polypropylene sleeve.

D is the glass cell body.

E is the electrolyte solution, which was various concentrations of $LiBr/AN/SO_2$.

F is a plastic screw cap which was tightened and together with the rubber O-rings, H, effected a liquid tight seal.

G is the anode, cut from lithium foil.

I is a copper disc which provided electrical contact with the external circuit.

By orientating the passivating electrode in a horizontal plane with electrolyte confined in such a way that it formed a vertical right cylinder above the electrode convection can be suppressed as long as the experiment is not too protracted. In addition because the electrolyte is only allowed access to the horizontal surface of the electrode no spurious edge effects can influence the progressive development of the linear concentration gradient in the vertical direction. This general principle of operation has been described in the literature [78,79].

The cells were assembled in an Argon filled 'dry-box', atmosphere <10 p.p.m. water. The lithium electrodes were cut from LITHCO lithium foil, thickness .008". The electrolyte was prepared and dried in the dry-box.

The cells were discharged galvanostatically at various current densities inside the dry-box. The potential of the lithium anode w.r.t. the reference electrode was monitored with time on a chart recorder, Fig. 7.2, shows a typical potential profile.

It can be seen the cell shows the voltage delay, typical of lithium electrode, when the current is switched on [80]. The onset of passivity causes the potential to fall rapidly. The passivation time, t_p, is calculated by drawing tangents to the curve before and after
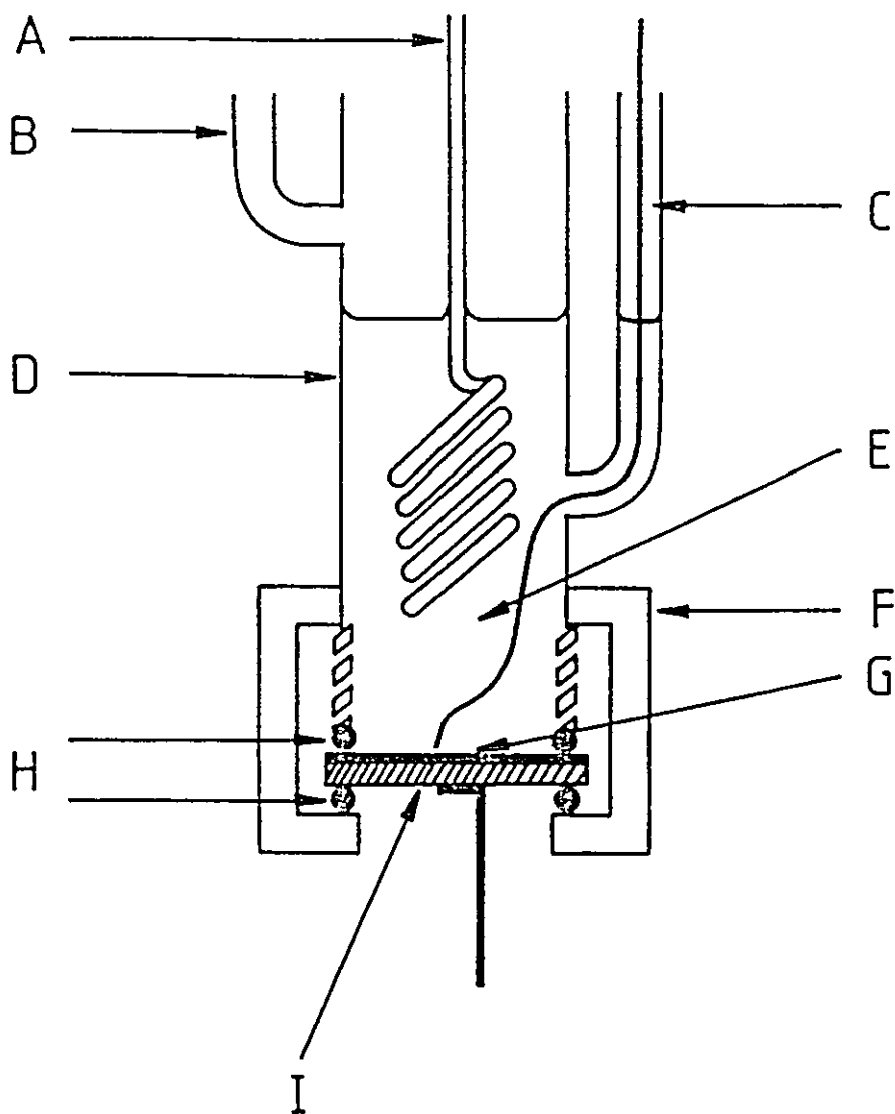
Figure 7.1   Diagram of cell used in passivation experiments.

passivation and finding the intersection, see Fig. 7.2.

7.4 Results

Fig. 7.3 shows plots of $t_p^{-\frac{1}{2}}$ versus i, the current density for various values for the concentration of LiBr. It can be seen that the plots are good straight lines, the slopes of which were determined. From equation (7.1) the slope should equal $2/nFC_p\sqrt{\pi D}$. Table 7.1 gives the values of these slopes.

If C_c is the critical concentration at which passivation occurs and C_o the initial concentration, then

$$C_p = C_c - C_o \qquad\qquad (7.3)$$

so
$$\frac{1}{m} = \frac{nF\sqrt{\pi D}}{2} (C_c - C_o) \qquad\qquad (7.4)$$

where m is the slope for the $t_p^{-\frac{1}{2}}$ versus i plots. Thus a plot of $1/m$ vs C_o should give a straight line of slope $\frac{-nF\sqrt{\pi D}}{2}$ and intercept $\frac{nF\sqrt{\pi D}}{2} C_c$

this plot is shown in Fig. 7.4 and from this the slope is -715.6 ($mAcm^{-2}s^{\frac{1}{2}}mol^{-1}$litre) and intercept is 1.649 x 10^3($mAcm^{-2}s^{\frac{1}{2}}$), with correlation coefficient, -0.973.

So C_c = 2.30 M

and D = 7.00 x 10^{-5} cm^2 s^{-1}

as n = 1 for the reaction $Li = Li^+ + e^-$ and F = 9.64867 x 10^4 C mol^{-1}.

TABLE 7.1

| concentration LiBr, C_o, (M)	slope, $m(s^{-\frac{1}{2}}mA^{-1}cm^2)$	correlation coefficient
1.67	1.937 x 10^{-3}	0.9888
0.843	1.131 x 10^{-3}	0.9933
0.444	7.241 x 10^{-4}	0.9812
0.219	6.480 x 10^{-4}	0.9975
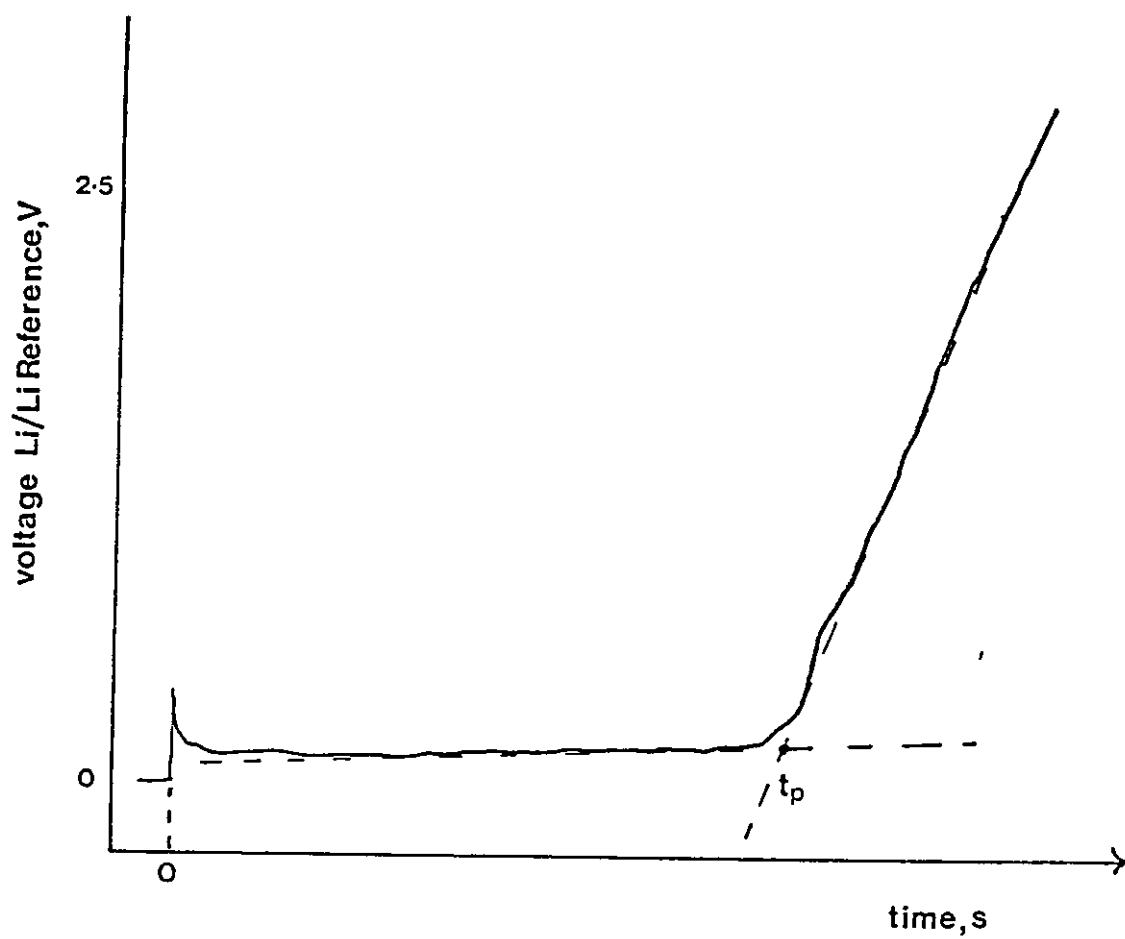
Figure 7.2   A typical potential-time plot for the passivation of
a lithium anode.

Fig. 7.3 Plots of $t_p^{-1/2}$ vs. current density,i, for different initial LiBr concentrations,C_0

Current density,i,mAcm^{-2}

$t_p^{-1/2}$,$S^{-1/2}$
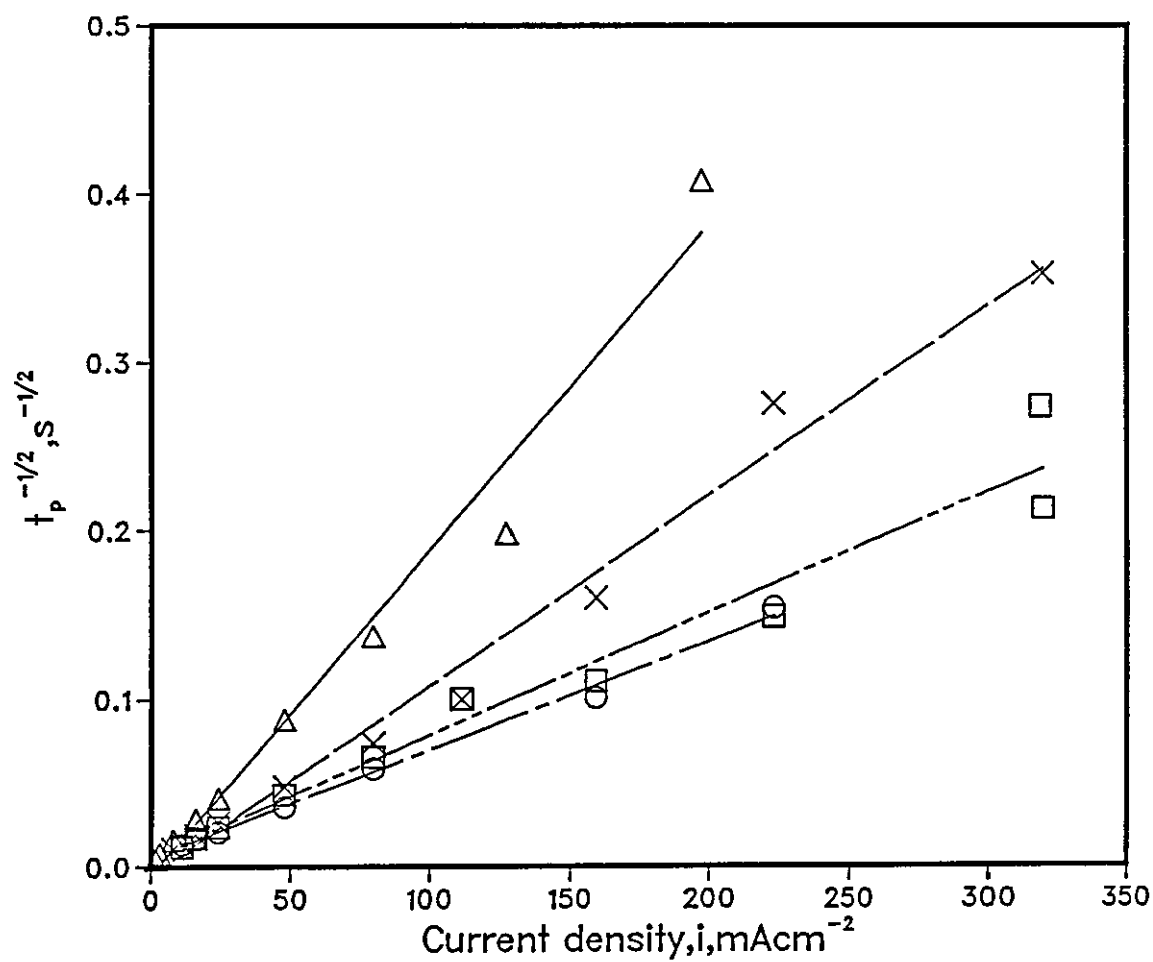
△   1.67M LiBr, 4.02M SO$_2$

✕   0.843M LiBr, 4.05M SO$_2$

☐   0.444M LiBr, 4.05M SO$_2$

○   0.219M LiBr, 4.05M SO$_2$

Fig. 7.4 Plot of reciprocal of slopes from fig. 7.3,1/m vs. the initial concentration of LiBr,C_o
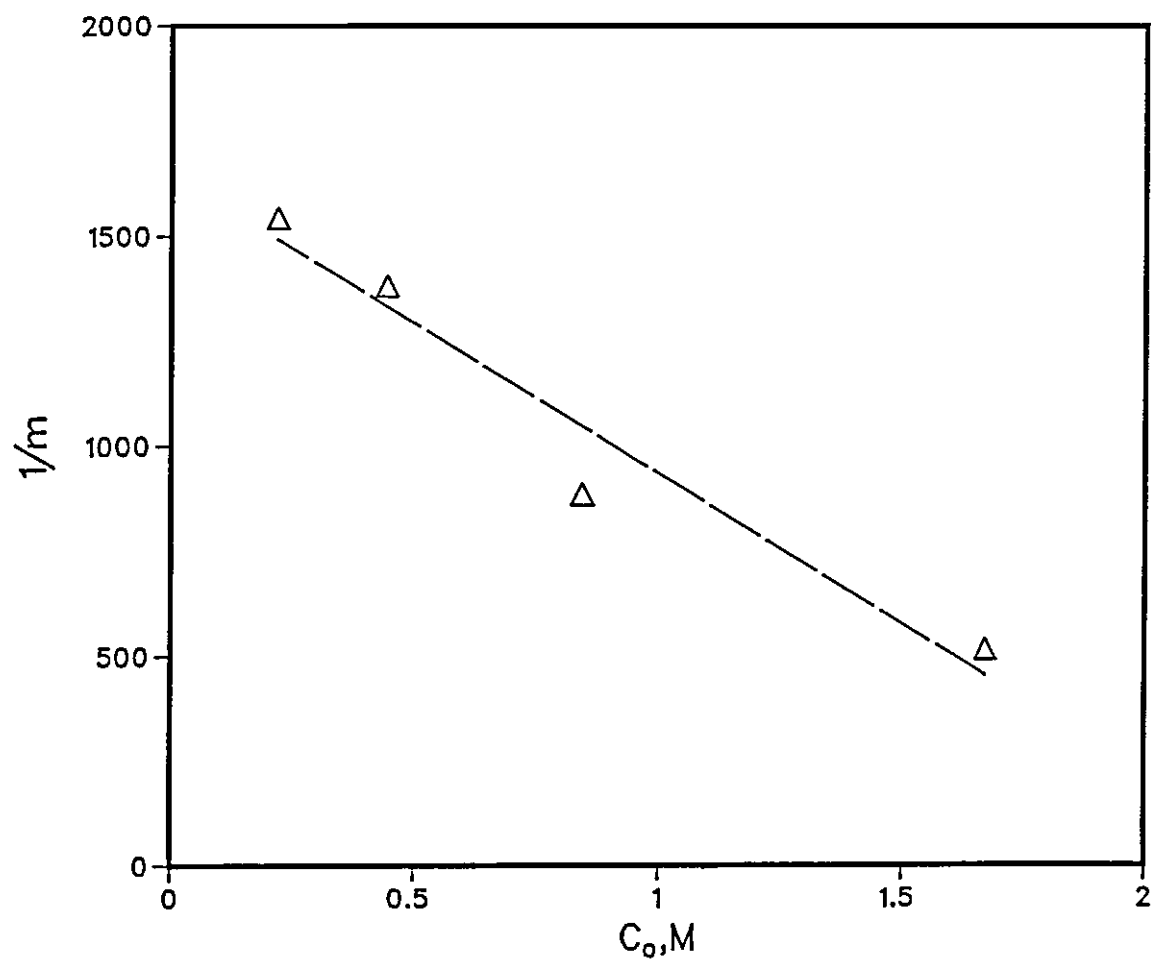
These values seem to be of the right order of magnitude and compares with C_c = 3.8 M and D = 5 x 10^{-6} cm^2s^{-1} at -30°C calculated by Zlatilova et al [65].

Figure 7.5 shows a plot of $it_p^{\frac{1}{2}}$ vs i for the same data values as Figure 7.3. If equation 7.1 holds then the plots should be horizontal straight lines, it can be seen that this is a good approximation at high current densities, but breaks down at very low current densities, as might be expected.

Table 7.2 gives data for interrupted runs for 1.67 M LiBr and a value of $nFC_p\sqrt{\pi D}/2$ is calculated for each run according to equation (7.2).

TABLE 7.2

i_1 (mA)	i_2 (mA)	t_1(s)	t_2(s)	t_3(s)	$nFC_p\sqrt{\pi D}/2$ (mAcm^{-2} s$^{\frac{1}{2}}$)
79.58	79.58	30	31	78.9	813.85
79.58	40.62	30	30	313.5	782.2
23.87	49.02	300	120	126.6	551.6
23.81	8.63	4800	660	1678.8	1213.7

The value for $nFC_p\sqrt{\pi D}/2$ calculated from the slope of $t_p^{-\frac{1}{2}}$ vs current density (Table 7.1) for this concentration is $1/_m$ = 516.3 mAcm^{-2}s$^{\frac{1}{2}}$. Thus it can be seen that equation (7.2) holds approximately providing t_1, t_2, t_3 are not too large.

7.5 Conclusions

It has been demonstrated that the lithium electrode in open cells of the type described in this chapter can exhibit anodic passivation at room temperature and that the passivation time and current density are related by Sand's equation provided the current densities are high enough, typically >20 mAcm^{-2}.

The concept of a critical concentration of the metal ion above which passivation occurs has been validated as the plot of $nF\sqrt{\pi D}/2$. C_p vs C_o is a good straight line; the value of this concentration was found to be 2.30 M.

The value of the diffusion coefficient for Li$^+$ in AN/SO$_2$ solutions was also determined and was calculated to be 7.00 x 10^{-5} cm^2s^{-1}.

Fig. 7.5   Plot of $it_p^{1/2}$ vs current density,i for the same data as fig. 7.3
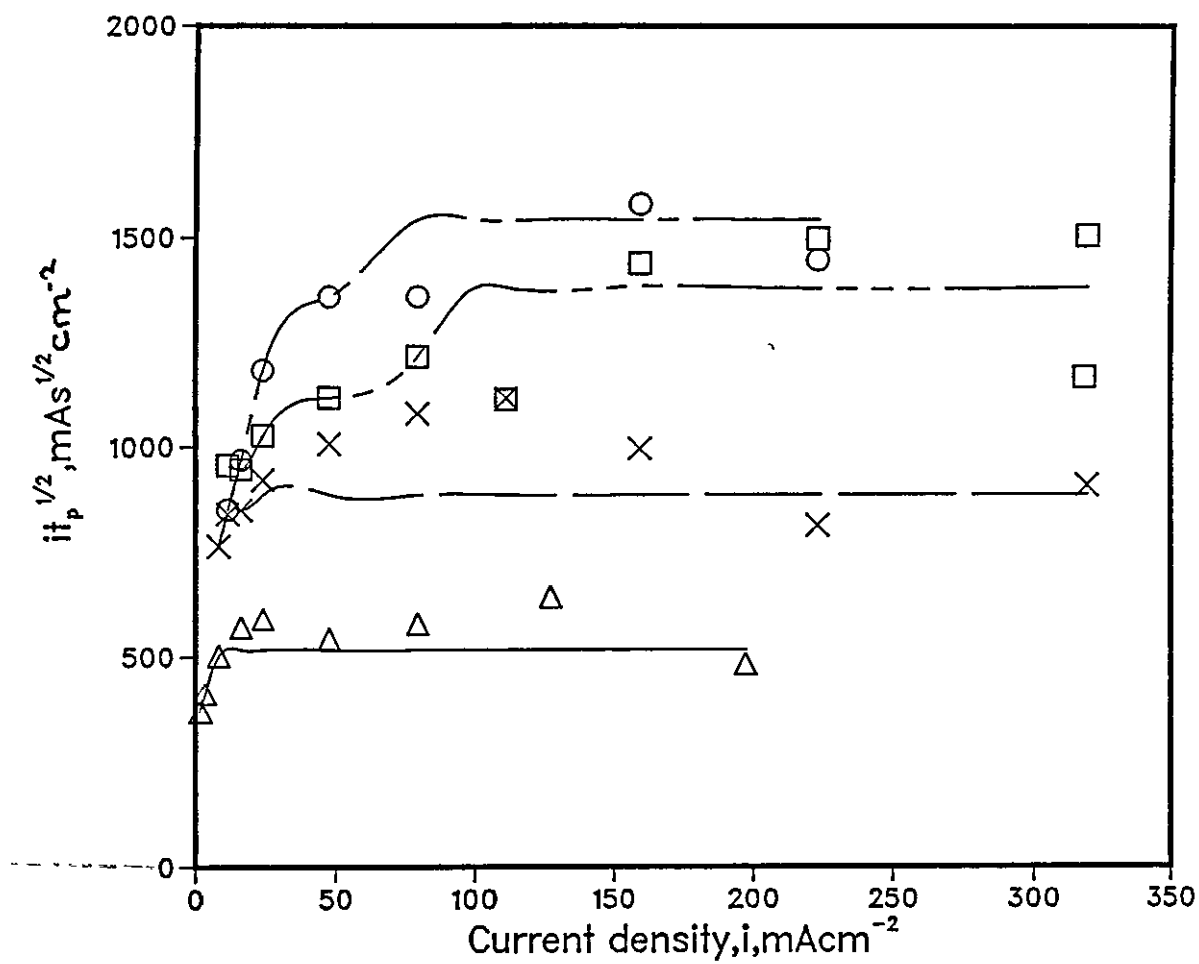
Thus it has been shown that this form of passivation of the lithium anode can be a valid failure mode for Li/SO$_2$ batteries at high current densities at room temperature. The values of the parameters determined in this chapter may be used to calculate the capacity of a cell at a certain discharge rate if the cell is to be discharged to passivation in one go. Also an estimate of the capacity may be made for an interrupted discharge.

CHAPTER VIII

THE PASSIVATION OF THE CARBON CATHODE

8.1 Introduction

In the previous chapter the passivation of the lithium anode was
examined, this may be irrelevant as far as the whole Li/SO$_2$ cell is
concerned if it is the carbon cathode that determines the cell behaviour,
by passivating first.

Therefore the passivation of the carbon cathode under similar
conditions to those for the lithium anode was investigated.

8.2 Experimental Procedure

The set-up of the cell was identical to that for the previous
chapter, see Fig. 7.1, except that G was a disc of carbon cathode
material and the counter electrode, A, was a roll of lithium foil. To
ensure that the lithium did not passivate first, the area of the counter
electrode was many times greater than that of the cathode.

The cathode was cut from a sheet of commercially manufactured
cathode (Crompton Parkinson Ltd.) identical to that used in commercial
Li/SO$_2$ cells. This consisted of acetylene black (specific surface area
76 m^2 g^{-1}) on an aluminium mesh with a PTFE binder.

The cells were constructed and discharged as before and the
passivation times determined.

The concentration of SO$_2$ in the electrolyte was varied, but as the
SO$_2$ is responsible for the solubility of the LiBr in acetonitrile, the
LiBr concentration had to be reduced if the SO$_2$ concentration was
reduced.

To demonstrate that the lower concentration of LiBr would have
no effect on the cathode passivation, runs were performed with the
same SO$_2$ concentration, but different LiBr concentrations; the
passivation times were found to be the same.

8.3 Results and Discussion

Figure 8.1 shows the plots of $t_p^{-\frac{1}{2}}$ vs. i, the current density for various values for the concentration of SO_2. These give good linear plots, the slopes of which were determined and are shown in Table 8.1.

TABLE 8.1

Concentrations (M)		slope, m $(s^{-\frac{1}{2}}mA^{-1}cm^2)$	correlation coefficient
LiBr	SO_2		
1.828	4.68	6.74×10^{-4}	0.9898
0.829	2.01	1.31×10^{-3}	0.9841
0.419	1.02	2.30×10^{-3}	0.9955
0.205	0.499	4.05×10^{-3}	0.981

The fact that these plots do give such good straights shows that the carbon cathode does exhibit a passivation phenomenon similar to that described in the previous chapter.

Figure 8.2 shows plots of $it_p^{\frac{1}{2}}$ vs. i for the same data as Figure 8.1, and demonstrates that the Sand equation is obeyed for current densities $> \sim 20$ $mAcm^{-2}$.

If $1/m$ is plotted vs. C_{SO_2}, the concentration of SO_2 as before, a very good straight line is obtained, (see figure 8.3), the slope of which is 292.1 $mAcm^{-2}s^{\frac{1}{2}}mol^{-1}litre$, intercept 133.2 $mAcm^{-2}s^{\frac{1}{2}}$ and correlation coefficient 0.998.

However, the slope is positive and not negative as obtained in Chapter 7, which means that increasing the SO_2 concentration gives longer passivation times for the cathode, whereas increasing the LiBr gives shorter passivation times for the anode.

This can be explained as follows.
The reaction at the cathode is:

$$2SO_2 + 2e^- \rightleftharpoons S_2O_4^{2-} \tag{1.9}$$

Initially the concentration of the dithionite ion will be zero, but as the discharge proceeds, the concentration will build up until it reaches a critical value, C_c, and passivation will occur.

Fig. 8.1 Plot of $t_p^{-1/2}$ vs. current density, i for different values of the initial SO_2 concentration, C_{SO_2}
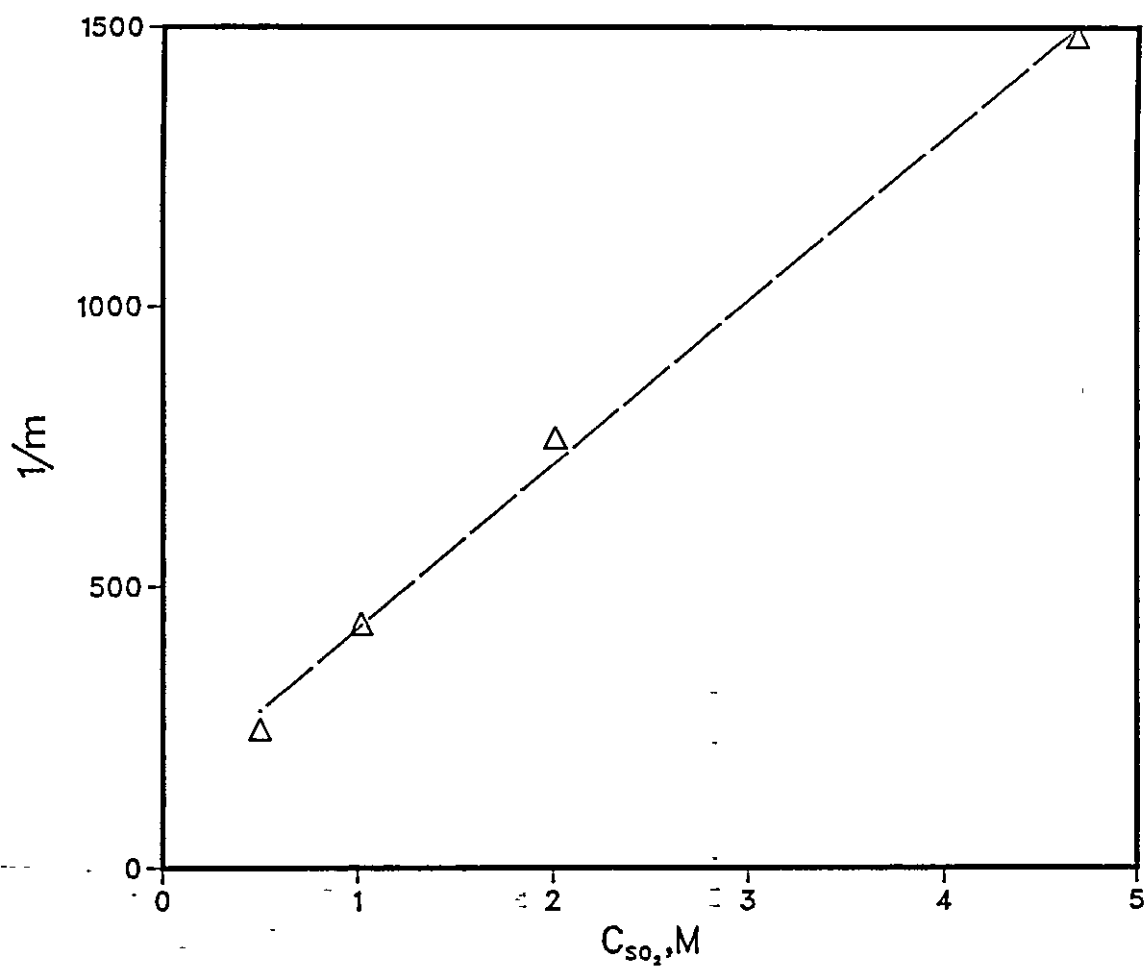
Current density, i, mAcm^{-2}

$t_p^{-1/2}$, $S^{-1/2}$
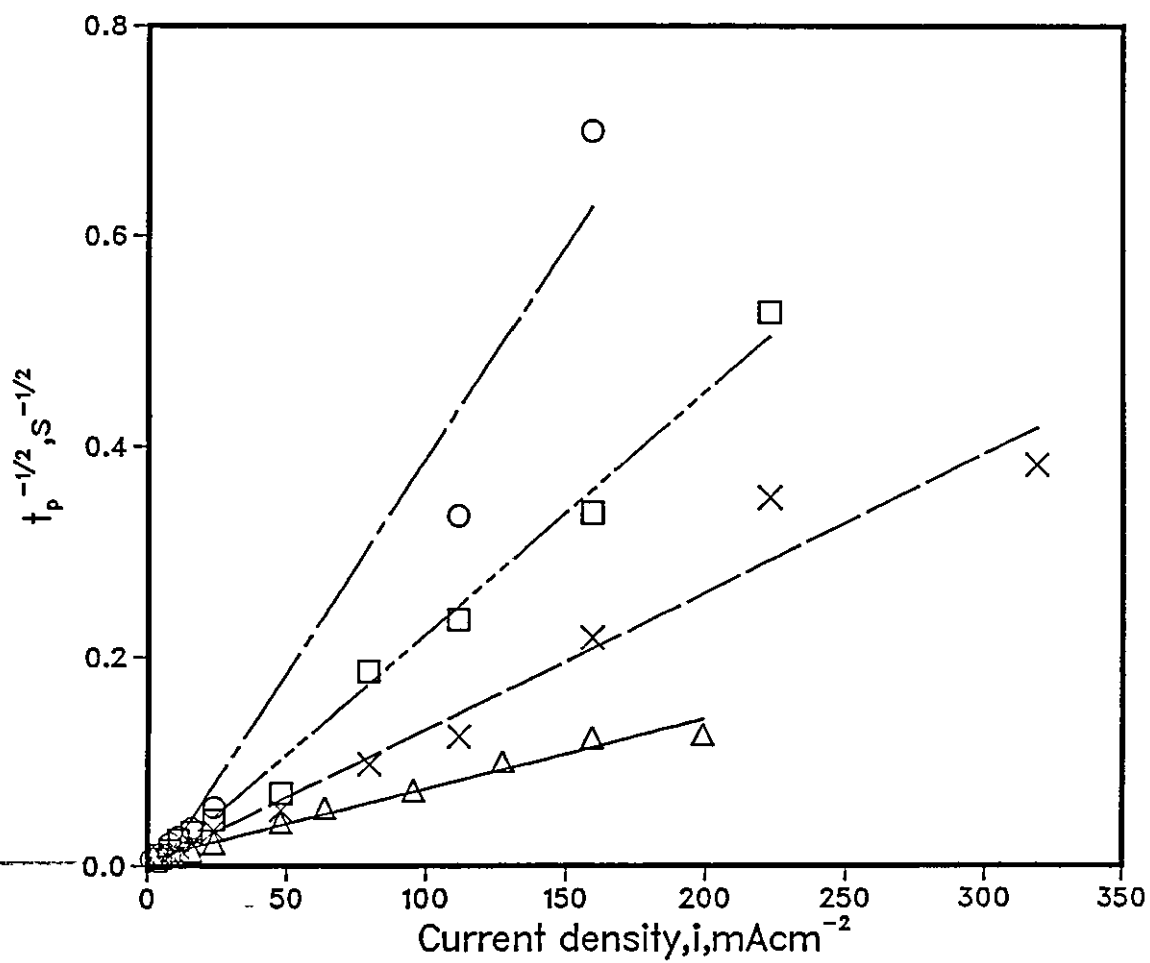
△ 1.828M LiBr, 4.68M SO_2

✕ 0.829M LiBr, 2.01M SO_2

☐ 0.419M LiBr, 1.02M SO_2

○ 0.205M LiBr, 0.499M SO_2

Fig. 8.2 Plot of $it_p^{1/2}$ vs. current density,i for the same data as fig. 8.1
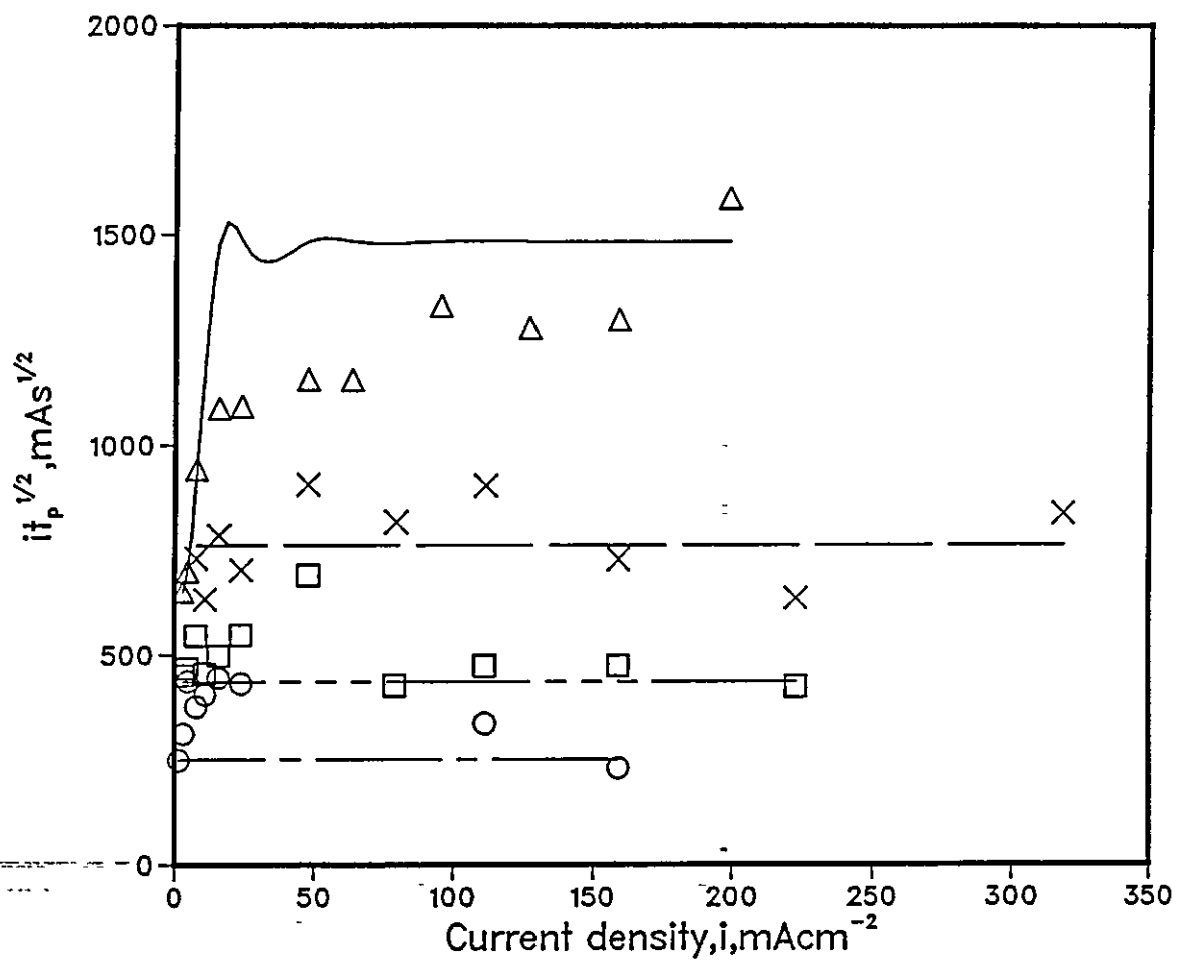
$\triangle$ 1.828M LiBr, 4.68M SO_2

$\times$ 0.829M LiBr, 2.01M SO_2

$\square$ 0.419M LiBr, 1.02M SO_2

$\bigcirc$ 0.205M LiBr, 0.499M SO_2

Fig. 8.3 Plot of reciprocal of slopes from fig. 8.1,1/m vs. the initial SO_2 concentration,C_{so_2}

C_o from equation (7.4) will be zero for each concentration of SO_2 in Table 8.1. C_c must therefore be a function of the SO_2 concentration. The greater the SO_2 concentration, the greater the solubility of $Li_2S_2O_4$ will be and hence C_c will be greater. This seems reasonable as the solubility of LiBr is increased in the presence of SO_2, the yellow colour of the electrolyte suggests the charge transfer absorption of a complex.

The fact that the plot of $1/m$ vs C_{SO_2} is such a good straight line suggests the relationship between C_c and C_{SO_2} will be of the form

$$C_c = kC_{SO_2} + \alpha \tag{8.1}$$

where k and α are constants.

Thus the slope of $1/m$ vs. C_{SO_2} will equal $nF\sqrt{\pi D}/2.k$ and the intercept $nF\sqrt{\pi D}/2\ \alpha$, where D is the diffusion coefficient of the dithionite ion.

Unfortunately no value for D is known, but putting in a rough order of magnitude of 10^{-5} yields the following values for k and α.

$$k = 5.4 \times 10^{-1}$$

$$\alpha = 2.5 \times 10^{-1}\ mol\ l^{-1}$$

showing that dithionite can have significant solubility under these conditions.

The effect of interruption was also investigated and Table 8.2 shows the data obtained, for 1.828 M LiBr, 4.68 M SO_2.

TABLE 8.2

i_1 (mA)	i_2 (mA)	t_1 (s)	t_2 (s)	t_3 (s)	$nFC_p\sqrt{\pi D}/2$ (mAcm^{-2}s$^{\frac{1}{2}}$)
47.75	47.75	300	300	195	0.951×10^3
47.75	47.75	124	1200	378	1.001×10^3
47.75	95.49	120	60	100.5	1.152×10^3
47.75	23.87	450	600	330	0.751×10^3

The value for $nFC_p\sqrt{\pi D}/2$ calculated from the slope of $t_p^{-\frac{1}{2}}$ vs. i (Table 8.1) for this concentration was

$$1/m = 1.48 \times 10^3\ mAcm^{-2}s^{\frac{1}{2}}$$

thus it can be seen that equation (7.2) holds approximately providing t_1, t_2, t_3 are not too large and the current densities are not too low.

It was also observed that if the discharge was continued after passivation lithium was deposit ed on the carbon surface in the form of dendrites. This indicates a possible safety hazard if cells are discharged galvanostatically in this manner after the carbon has passivated, as the dendrites might puncture the separator causing a short circuit. In addition, it has been reported that aluminium can catalyse the reaction between finely divided carbon and lithium [81] and aluminium is present in the backing mesh.

8.4 Conclusions

It has been shown that the carbon cathode does exhibit the passivation phenomenon for high current densities (>20 mAcm^{-2}). As the carbon electrode is in the form of a porous matrix at low current densities the $Li_2S_2O_4$ will be able to diffuse into the pores and only screen of a relatively small area of electrode when it precipitates.

To achieve longer passivation times for lithium, the concentration of LiBr must be reduced, however, this will also cause the conductivity to drop. For carbon the passivation times are increased by increasing the SO_2 concentration.

This suggests for high rate cells as much SO_2 as possible should be added to the electrolyte, this may have the additional benefit of increasing C_c for LiBr in the same way as it does for $Li_2S_2O_4$, thus increasing the passivation times for the lithium anode.

Comparison of the data for both electrodes shows that given the LiBr concentration is about 1.8 M for conductivity purposes, the lithium will always passivate before the carbon, it is therefore the lithium electrode which determines the cell behaviour.

Consequently it would be possible to design a high rate cell for single discharge with much less cathode material, so the cathode area is much less than that of the anode. This may be economically attractive.

CHAPTER IX

THE COMPUTER SIMULATION OF ELECTROCRYSTALLIZATION REACTIONS ON A
PLANE SURFACE

9.1 Introduction

A nucleation and growth mechanism has been applied to metal
deposition from the vapour phase by Kossel [82] and Stranski [83], who
postulated two dimensional nucleation and subsequent layer-by-layer
growth.

Their concepts were later applied by Erdey-Gruz and Volmer [84]
to crystal growth from solution and extended by many others [85].

It was desirable that the collision and overlap of these centres
was to be considered and much progress was made by the Fleischmann school
[85] using the Avrami theory of overlap [86] (similar overlap theories
giving an identical result have been derived by Kolmogorov [87] and
Evans [88]).

Armstrong et al [89] extended this work to the growth of three
dimensional conical crystals as well as three dimensional growth
leading to passivation.

Apart from this and the work of Evans [90] and Müller [91] very
little attention has been paid to the problem of nucleation and growth
followed by passivation.

The first problem in considering any three dimensional growth is
finding a volume transform, that is a relationship between the volume
of overlapped crystals and the volume they would have had had overlap
not taken place.

The Kolmogorov-Avrami-Evans theorem [86-88] states that:

$$V/V_o \ = \ 1 - \exp \ (-V_{ex}) \qquad . \qquad (9.1.1)$$

where V is the total volume of the overlapped crystals, V_o is the
total volume of the space into which there are growing, and V_{ex} is
the volume they would have had neglecting overlap.

For this equation to be a true transform it requires the crystals
to be distributed in an infinite space so that boundary effects can
be ignored and that the distribution of the crystal centres be

completely random in three dimensional space.

The first requirement may be physically unrealistic, but a reasonable approximation. The second, however, will not be true if the centres are confined to a two dimensional surface even though they may be randomly distributed on such a surface.

Armstrong et al [89] considered the crystals to have right circular conical geometry and applied the Avrami equation (for a surface as opposed to a three-dimensional space) for the overlap of circular discs comprising thin slices of the cones at heights above the surface. This gave current-time transients of the following form

$$i = nFk_2[1-\exp(-\pi N_o k_1{}^2 M^2 t^2/\rho^2)] \qquad (9.1.2)$$

for instantaneous nucleation and

$$i = nFk_2[1-\exp(-\pi M^2 k_1{}^2 A t^3/3\rho^2)] \qquad (9.1.3)$$

for progressive nucleation.
Where k_1 is a rate constant parallel to the plane of the electrode surface and k_2 is one for growth perpendicular to it. k_2 is related to a growth velocity V_2 (cm s^{-1}) perpendicular to the plane such that $k_2 = \rho V_2/M$.

Armstrong et al [89] also consider three dimensional growth leading to passivation.

They assume that the velocity of advance orthogonal to the electrode surface, V_2, is proportional to the uncovered surface area which gives the following current-time transients:

$$i = nFk_2[1-\exp(-\pi N_o k_1{}^2 M^2 t^2/\rho^2)]\exp(-\pi N_o k_1{}^2 M^2 t^2/\rho^2) \quad (9.1.4)$$

for instantaneous nucleation and

$$i = nFk_2[1-\exp(-\pi M^2 k_1{}^2 A t^3/3\rho^2)]\exp(-\pi M^2 k_1{}^2 A t^3/3\rho^2) \quad (9.1.5)$$

for progressive nucleation.

Although the geometry of crystal growth was assumed to be conical, this is not in fact the case since the rate of growth parallel to the surface is constant, that orthogonal to it is time dependent. Bosco and Rangarajan have recently reported this [92].

Since the Armstrong system [89] has formed the basis of many discussions of electrochemical passivation [93,94] and one often gets the impression that the crystal shape is fixed, the actual geometry that results from this model will be examined in detail in the next section.

9.2 Derivation of the crystal growth geometry in the Armstrong Model

The velocity of growth perpendicular to the plane is proportional to the uncovered surface area, which is given by

$$V_2 = V_{20} \exp(-\pi N_o k_1^2 M^2 t^2/\rho^2) \qquad (9.2.1)$$

for instantaneous nucleation, where V_{20} is the constant of proportionality.

If $\alpha = \pi N_o k_1^2 M^2/\rho^2$ and x is the height above the electrode surface, then x as a function of time is given by

$$x = V_{20}(\pi/\alpha)^{\frac{1}{2}}/2 \ \mathrm{erf}(\alpha^{\frac{1}{2}}t) \qquad (9.2.2)$$

Because the growth rate parallel to the plane is constant we have

$$dr/dt = k_1$$

and the radius as a function of height can be found

$$r(x) = k_1(t - t_x) \quad t > t_x \qquad (9.2.3)$$

$$r(x) = 0 \qquad\qquad t < t_x \qquad (9.2.4)$$

where t_x is the time at which the crystal reaches height x above the electrode surface - obtained from equation (9.2.2). Figure 9.2.1 shows the crystal shape at various times and coverages. It can be seen that the geometry of crystal growth is constantly changing. The growth commences from a nucleus in the right circular conical format but the shape becomes progressively flattened in the plane parallel to the electrode surface as growth proceeds. This ultimately results in there being a maximum height, above which the crystals do not grow.

Fig. 9.2.1   Evolution of Crystal Shape with Time
for Instantaneous Nucleation
$V_{20}=1.0, \alpha=0.5, k_1=1.0$
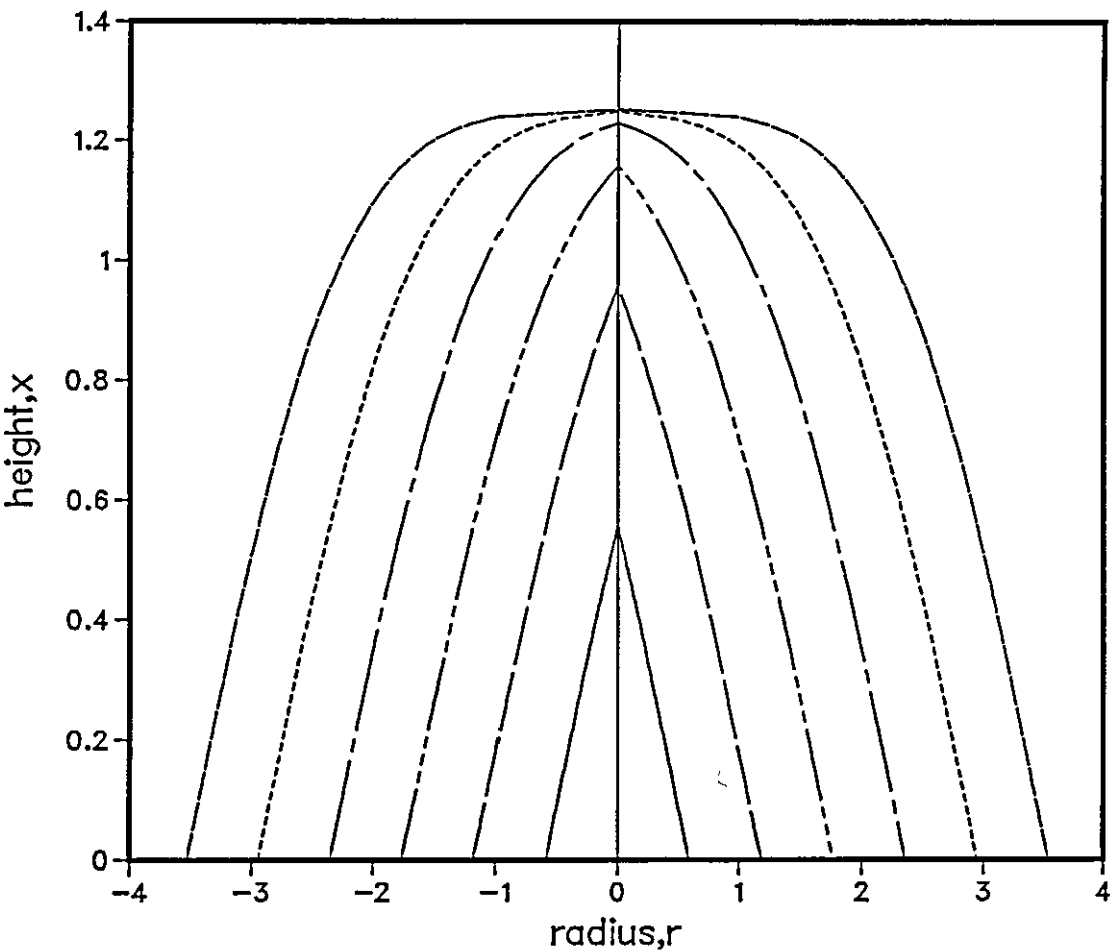
$t=0.5t_{max}$

$t=1.0t_{max}$

$t=1.5t_{max}$

$t=2.0t_{max}$

$t=2.5t_{max}$

$t=3.0t_{max}$

For progressive nucleation, instead of equation (9.2.1), the perpendicular growth rate is given by

$$V_2 = V_{20} \exp \left(-\pi A k_1^2 M^2 t^3 / 3\rho^2 \right) \tag{9.2.5}$$

now if $\beta = (\pi A k_1^2 M^2 / 3\rho^2)$ and x is again the height above the electrode surface, then

$$x = V_{20} \int_{\tau-u}^{\tau} \exp(-\beta t^3) dt \tag{9.2.6}$$

Here u is the age of the nucleus, τ is the present time and $\tau_{nucl} = \tau - u$, the nucleation time.

Figures 9.2.2 illustrate how the rate of growth perpendicular to the surface depends on the uncovered area at different nucleation times. If the nucleus is formed at t = 0 (Figure 9.2.2(a)) the form of the crystal is similar to that seen for instantaneous nucleation.

A gradual evolution from conical to "bullet" shape is noticed as perpendicular growth is suppressed. If nucleation occurs at $t = 0.5t_{max}$ (Figure 9.2.2(b)) the bullet shape is immediately evident and the height attained by the growing crystal is less than half that of a crystal nucleated at t = 0. By the time the i - t growth transient has reached the maximum, newly nucleated crystals (Figure 9.2.2(c)) have their vertical growth curtailed almost immediately and their resultant height is approximately 2 orders of magnitude less than $t_{nuc} = 0$.

The following conclusions can be made.

(i) The geometry of a crystal growth from a single nucleus is not only non-conical but its form evolves with time.

(ii) There can be a maximum height above which the crystal does not grow. Figure 9.2.3 shows this maximum height as a function of nucleation time.

(iii) For the case of progressively nucleated growth the evolving crystal shape is dependent upon the time at which the nucleation centre is born.

Fig. 9.2.2a Evolution of Crystal Shape with Time
for Progressive Nucleation
(nucleation time is 0.0)
$V_{2o}=1.0, \beta=0.5, k_1=1.0$
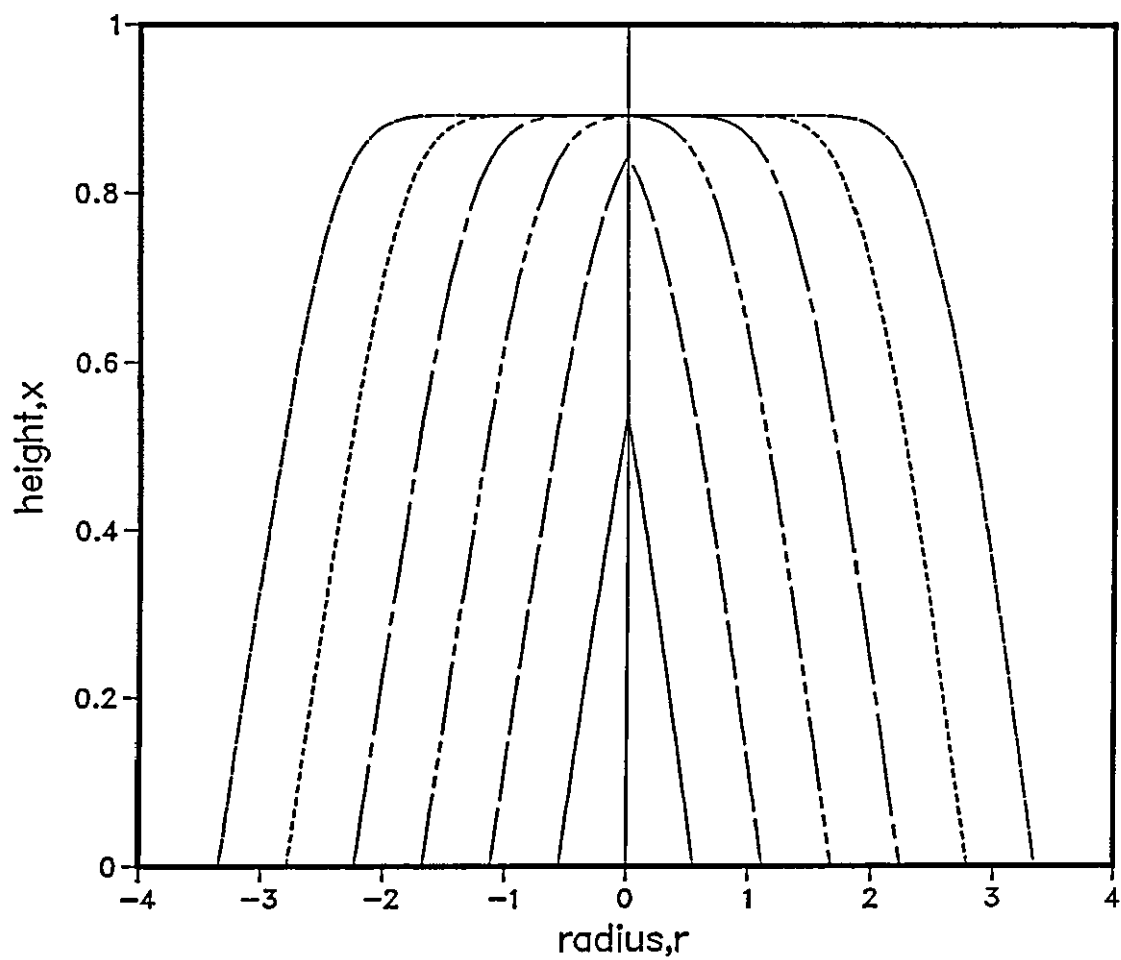
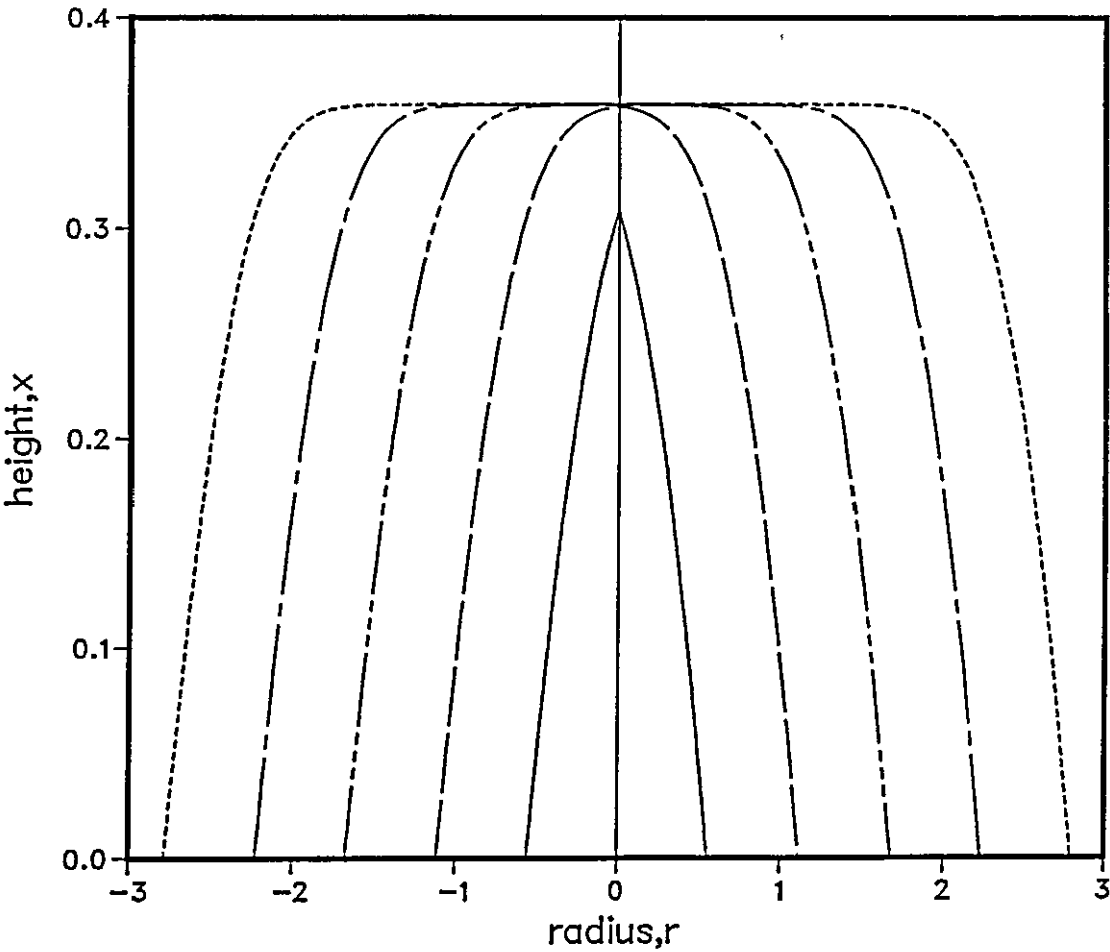$t=0.5t_{max}$ ____

$t=1.0t_{max}$ ____ .

$t=1.5t_{max}$ ____

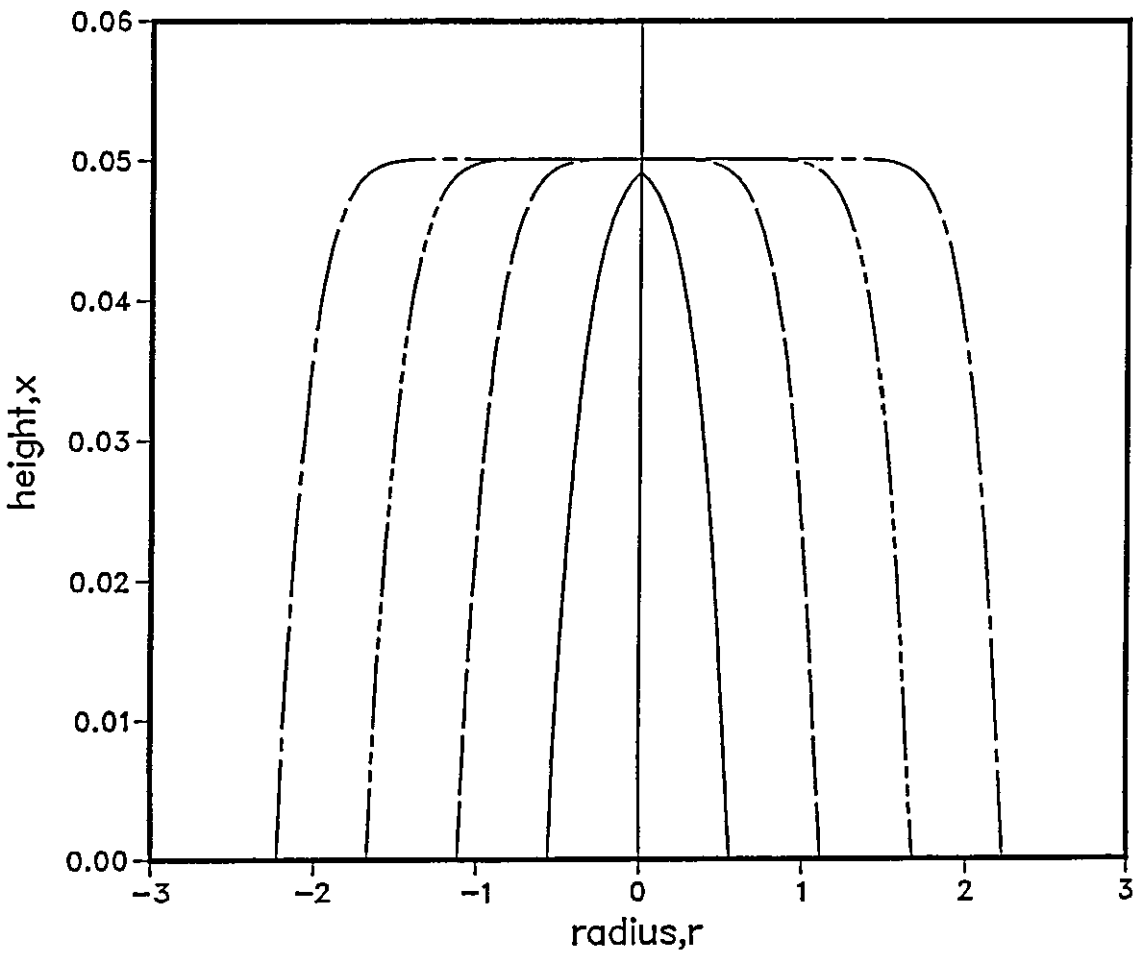$t=2.0t_{max}$ ____

$t=2.5t_{max}$ ------

$t=3.0t_{max}$ ____

Fig. 9.2.2b Evolution of Crystal Shape with Time
for Progressive Nucleation
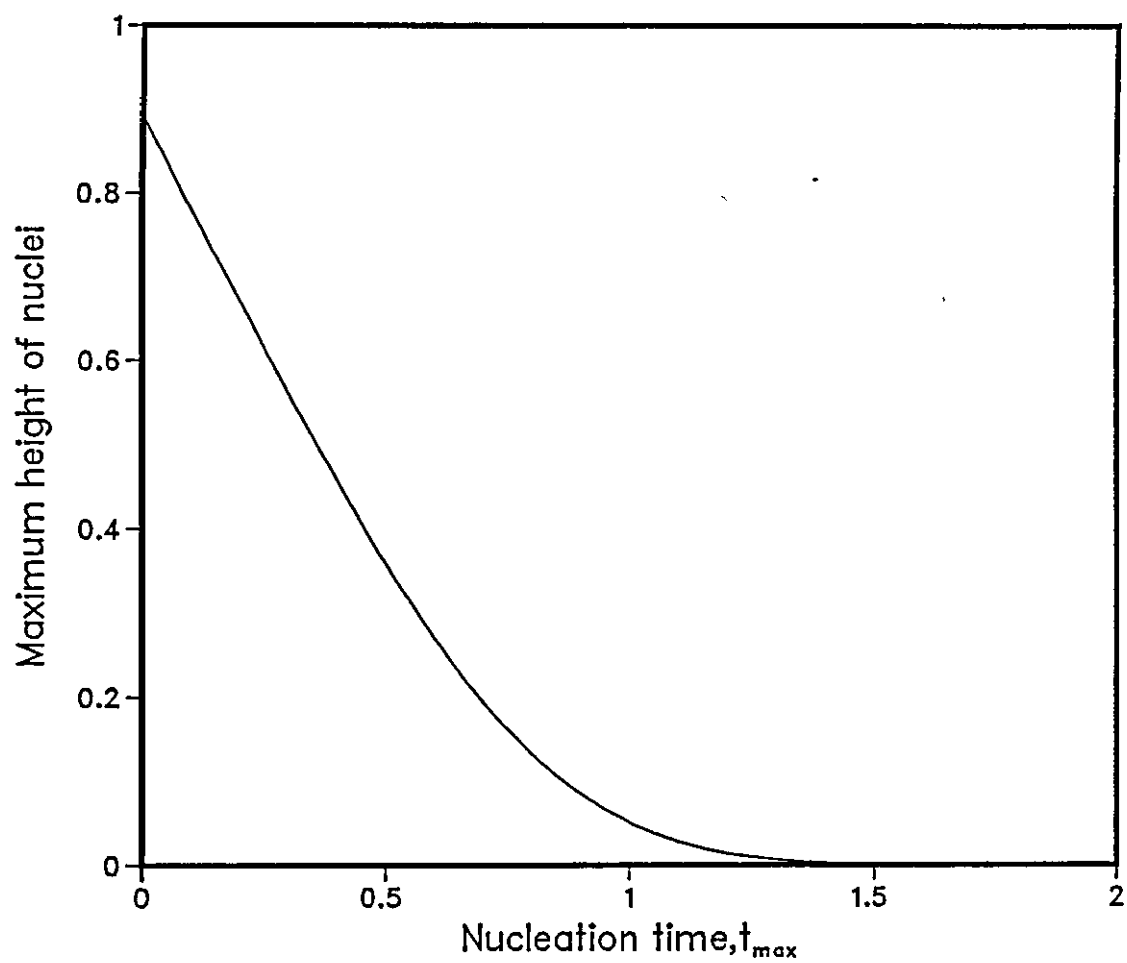(nucleation time is $0.5t_{max}$)
$V_{20}=1.0, \beta=0.5, k_1=1.0$

$t=1.0t_{max}$ _____

$t=1.5t_{max}$ _____ .

$t=2.0t_{max}$ _____

$t=2.5t_{max}$ _____

$t=3.0t_{max}$ ------

Fig 9.2.2c Evolution of Crystal Shape with Time
for Progressive Nucleation
(nucleation time is $1.0t_{max}$)
$V_{2o}=1.0, \beta=0.5, k_1=1.0$

height,x

radius,r

$t=1.5t_{max}$ _____

$t=2.0t_{max}$ _____ ._

$t=2.5t_{max}$ _____

$t=3.0t_{max}$ _____

Fig. 9.2.3 Maximum Height of Nuclei as a Function
of Nucleation Time
$V_{2o}=1.0, \beta=0.5, k_1=1.0$

9.3 The need for a new model

Fletcher and Mathews [95] comment on the physical plausibility of the Armstrong Model. They suggest that as the rate of lateral growth is under 'interfacial control' and the vertical spreading is under diffusion control a dendritic growth form should result. They continue by saying that were the growth truly diffusion controlled, the rates of growth in both directions should be limited by mass transport processes.

The purpose of this chapter will be to derive an electro-crystallization model where crystal growth occurs in a shape-preserving way.

The need for a new model is also demonstrated by the failure of the Armstrong Model to predict the current-time transients for long times.

Armstrong et al themselves [89] and Barradas et al [96] report a 'tailing' phenomenon at long times $\sim 2t/tm$ for the Hg/HgO system, i.e. the experimental plots return to zero much more slowly than equations (9.1.2) and (9.1.3) predict.

The next section illustrates the fact that forcing the crystals to grow in fixed geometry results in a much slower 'tail-off'.

9.4 Formulation of the new model and calculation of Current-time Transients

The mechanism for processes occurring at the electrode-electrolyte interface are assumed to be represented by:

$$M \underset{k_b}{\overset{k_f}{\rightleftharpoons}} M^{n+}_{ads} + ne^- \qquad (9.4.1)$$

followed by

$$M^{n+}_{ads} + nX^- \overset{k_L}{\longrightarrow} MX_{n\ lat} \qquad (9.4.2)$$
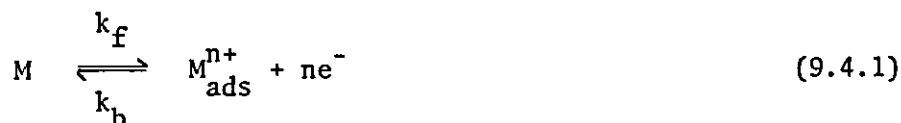
For example, in the case of a silver electrode in a solution of HCl, M would be Ag and X would be Cl^-. M^{n+}_{ads} is the participating species which has been expelled from the electrode substate and become a surface adsorbed species. MX_{nlat} is the species which is subsequently incorporated into the passivating lattice.

- 68 -

The growth of the crystals is assumed to occur in a fixed habit, the physical justification for which was given in the previous section.

In equation (9.4.2) it is the incorporation of species into the lattice which is assumed to be the slow step. The surface diffusion and reaction with X are assumed to be rapid in comparison.

It is also assumed that the adsorbed species is mobile on both the electrode surface and the deposited crystal surface. Whether the adsorbed species is M^{n+} or MX or M^{n+} on the metal surface and MX on the crystal surface is irrelevant to the kinetics as the reaction with X^- has been assumed to be fast; it will be written as M^{n+}_{ads} for convenience.

For the forward reaction in equation (9.4.1) the rate will be proportional to the uncovered surface area, with rate constant, k_f. The rate of the back reaction will be proportional to the surface concentration of the adsorbed species multiplied by the uncovered surface area, with rate constant, k_b. For the lattice incorporation step (9.4.2), the rate will be proportional to the surface concentration of the adsorbed species multiplied by the number of available incorporation sites per unit base area of the growing crystals, with rate constant, k_L.

This gives rise to the following kinetics:

$$i/nF = d\,M/dt = k_f \theta_{uncov} - k_b\, M^{n+}_{ads}\, \theta_{uncov}/A_o \qquad (9.4.3)$$

$$d\,M^{n+}_{ads}/dt = k_f \theta_{uncov} - k_b\, M^{n+}_{ads}\, \theta_{uncov}/A_o - k_L\, M^{n+}_{ads}\, S/A_o \qquad (9.4.4)$$

$$d\,MX_{n\ lat}/dt = k_L\, M^{n+}_{ads}\, S/A_o \qquad (9.4.5)$$

Where M^{n+}_{ads} and $MX_{n\ lat}$ are the number of each species in the mobile state and incorporated into the lattice respectively, θ_{uncov} is the uncovered area and S is the number of incorporation sites in the total area of the passivating crystals, A_o is the total electrode surface area, i is the current, n is the number of electrons transferred and F is the Faraday constant.

As the adsorbed species is mobile over the entire electrode surface area, covered or uncovered, the surface concentration will be equal to M^{n+}_{ads}/A_o.

θ_{uncov}, S and V, the total volume of all the passivating crystals can be determined by applying the Kolmogoroff-Avrami-Evans theorem [86-88] to right circular cones or hemispheres [89].

9.4.1 The case of conical growth from instantaneous nucleation of centres

If the basal radius of the conical crystals at any time instant is represented by R(t) then for N_o nuclei

$$\theta_{cov} = A_o(1 - \exp(-N_o \pi R^2/A_o)) \tag{9.4.6}$$

where A_o is the total electrode area. Hence

$$\theta_{uncov} = A_o \exp(-N_o \pi R^2/A_o) \tag{9.4.7}$$

V can be found by considering the overlap of slices, height h above the electrode, thickness dh and radius x, thus

$$x = R - h/a \tag{9.4.8}$$

where a is the ratio of the height to basal radius of the cones.

So, dV the elemental volume for this slice is found by applying the Avrami equation to the overlap of the circular slices at height h above the electrode. Therefore

$$dV = A_o(1 - \exp(-\pi N_o x^2/A_o))dh \tag{9.4.9}$$

Substituting for x and integrating from h = 0 to h = R gives

$$V = \int_{h=0}^{R} A_o(1 - \exp(-\pi N_o(R - h/a)^2/A_o))dh \tag{9.4.10}$$

If it is assumed that the area of the overlapped cones available for reaction, S, is given by

$$S = \partial V/\partial R \tag{9.4.11}$$

S can be found by differentiating equation (9.4.10) w.r.t. R using a change of variable

$$u = R - h/a \ , \quad du = -dh/a$$

So

$$S = \frac{\partial}{\partial R} \left\{ A_o a \int_{u=0}^{R} (1 - \exp(-\pi N_o u^2/A_o)) du \right\} \qquad (9.4.12)$$

$$S = A_o a (1 - \exp(-\pi N_o R^2/A_o)) \qquad (9.4.13)$$

It can be seen that S is just the constant factor a multiplied by θ_{uncov}, so that S is not the true surface area of the overlapped cones, but is proportional to the number of sites available for reaction and hence is then the effective surface area that is required. This is clearly seen when each cone is visualised as a number of stacked discs. The incorporation sites are restricted to the perimeter of each disc.

If ρ is the density of the deposit and M is its relative molecular mass then

$$MX_{n \ lat} = \rho V/M \qquad (9.4.14)$$

Thus from equation (9.4.5)

$$(\rho/M)(\partial V/\partial t) = k_L M_{ads}^{n+} S/A_o$$

so that

$$M_{ads}^{n+} = (\rho A_o/Mk_L S)(\partial V/\partial t) \qquad (9.4.15)$$

substituting this expression into equation (9.4.4) gives

$$\frac{\partial}{\partial t} \left\{ (\rho A_o/Mk_L S)(\partial V/\partial t) \right\} = k_f \theta_{uncov} - (k_b \theta_{uncov} \rho/Mk_L S)(\partial V/\partial t) - (\rho/M)(\partial V/\partial t)$$
$$(9.4.16)$$

Similarly substituting into equation (9.4.3) gives

$$i/nF = k_f \theta_{uncov} - (k_b \theta_{uncov} \rho/Mk_L S)(\partial V/\partial t) \qquad (9.4.17)$$

Using the relationships

$$\partial V/\partial t = (\partial V/\partial R).(\partial R/\partial t) \qquad (9.4.18)$$

and

$$\partial V/\partial R = S \qquad (9.4.11)$$

hence

$$\partial V/\partial t = S(\partial R/\partial t) \qquad (9.4.19)$$

so that

$$\frac{\partial}{\partial t}\left((1/S)(\partial V/\partial t)\right) = \partial^2 R/\partial t^2 \qquad (9.4.20)$$

Equation (9.4.16) becomes

$$\partial^2 R/\partial t^2 + \partial R/\partial t(k_b\theta_{uncov} + k_L S)/A_o - (M/\rho)k_L k_f\theta_{uncov}/A_o = 0 \qquad (9.4.21)$$

Substituting for S and θ_{uncov} from equations (9.4.13) and (9.4.7) we arrive at

$$(\partial^2 R/\partial t^2)+(\partial R/\partial t)\{k_b\exp(-N_o\pi R^2/A_o)+k_L a(1-\exp(-N_o\pi R^2/A_o))\}$$
$$- (Mk_L k_f/\rho)(\exp(-N_o\pi R^2/A_o)) = 0 \qquad (9.4.22)$$

and from (9.4.17) the current is given by

$$i/nF = A_o \exp(-N_o\pi R^2/A_o)\{k_f - (k_b\rho/(k_L M))\partial R/\partial t\} \qquad (9.4.23)$$

Equation (9.4.22) is a second order differential equation in R, which can be solved numerically. Solutions were obtained by applying a variable-order, variable-step, Gear method for a Stiff System. (This system can become stiff for certain values of rate constants k_f, k_b and k_L). The routine employed was DO2EBF from the NAG FORTRAN library [97].

The routine requires initial values for R and $\partial R/\partial t$. Obviously at t = 0, R (the basal radius of the as yet unnucleated cones) must also be set to zero. The value of $\partial R/\partial t$ at t = 0 was set by assuming that the concentration of mobile species within the vicinity of the electrode, M^{n+}_{ads}, is zero therefore from equation (9.4.15)

$$M^{n+}_{ads} = (\rho A_o/Mk_L S)\ \partial V/\partial t = 0 \qquad (9.4.24)$$

Therefore using (9.4.19)

$$O = (\rho A_o/Mk_L) \, \partial R/\partial t$$

giving

$$\partial R/\partial t = 0 \text{ at } t = 0$$

Current time plots obtained by our numerical method of solving for R as a funtion of t and substituting into equation (9.4.22) are presented in Figures 9.4.1 a-d. Each figure shows the variation of one of the parameters, k_f, k_b, k_L, or N_o/A_o. It can be seen that the resulting current-time transients consist of a falling section followed by a maximum and a slow 'tail-off' to zero, although for some values of the parameters a single falling transient results.

An initial falling transient can be observed for many electro-crystallization experiments, but is usually ignored.

The value of the initial current is equal to the rate constant k_f. It is also this constant which determines the current at long times, although the nuclei density N_o/A_o also has an effect, as might be expected (the greater the nuclei density the faster overlap and coverage of the surface occurs, which results in conical crystals of less height and therefore less volume and consequently the total charge passed will be less).

The rate constants k_b and k_L determine the positions of the maximum and minimum, along with k_f and N_o/A_o.

The non-linearity of R(t) is shown in Figure 9.4.2.

9.4.2 The case of conical growth with progressive nucleation
       of centres

In this case the nuclei are assumed to form according to the rate function

$$N = N_o(1 - \exp(-At)) \tag{9.4.25}$$

where N is the number of nuclei at any instant t, N_o is the total number of nuclei and A is the nucleation rate constant.

No approximation for short times is made as we wish to find a current-time transient over the whole time range.

A similar differential equation to that applied in the instantaneous case, can be written; however, the equation for the surface area θ_{cov} is given by

Fig. 9.4.1a   Instantaneous Nucleation of Cones
Variation of k_L
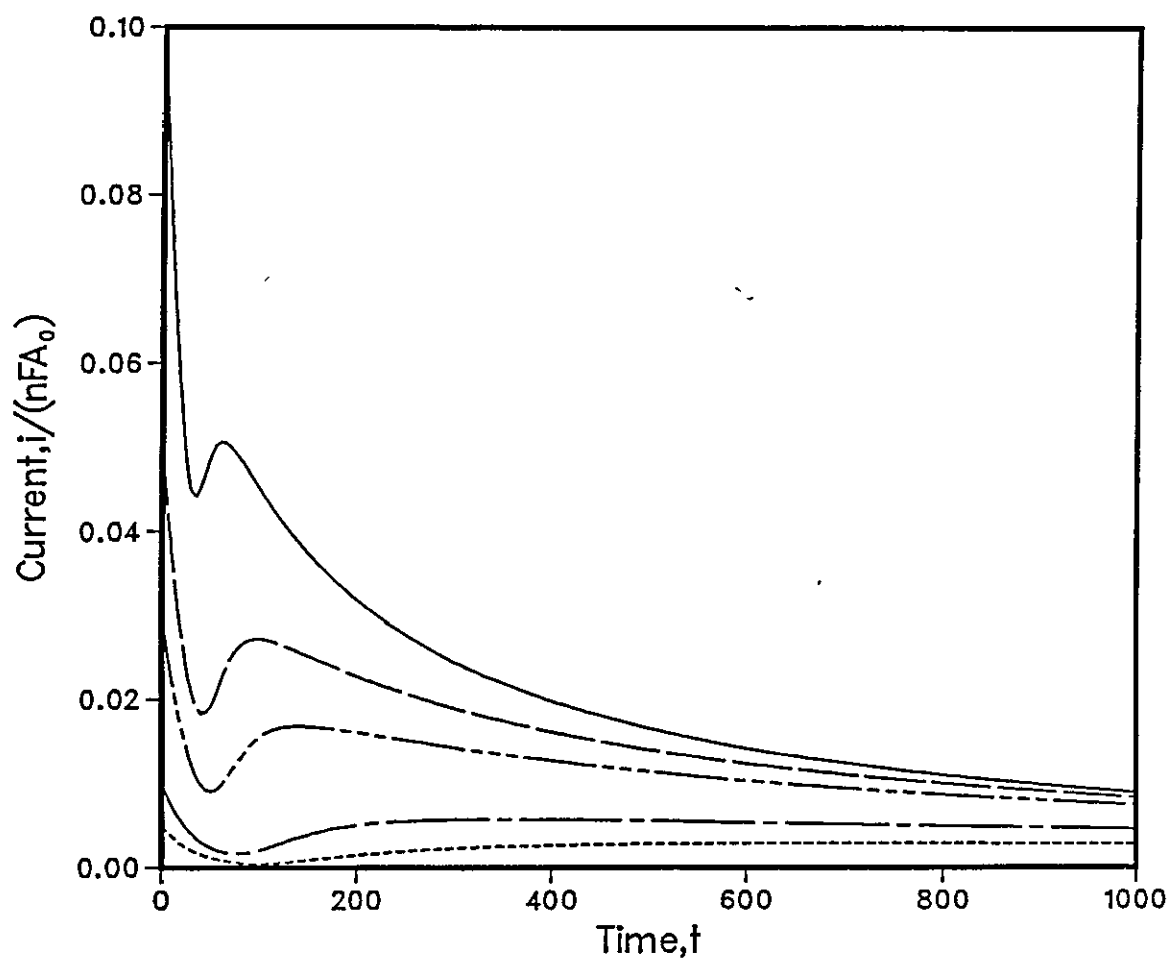$k_f = 3.0E-2, k_b = 3.0E-2, \pi N_o/A_o = 1.0E-3, M/\rho = 1.0$
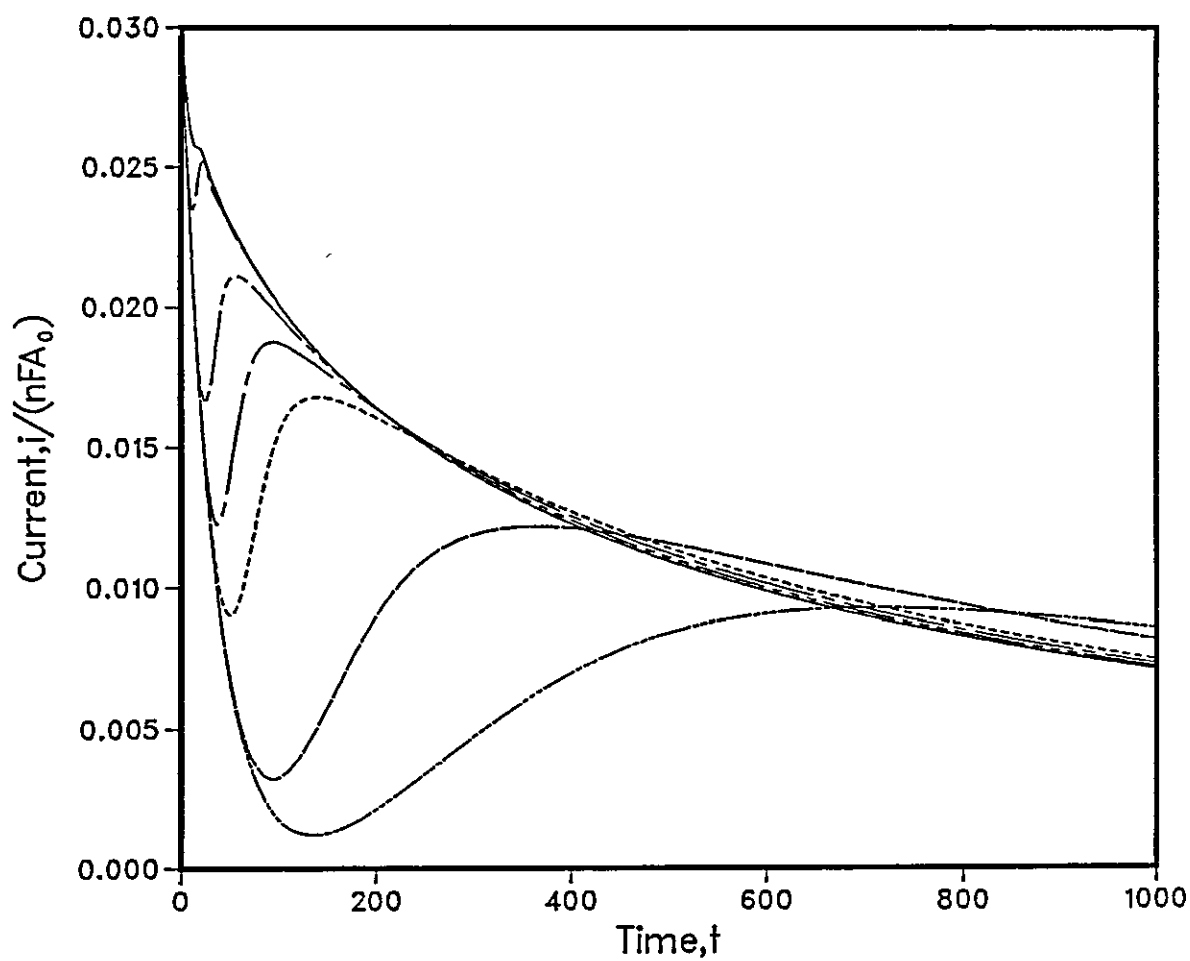
$k_L = 1.0E1$ _____

$k_L = 5.0E0$ ___ .

$k_L = 1.0E0$ ___

$k_L = 5.0E-1$ ___

$k_L = 3.0E-1$ ....

$k_L = 1.0E-1$ ___

$k_L = 5.0E-2$ ___

Fig. 9.4.1b   Instantaneous Nucleation of Cones
Variation of k_b
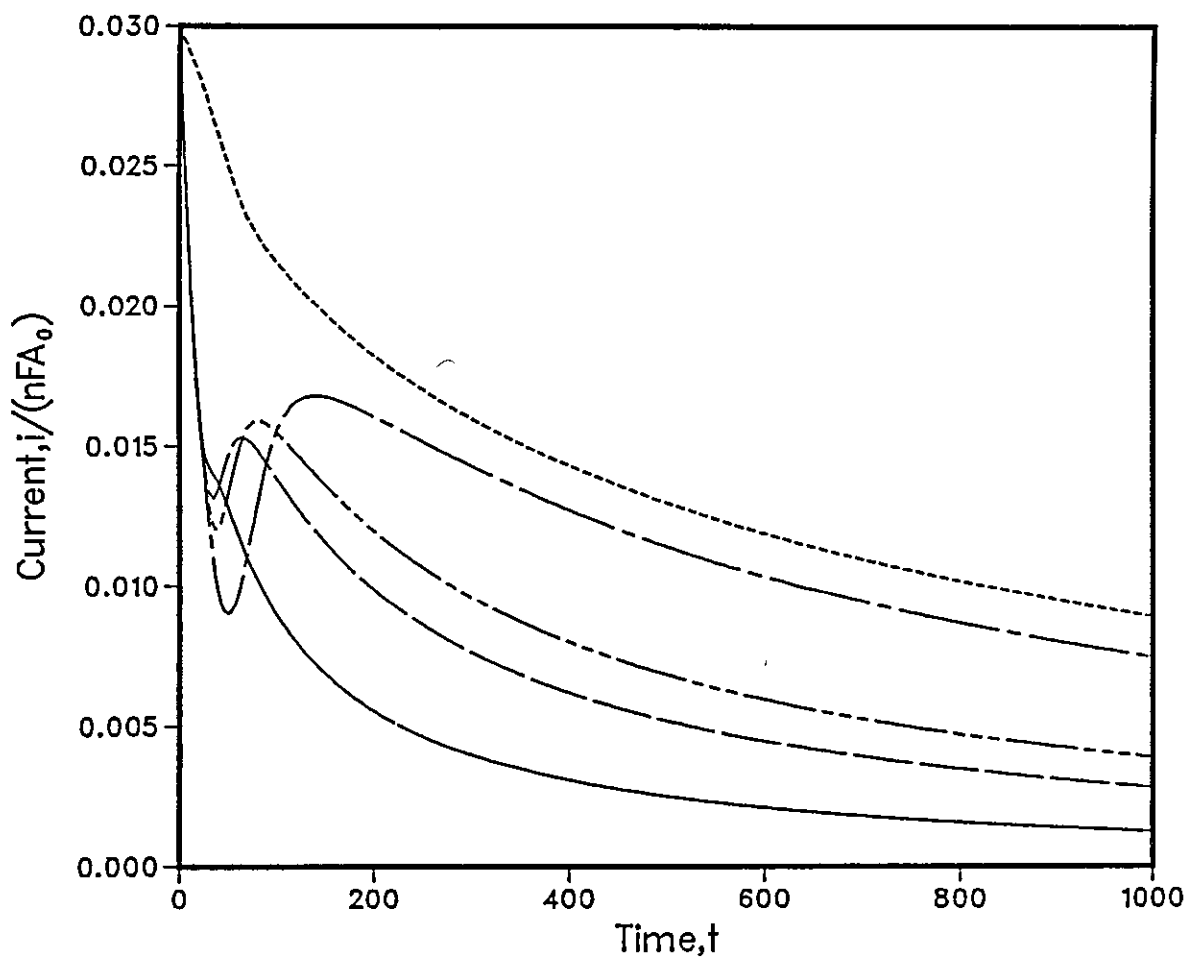$k_f=3.0E-2, k_L=3.0E-1, \pi N_0/A_0=1.0E-3, M/\rho=1.0$
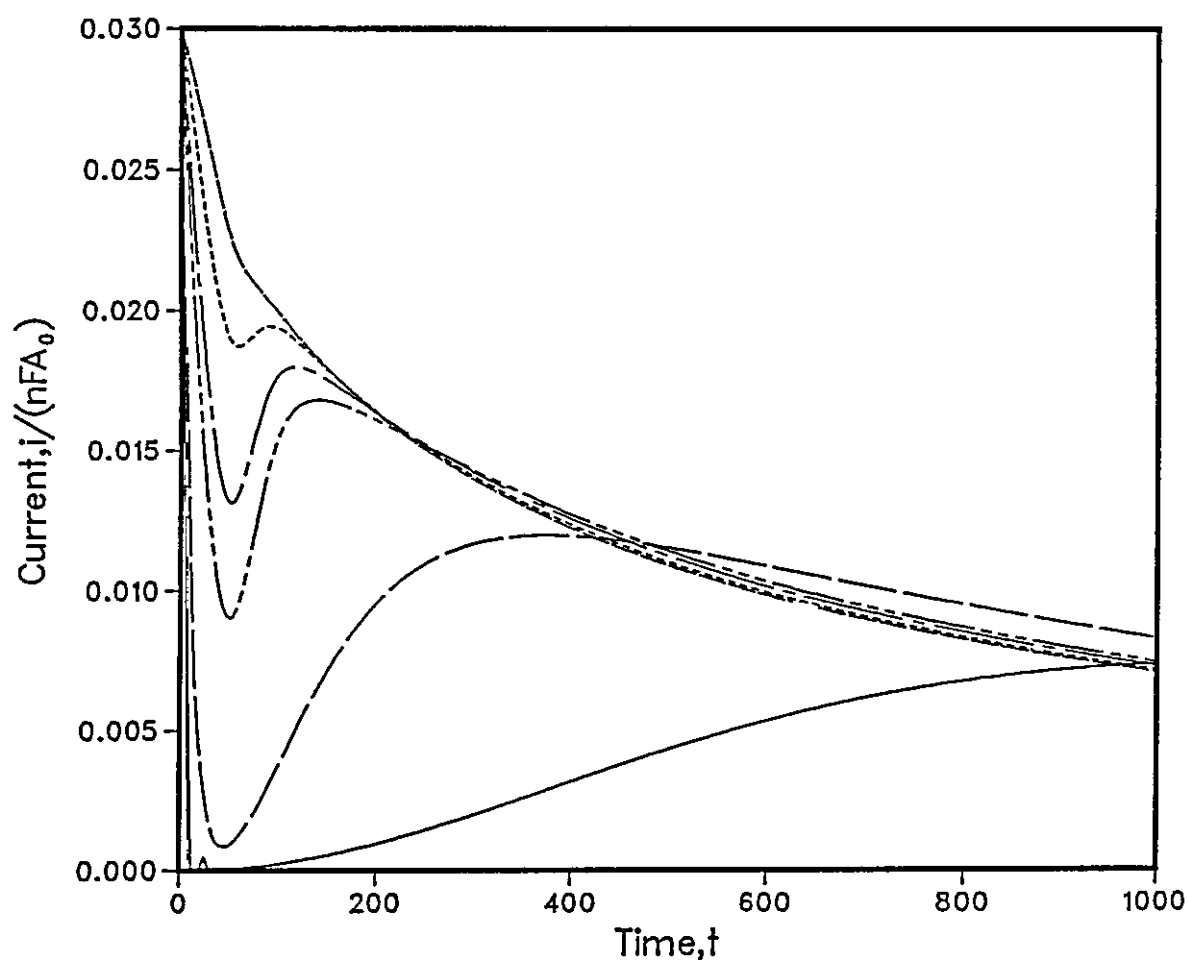
$k_b=3.0E-1$

$k_b=1.0E-1$

$k_b=3.0E-2$

$k_b=2.0E-2$

$k_b=1.0E-2$

$k_b=5.0E-3$

Fig. 9.4.1c   Instantaneous Nucleation of Cones
Variation of k_f
$k_b=3.0E-2, k_L=3.0E-1, \pi N_0/A_0=1.0E-3, M/\rho=1.0$

$k_f=1.0E-1$ _____

$k_f=5.0E-2$ _____ .

$k_f=3.0E-2$ _____

$k_f=1.0E-2$ _____

$k_f=5.0E-3$ - - - -

Fig. 9.4.1d   Instantaneous Nucleation of Cones
Variation of $\pi N_0/A_0$
$k_f=3.0E-2, k_b=3.0E-2, k_L=3.0E-1, M/\rho=1.0$

$\pi N_0/A_0=5.0E-2$

$\pi N_0/A_0=1.0E-2$

$\pi N_0/A_0=5.0E-3$

$\pi N_0/A_0=1.0E-3$

$\pi N_0/A_0=5.0E-4$

Fig. 9.4.2   Radii of Cones vs. Time for the Same Parameter
Values as Fig 9.4.1a
$k_t=3.0E-2, k_b=3.0E-2, \pi N_o/A_o=1.0E-3, M/\rho=1.0$
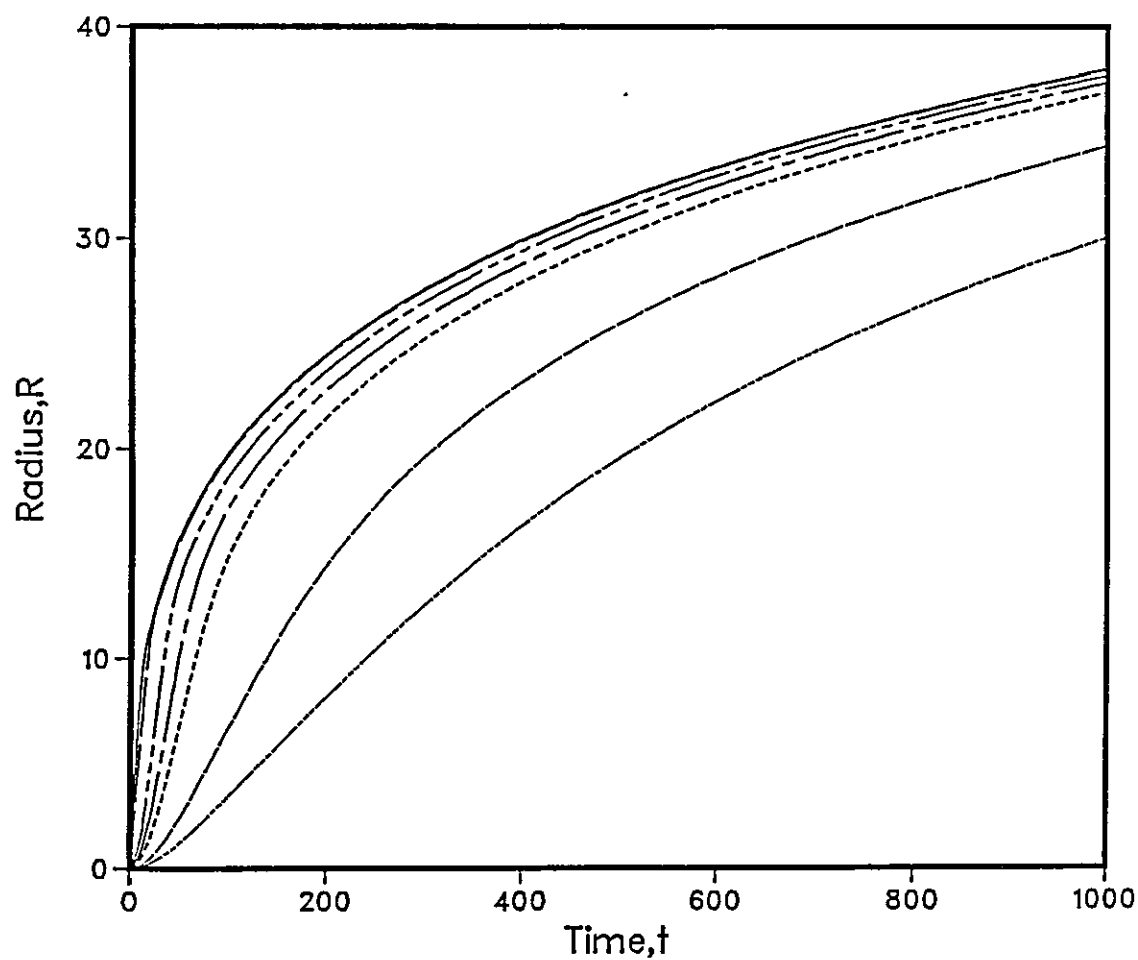
$$\theta_{cov} = A_o(1 - \exp(-S_{ext})) \qquad (9.4.26)$$

where S_{ext} is the fractional extended surface area (the area that would exist without overlap). For the instantaneous case S_{ext} is simply $\pi N_o R^2/A_o$, but for progressive nucleation S_{ext} must be given by

$$S_{ext} = \pi/A_o \sum_{i=1}^{i=t/\delta t} n_i r^2_i \qquad (9.4.27)$$

n_i is the number of nuclei formed during a time interval $((i-1)\delta t, i\delta t)$ and r_i is the radius at time t of nuclei of age u, where $u = t - i\delta t$.

For crystal growth without passivation R is a linear function of t. In our model for passivation from instantaneous nucleation R(t) is initially linear but eventually approaches a limit. For the progressive case we assume that the radii of all nuclei, whatever their age, increase at the same rate (Figure 9.4.3). It can be seen that for a nucleus of age u, the radius as a function of time will be given by

$$r = r(t) - r(u) \qquad (9.4.28)$$

The number of nuclei nucleated at time u in the time interval du will be given by

$$n_u = (\partial N/\partial t)_{t-u} du \qquad (9.4.29)$$

equation (9.4.27) then takes on the form

$$S_{ext} = \pi/A_o \int_o^t \{r(t) - r(u)\}^2 (\partial N/\partial t)_{t-u} \, du \qquad (9.4.30)$$

To perform this integration at each time step, in the numerical solution, would consume an excessive amount of computational time. In order to avoid this a relationship between $S_{ext}(t + \Delta t)$ and $S_{ext}(t)$ was derived. Thus, from equation (9.4.27):

$$S_{ext}(\tau) = \pi/A_o \sum_{i=1}^{\tau/\delta t} n_i r_i^2 \qquad (9.4.27)$$

- 74 -

Fig. 9.4.3   Schematic Representation of Radii of Cones
as a Function of Time for Cones Nucleated at Different Times
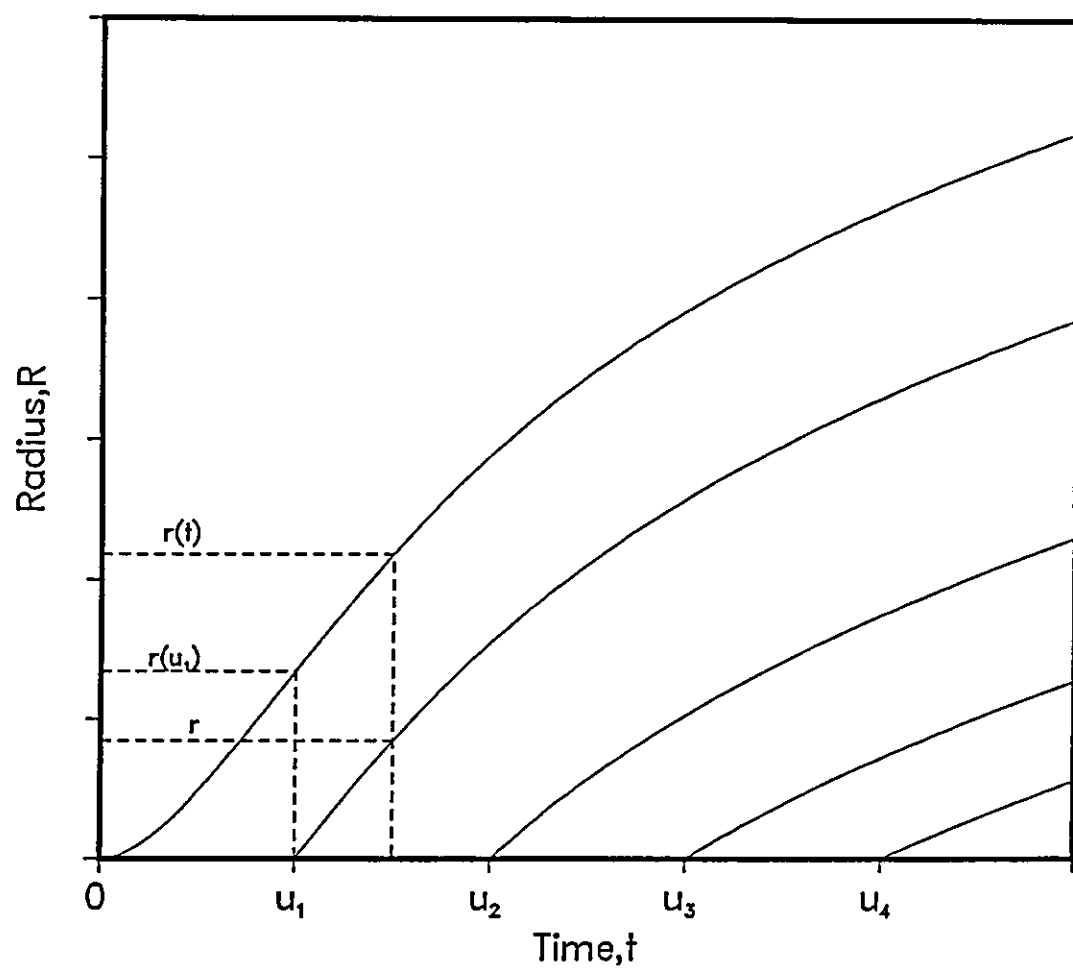
in the time interval Δt, the radii of all nuclei will increase by the same degree,

$$\Delta r = (\partial r/\partial t)_\tau \Delta t \qquad (9.4.31)$$

where r is the radius of nuclei formed at t = 0.

So that

$$S_{ext}(\tau+\Delta t) = (\pi/A_o) \sum_{i=1}^{\tau/\delta t} n_i(r_i+\Delta r)^2 + (\pi/A_o)(\partial N/\partial t)_\tau \Delta t(\Delta r)^2 \qquad (9.4.32)$$

that is, the number of existing nuclei multiplied by their new radius squared added to the number of new nuclei formed in the time interval Δt multiplied by $(\Delta r)^2$.

This becomes

$$S_{ext}(\tau+\Delta t) = (\pi/A_o)[\sum_{i=1}^{\tau/\delta t} n_i r_i^2 + 2\Delta r \sum_{i=1}^{\tau/\delta t} n_i r_i + (\Delta r)^2 \sum_{i=1}^{\tau/\delta t} n_i$$

$$+ (\partial N/\partial t)_\tau \Delta t(\Delta r)^2] \qquad (9.4.33)$$

$$= S_{ext}(\tau) + (\pi/A_o[2\Delta r \sum_{i=1}^{\tau/\delta t} n_i r_i + N(\tau)(\Delta r)^2 + (\partial N/\partial t)_\tau \Delta t(\Delta r)^2] \qquad (9.4.34)$$

If the following function is defined

$$R_{ext}(\tau) = \sum_{i=1}^{\tau/\delta t} n_i r_i \qquad (9.4.35)$$

A relationship between $R_{ext}(\tau)$ and $R_{ext}(\tau+\Delta t)$ must be derived as follows

$$R_{ext}(\tau+\Delta t) = \sum_{i=1}^{\tau/\delta t} n_i(r_i+\Delta r) + (\frac{\partial N}{\partial t})_\tau \Delta t\Delta r \qquad (9.4.36)$$

- 75 -

which becomes

$$R_{ext}(\tau+\Delta t) = R_{ext}(\tau) + N(\tau)\Delta r + (\frac{\partial N}{\partial t})_\tau \Delta t \Delta r \qquad (9.4.37)$$

From equation (9.4.25)

$$N(\tau) = N_o(1 - \exp(-A\tau)) \qquad (9.4.25)$$

and

$$(\partial N/\partial t)_\tau = N_o A \exp(- A\tau) \qquad (9.4.38)$$

$$\Delta r = (\partial r/\partial t)_\tau \Delta t \qquad (9.4.31)$$

$\partial r/\partial t$ is calculated at each point in time during the integration of the differential equation. Thus $R_{ext}(t)$ can be calculated at each point in time as $R_{ext}(0) = 0$. Returning to equation (9.4.34) for S_{ext}.

$$S_{ext}(\tau+\Delta t) = S_{ext}(\tau)+(\pi/A_o)\{2\Delta r\Delta t R_{ext}(\tau)+N(\tau)(\Delta r)^2+(\partial N/\partial t)_\tau \Delta t(\Delta r)^2\} \qquad (9.4.39)$$

Since $S_{ext}(0) = 0$, S_{ext} can be calculated for all times during the integration by addition of terms known at that time, this avoids computing a complete integration from $t = 0$ at every point in time during the integration of the differential equation.

Thus the differential equation for progressive nucleation can be solved relatively easily, and current-time transients calculated as before. Figure 9.4.4 shows some typical current-time transients for various values of the nucleation constant A. It can be seen that as A is increased the transients approach the instantaneous limit as would be expected.

9.4.3 Instantaneous growth in hemispherical geometry

The Avrami expression can be applied to the volume calculation of overlapping hemispheres in a similar way to the calculations for cones [89]. Providing the nucleation is instantaneous the simple expression for V can be derived.

$$V = \int_o^R A_o[1 - \exp(-\pi N_o(R^2 - h^2)/A_o)]dh \qquad (9.4.40)$$

Fig. 9.4.4　Progressive Nucleation of Cones
Variation of Nucleation Constant A
$k_f=3.0E-2, k_b=3.0E-2, k_L=3.0E-1, \pi N_0/A_0=1.0E-3, M/\rho=1.0$
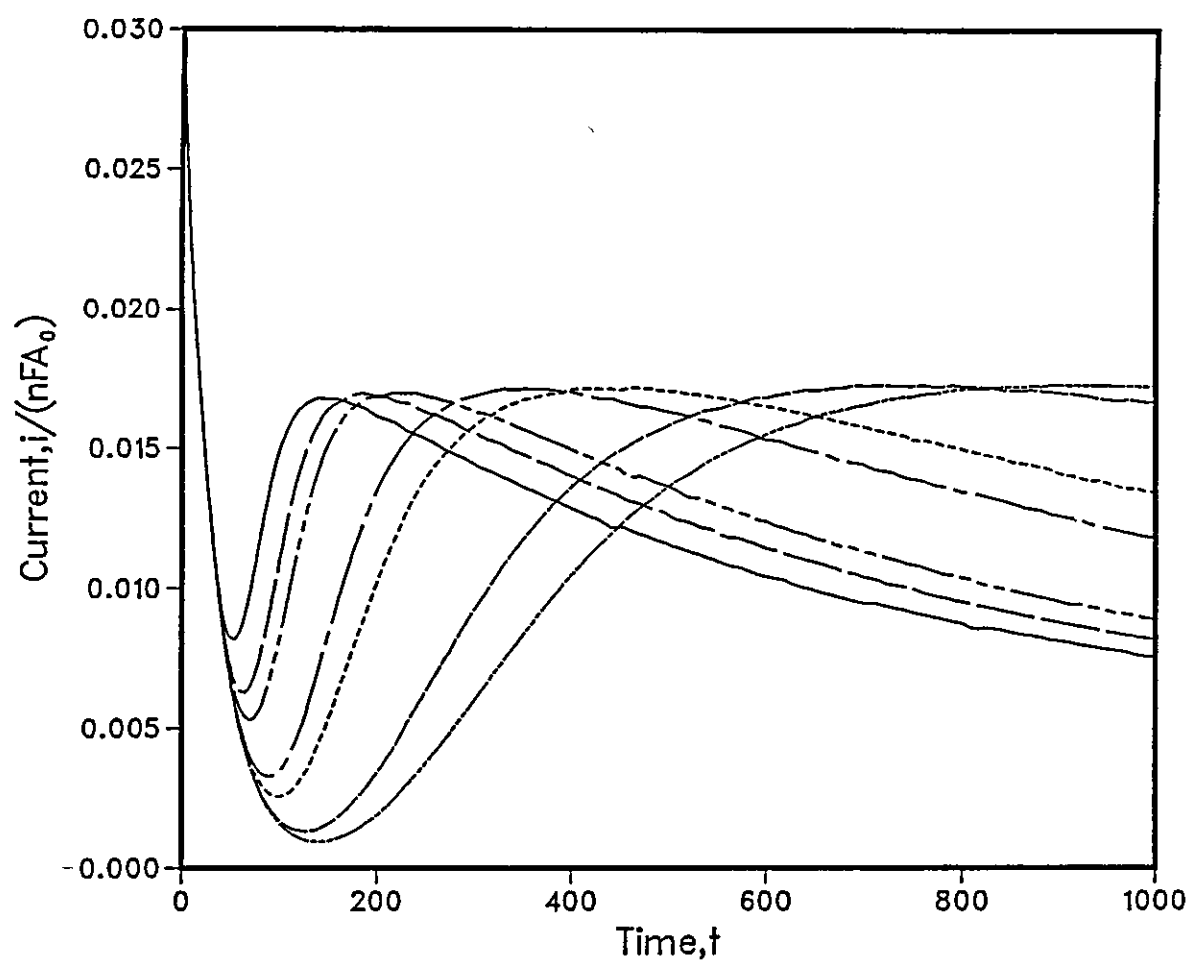
A=5.0E-2

A=1.0E-2

A=5.0E-3

A=1.0E-3

A=5.0E-4

A=1.0E-4

A=5.0E-5

The effective surface area S is given by $\partial V/\partial R$ as before, therefore

$$S = \frac{\partial}{\partial R} \{R - \exp(-\pi N_o R^2/A_o) \int_o^R \exp(\pi N_o h^2/A_o) dh\} A_o \quad (9.4.41)$$

$$\therefore \quad S = 2\pi N_o R \exp(-\pi N_o R^2/A_o) \int_o^R \exp(\pi N_o h^2/A_o) dh \quad (9.4.42)$$

The basal uncovered surface area, θ_{uncov}, will be identical to that in the conical case. Thus substituting for S in equation (9.4.21) gives

$$\partial^2 R/\partial t^2 + \partial R/\partial t (k_b \exp(-N_o \pi R^2/A_o) + k_L 2\pi N_o R \exp(-\pi N_o R^2/A_o) \int_o^R \exp(\pi N_o h^2/A_o) dh/A_o)$$

$$-(M/\rho)k_L k_f \exp(-N_o \pi R^2/A_o) = 0 \quad (9.4.43)$$

This differential equation can be solved in a similar manner to the conical case, with the integral $\int_o^R \exp(\pi N_o h^2/A_o) dh$ being evaluated as the integration of the differential equation proceeds.

The current will be given by equation (9.4.23) as before.

Figure 9.4.5 compares current-time transients for conical and hemispherical growth for the same rate constants. It shows that the shape is very similar, except that the current is greater for hemispheres, as would be expected because the volume and hence the total charge passed is greater for a hemisphere compared with a cone of height equal to its radius.
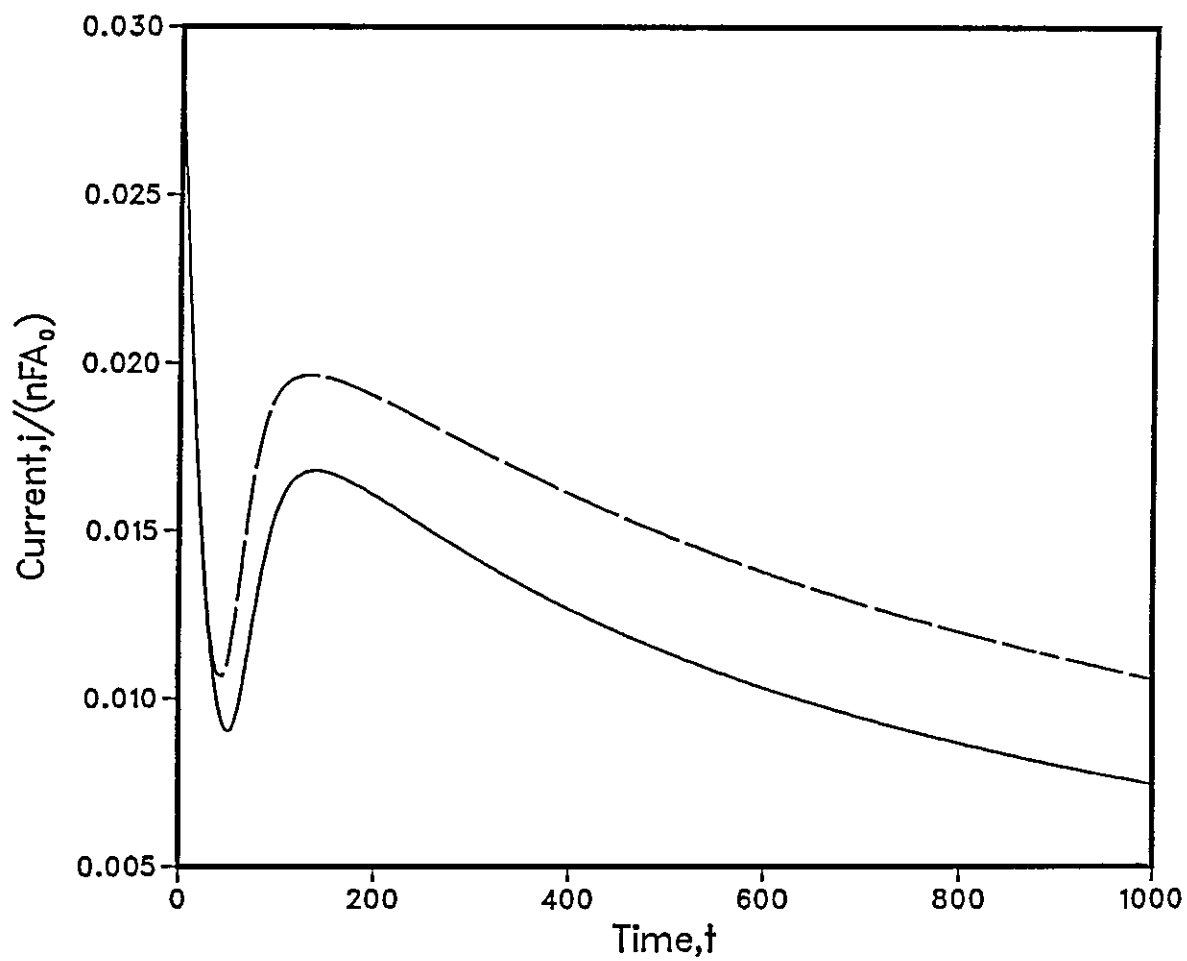
9.4.4 Instantaneous growth in cylindrical geometry

For cylinders of a constant height, H, the following expression for V and S can be easily derived.

$$V = A_o(1 - \exp(-N_o \pi R^2/A_o))H \quad (9.4.44)$$

$$S = \frac{\partial V}{\partial R} = 2N_o \pi RH \exp(-N_o \pi R^2/A_o) \quad (9.4.45)$$

Fig. 9.4.5   Comparison of Conical and Hemispherical
Growth Geometry
$k_t=3.0E-2, k_b=3.0E-2, k_L=3.0E-1, \pi N_o/A_o=1.0E-3, M/\rho=1.0$

Conical _____

Hemispherical.

Substituting for S in equation (9.4.21) gives

$$\partial^2 R/\partial t^2 + \partial R/\partial t (k_b \exp(-N_o \pi R^2/A_o) + k_L 2\pi N_o RH \exp(-N_o \pi R^2/A_o)/A_o)$$

$$+ (M/\rho)k_L k_f \exp(-N_o \pi R^2/A_o) = 0 \qquad\qquad (9.4.46)$$

and this again can be solved in a similar manner, to give current-time
plots for various values of H as shown in Figure 9.4.6.

It can be seen that as H is increased the 'tail-off' becomes much
slower and the current is greater, as would be expected as the volume
of the crystals increases. For small values of H, a sharp 'tail-off'
results and the shape is reminiscent of two-dimensional nucleation
and growth.

9.4.5 Fitting of the Model to Experimental Data

A program has been written, which varies the parameters k_f, k_b,
k_L, etc. to find the best fit to experimental data. The program used
a routine from the NAG FORTRAN Library EO4FCF [97] which minimises the
sum of the squares of the differences between calculated values and
experimental values using a combined Gauss-Newton and modified Newton
method.

Figure 9.4.7 shows the closeness of the computed fit to
experimental points. The model was the instantaneous nucleation of
cones and the data for $PbO_2/PbSO_4$ [98].

The values of the parameters obtained from the fit, were as
follows:

$$(M/\rho)k_f = 7.523 \times 10^{-2}$$
$$k_b = 3.050 \times 10^{-2}$$
$$k_L = 3.038 \times 10^{-1}$$
$$N_o/A_o = 7.503 \times 10^{-5}$$
$$nF(\rho/M)A_o = 2.012 \times 10^{2}$$

It would be possible to fit experimental current-time transients to
each model (conical, hemispherical, cylindrical or progressive) with
the best fit giving some indication of the crystal growth geometry
and type of nucleation.

It would also be possible to perform fits for the same system at
a range of potentials and obtain the potential dependence of the rate
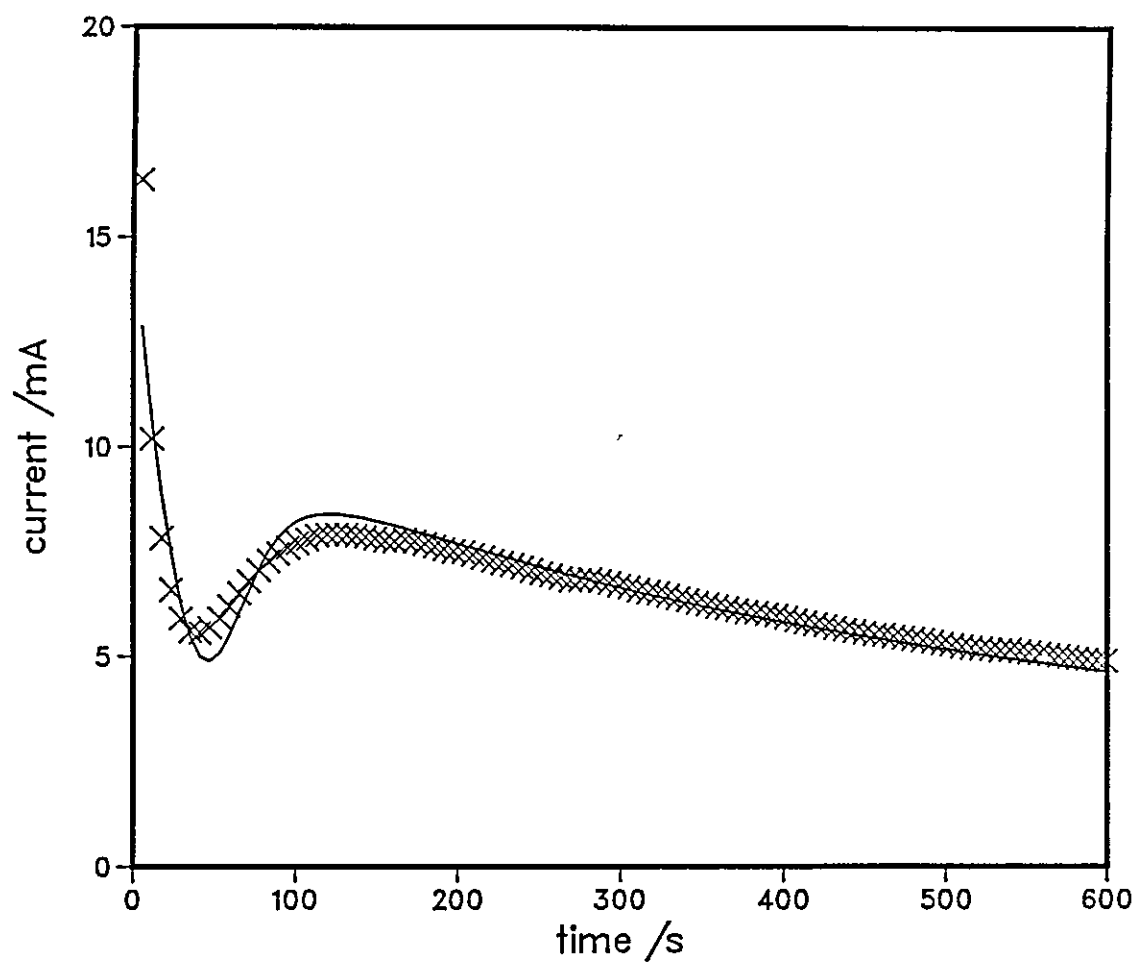constants and other parameters.

This may give useful information and provide further validation
for the model used.
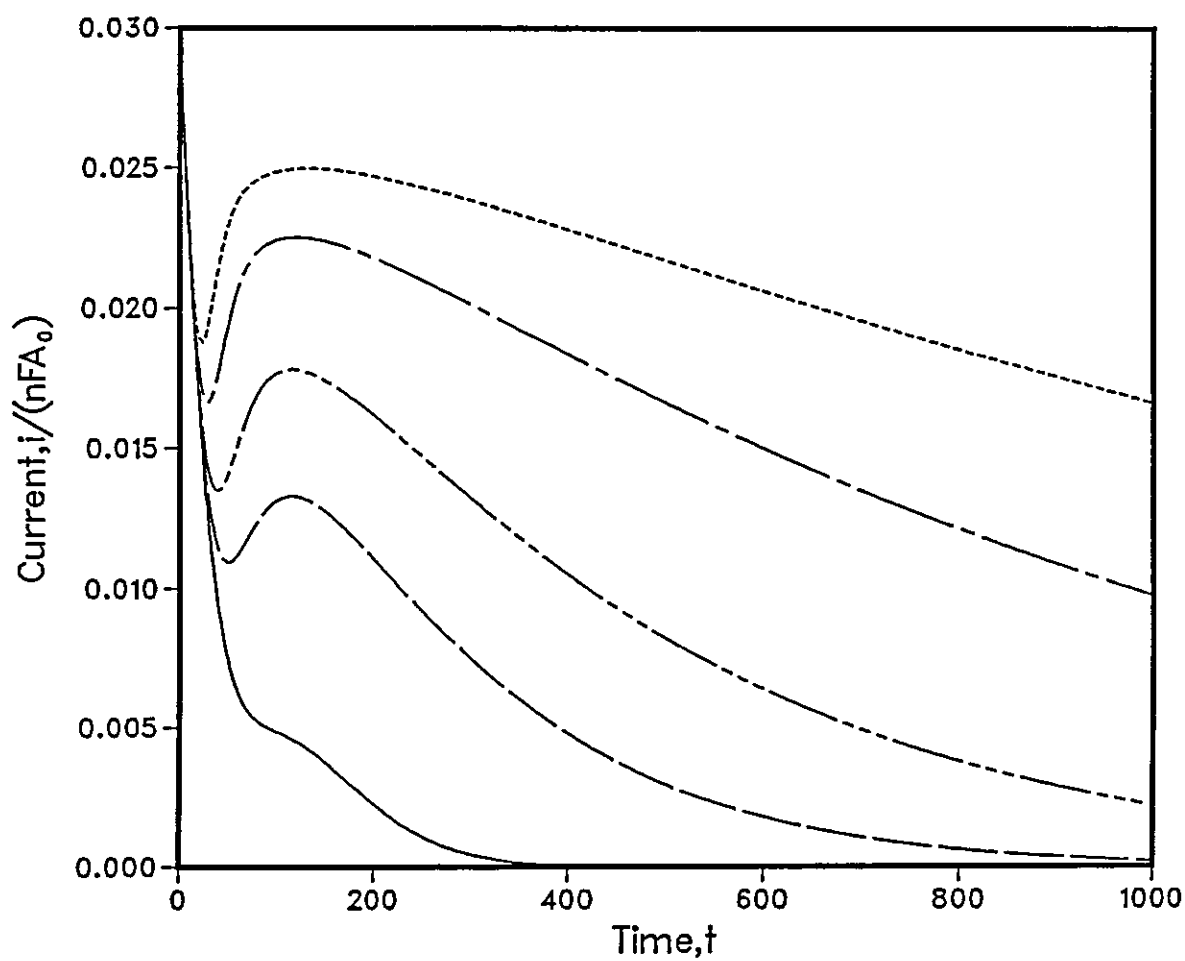
H=1.0

H=5.0

H=10.0

H=25.0

H=50.0

Fig 9.4.7   Fit to Experimental Data
Model is Instantaneous Nucleation of Cones
$k_tM/\rho=7.523E-02,k_b=3.050E-02,k_t=3.038E-01$
$\pi N_o/A_o=2.357E-04,nFA_o\rho/M=2.012E+02$

$\times$ Experimental data

Computed Fit

9.4.6 Conclusion

A kinetic model for crystal growth leading to passivation has been formulated which predicts an initial falling transient and a slow 'tail-off' at long times, which is frequenctly observed in experiment.

It is forcing the growth to proceed in a fixed geometry that is responsible for the long 'tail-off'.

It was also demonstrated that it is possible to fit this model to experimental data, extracting values for the parameters.

Further work is planned to obtain fits at a range of potentials and determine the potential dependence of the parameters.

CHAPTER X

A MACROHOMOGENEOUS MODEL FOR THE POROUS CARBON ELECTRODE

10.1 Introduction

The importance of various porous electrodes to the battery industry has stimulated much research into modelling their structure and discharge. De Levie [35] reviews progress in this field up until 1966.

There are three basic conceptual approaches to modelling a porous electrode. The first involves modelling the pores as cylinders perpendicular to the surface. Allowance can be made for the distribution of pore sizes, but not for connectivity between the pores. A thorough treatment of this model has been given by Winsel [99].

A second approach is to represent the pores as equivalent electrical circuits in a network corresponding to the whole porous structure; this model was suggested by Euler et al [100, 101].

The third approach is the macrohomogeneous model introduced by Newman and Tobias [102]. This model assumes the structure of the porous matrix, concentrations of species and deposition of material therein is uniform in a plane parallel to the electrolyte-electrode surface interface. This reduces the problem to essentially one dimension, perpendicular to the electrode surface.

Alkire, Grens and Tobias [103] modified this model to one in which the structure of the matrix changed during the discharge. Since this time much further progress has been made [104-110].

In this chapter two variations of this model will be used to derive data for potentiostatic and galvanostatic discharges.

10.2 Formulation of the model

A number of simplifying assumptions must first be made in order to facilitate the analysis.

(1) The material of the porous matrix has a much higher conductivity than the electrolyte.

(2) The matrix is infinitely connected in three dimensions so the conductivity of the matrix does not vary with discharge or depth into the electrode.

(3) The mass transport processes of the electrolyte solution within the matrix can be adequately described by dilute solution theory and diffusion is the predominant process.

(4) Double layer effects are ignored, i.e. the time constant for the charging of the double layer is small compared to the time intervals involved.

(5) The concentrations of species in the electrolyte at the surface of the electrode are equal to those in the bulk solution.

Equations describing the reation within the electrode and transport through it are now defined.

x is the distance into the electrode, x = 0 is the electrode surface.

c(x,t) is the concentration of a species at a distance x from the surface after time t.

a(x,t) is the available area for reaction in an element dx.

When a(x,t) = 0, the matrix is fully utilized in this plane distance x from the surface.

The reaction at a point x in the electrode follows the rate equation:

$$(i(x,t)/nF) = \partial c(x,t)/\partial t = -k\, a(x,t)\, c(x,t) \qquad (10.2.1)$$

where i is the current,
   n is the number of electrons in the reaction,
   F is the Faraday constant,
   k is a potential dependent rate constant.

Diffusion through the matrix is given by Fick's 2nd Law.

$$\partial c(x,t)/\partial t = D\, \partial^2 c(x,t)/\partial x^2 \qquad (10.2.2)$$

where D is the diffusion coefficient. So the equation describing the total process is:

$$(i(x,t)/nF) = \partial c(x,t)/\partial t = D\partial^2 c(x,t)/\partial x^2 - k\, a(x,t)c(x,t)$$

$$(10.2.3)$$

and $a(x,t)$ is assumed to be given by the following equation:

$$a(x,t) = a_0 - \int_0^t \rho k a(x,t)c(x,t)dt \qquad (10.2.4)$$

where ρ is density factor such that the maximum value of the integral is never greater than a_0.

It is equations (10.2.3) and (10.2.4) which must be solved to give the desired results.

The most direct way is to replace the derivatives by finite difference expressions. This is achieved by dividing the electrode depth into m equal increments of length Δx, and time into n equal increments Δt so

$$x = m\Delta x \qquad \text{and} \qquad (10.2.5)$$

$$t = n\Delta t \qquad \text{also} \qquad (10.2.6)$$

$$c(m\Delta x, n\Delta t) = C(m,n) \quad \text{so} \qquad (10.2.7)$$

$$(\partial c/\partial t) \simeq (1/\Delta t)[C(m,n + 1) - C(m,n)] \quad \text{and} \qquad (10.2.8)$$

$$(\partial^2 c/\partial x^2) \simeq (1/(\Delta x)^2)\, [C(m + 1,n) - 2C(m,n) + C(m - 1,n)] \qquad (10.2.9)$$

Equations (10.2.3) and (10.2.4) are thus converted to finite difference equations, so if values of $C(m,n)$ are known for all m i.e. all the points distance $m\Delta x$ down the electrode for time $n\Delta t$, they can be found for a time $(n + 1)\Delta t$.

In principle, as the initial conditions are assumed the concentrations can be found as a function of x and t.

The current as a function of time will be given by:

$$i(t) = nF \int_{x=0}^{x_0} ka(x,t) \; c(x,t) \; dx \qquad (10.2.10)$$

where x_0 is the total depth of the electrode.

The utilization of the matrix as a function of x is given by

$$a(x,\infty)$$

Figure 10.1 shows the current as a function of time for various rate constants. Figure 10.2 shows the utilization as a function of electrode depth x for the same rate constants and the total charge passed is given in Table 10.1.

The solutions of differential equations, by the above method are often subject to instability, where errors grow exponentially with the number of time steps.

A stability analysis for the simple linear parabolic partial differential equation

$$(\partial c/\partial t) = \alpha(\partial^2 c/\partial x^2) \quad (\alpha = \text{constant} > 0) \qquad (10.2.11)$$

shows that the stability criterion for a solution using the above method is

$$(\alpha \Delta t/(\Delta z)^2) < 0.5 \qquad (10.2.12)$$

[111]. This means that small time steps must be used. This simple parabolic equation is not the same as the more complicated case here, but trials using different values of Δt and D show this stability criterion to be approximately valid.

This has the effect that for small values of k, the number of time steps for the current to tend to zero, must be increased, since Δt must stay at a low value.

For all values of k the number of time steps used was such that the ratio of the initial current to the final current was 100, this resulted in reasonable computational time, and little error in values of total charge passed and utilization of the electrode.

A computational problem arises at the end of the electrode. If M is the number of divisions for the electrode depth, so $x_0 = M\Delta x$, then a value of $C(M + 1,n)$ will be needed for the solution. As nothing can diffuse through the end the electrode $C(M,n)$ is made a 'mirror-point', such that

k=1.0 _____

k=0.1 ___ ___ .
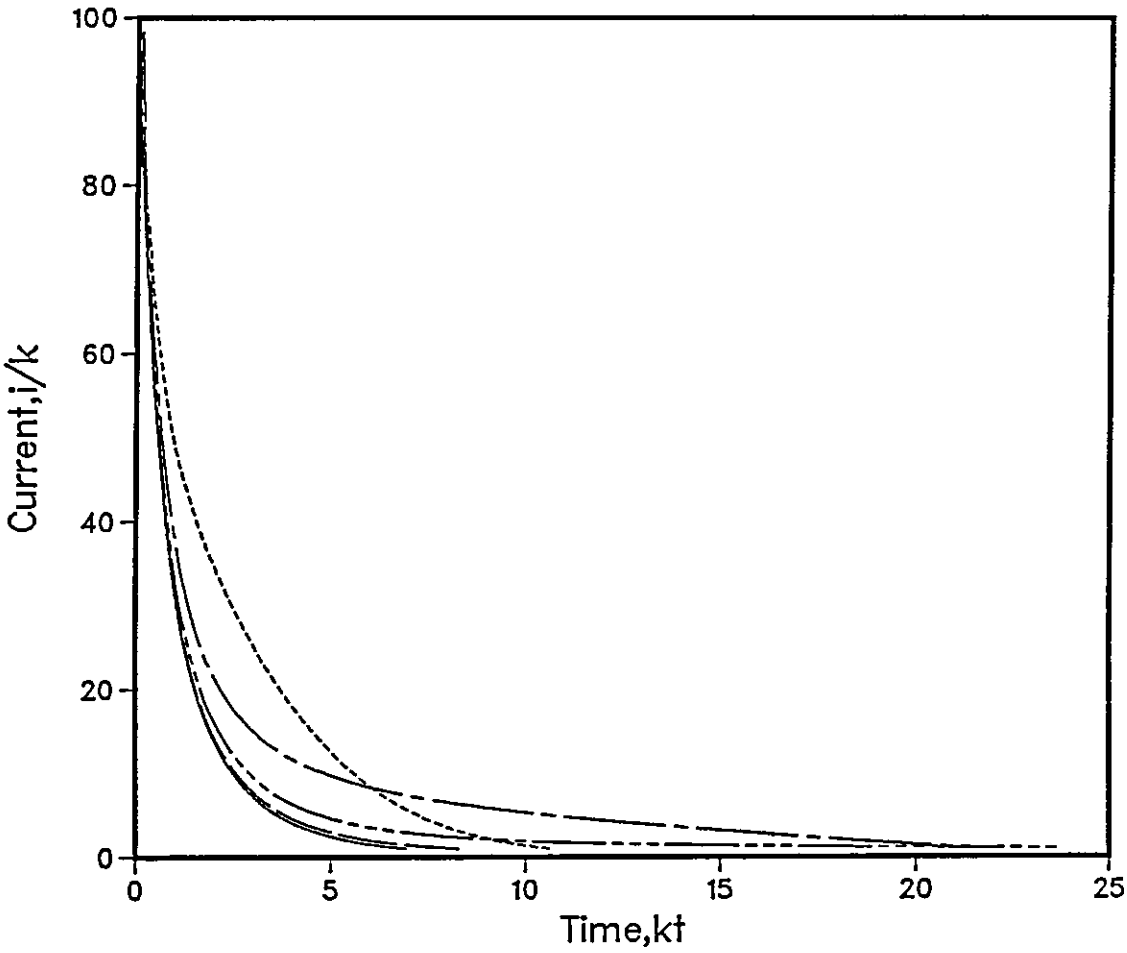
k=0.01 ___ _ _ ___

k=0.001 _ ___

k=0.0001 _ _ _ _ _ _ _

Fig. 10.2   Potentiostatic Discharge of the Simple Macrohomogeneous Model
utilization vs. depth into the electrode for various values of the rate constant,k
maximum utilization at any point depth, x, into the electrode is 2.0
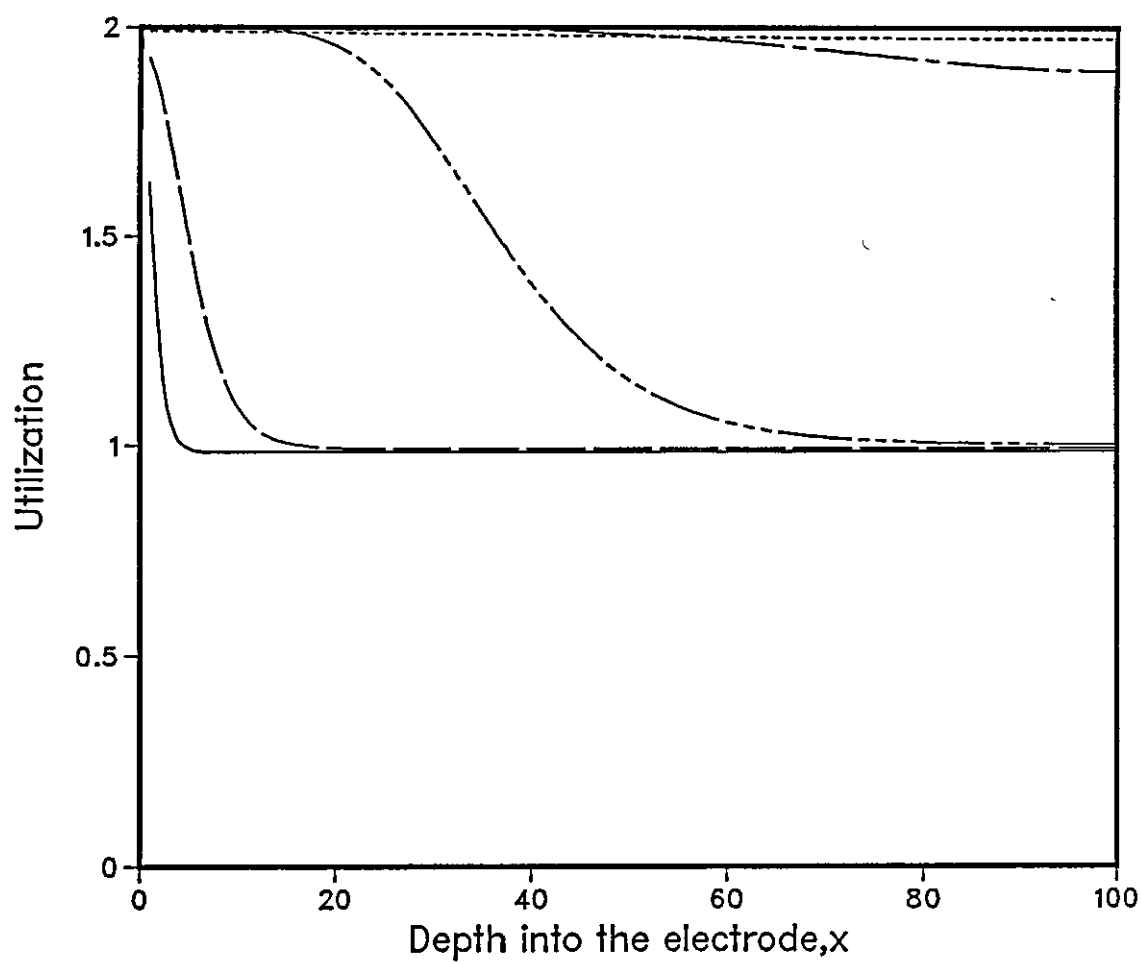
k=1.0
k=0.1
k=0.01
k=0.001
k=0.0001

TABLE 10.1

Total charge passed for various values of the rate constant, k.
Full utilization corresponds to a charge of 200.

k	Charge passed
1.0	99.47
0.1	104.22
0.01	137.66
0.001	196.56
0.0001	197.99

$$C(M - 1,n) = C(M + 1,n) \tag{10.2.13}$$

The boundary conditions used were at $t = 0$

$$c(x,0) = c_o \tag{10.2.14}$$

and at $x = 0$

$$c(0,t) = c_o \tag{10.2.15}$$

where c_o is the bulk concentration. The values for various parameters were chosen arbitrarily (but subject to equation (10.2.12) and are as follows:

$$\Delta x = 1$$
$$\Delta t = 1$$
$$x_o = 100$$
$$D = 0.5$$
$$a_o = 1.0$$
$$c_o = 1.0$$
$$\rho = 0.5$$

So for a point distance x into the electrode the maximum possible utilization is 2.0, and the maximum possible capacity of the electrode is 200.0.
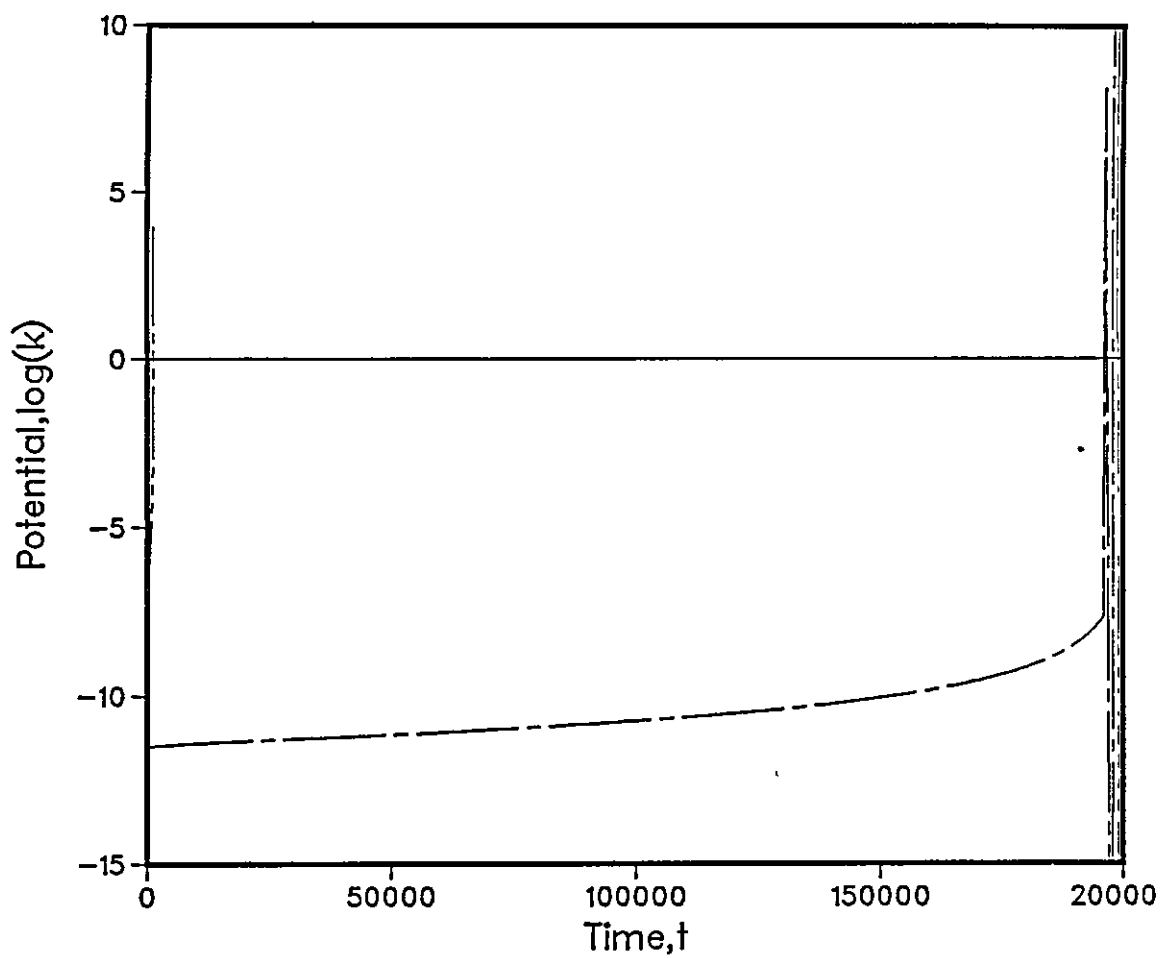
This model is now extended to discharge galvanostatically, which is more applicable to battery situations.

A value of the rate constant k is computed for each time time interval, which will give the same value for the current. This is repeated until the electrode is unable to sustain this current as it becomes fully utilized.

If k has the normal potential dependence a plot of log k vs t should give the shape of a potential-time plot. This is shown for various currents in figure 10.3.

Figure 10.4 shows the utilization as a function of depth at these currents, and Table 10.2 shows the total charge passed.

Fig. 10 3a Galvanostatic Discharge of the Simple Maorohomogeneous Model
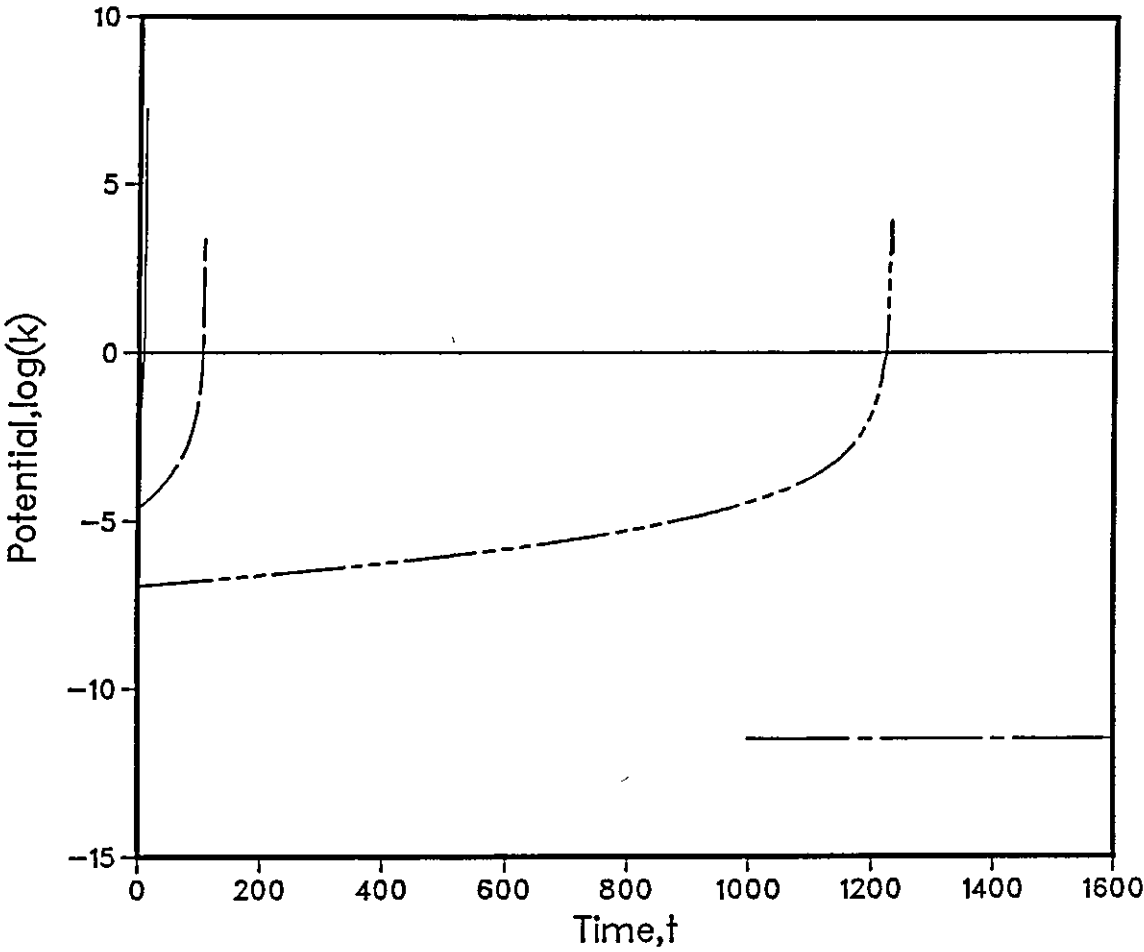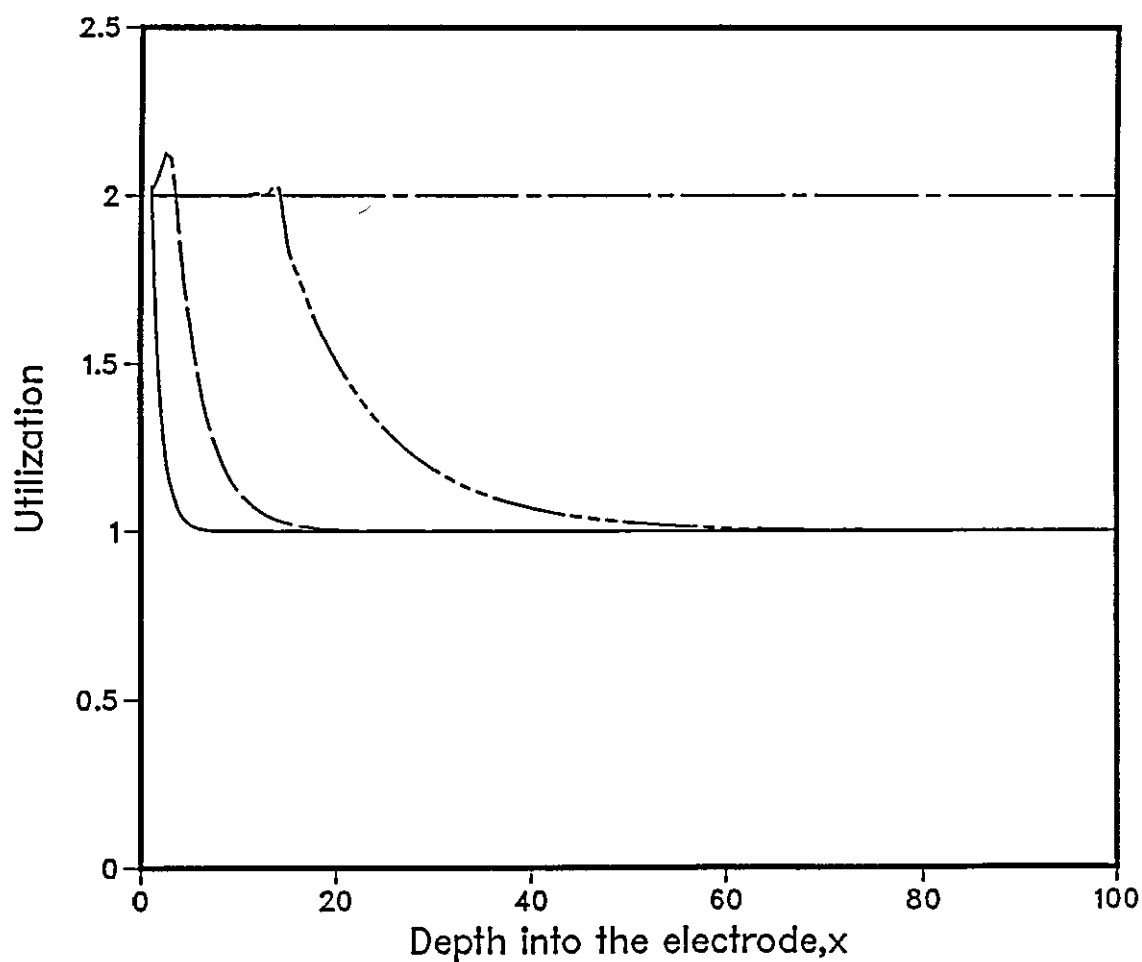log(k) (potential) vs. Time for various currents,i

i=10.0 ──────

i=1.0 ─── ─── ·

i=0.1 ─ ─ ───

i=0.01 ─── ───

Fig. 10.4   Galvanostatic Discharge of the Simple Macrohomogeneous Model
utilization vs. depth into the electrode for various values of the current,I
maximum utilization at any point depth, x, into the electrode is 2 0

TABLE 10.2

Total charge passed for various values of the current, i.
Full utilization corresponds to a charge of 200.

i	Charge passed
10.0	101.65
1.0	106.25
0.1	122.84
0.01	197.53
0.001	199.98

10.3 Extension of the Model

The porous structure of the electrode is now assumed to consist of randomly packed spheres on the surface of which instantaneous two dimensional nucleation and growth occurs.

Figure 10.5 shows S.E.M. photographs of carbon cathode material of various carbon types, taken from a Li/SO_2 cell production line.

As the growth of the insulating deposit on the surface is two dimensional the growth will be in the form of a spherical cap on a spherical surface.

It is therefore necessary to derive functions for the coverage and perimeter for a number of these caps overlapping on the surface.

Considering a single cap:

The probability that a given point is covered assuming all locations are equally likely

$$P(\text{a point is covered}) = S_{cap}/S \qquad (10.3.1)$$

and

$$P(\text{a point is not covered}) = 1 - S_{cap}/S \qquad (10.3.2)$$

where S_{cap} = area of the cap,

$\quad S$ = total surface area of the sphere,

and $\quad P(\ )$ is the probability of a given event,

$$S_{cap} = 2\pi Ra \qquad (10.3.3)$$

and

$$a = R(1 - \cos \phi) \qquad (10.3.4)$$

where R, a and ϕ are defined in figure 10.6.

$$\text{So} \quad S_{cap} = 2\pi R^2 (1 - \cos \phi) \qquad (10.3.5)$$

and

$$S = 4\pi R^2 \qquad (10.3.6)$$

So $\quad P(\text{a point not covered by one cap}) = 1 - (1 - \cos \phi)/2 \qquad (10.3.7)$

The probability that a point is not covered by n caps of the same size at random locations on the surface

Figure 10.5a S.E.M. micrograph of carbon cathode material
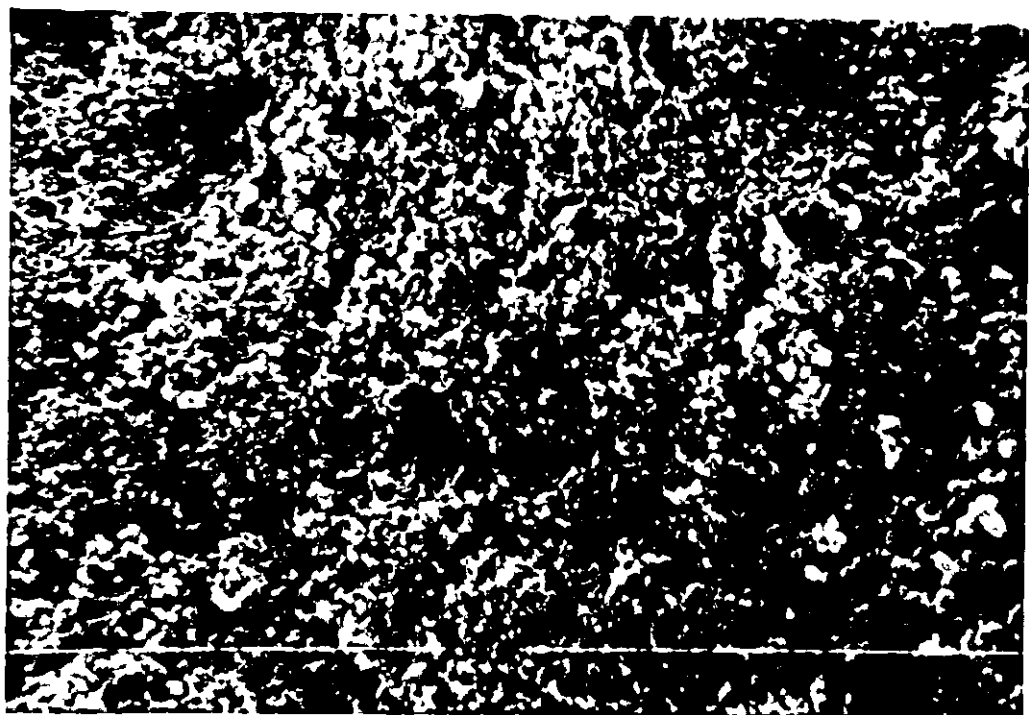(Canadian carbon type). Magnification x 3,750.

Figure 10.5b As figure 10.5a, but with magnification x 7,500.
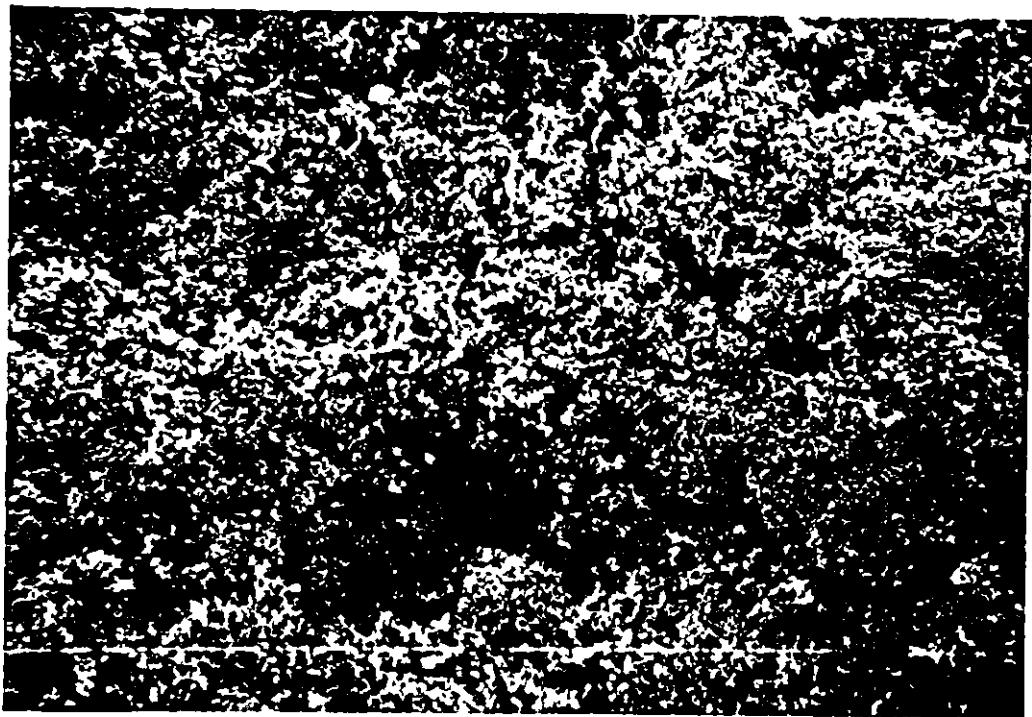
Figure 10.5c S.E.M. micrograph of carbon cathode material
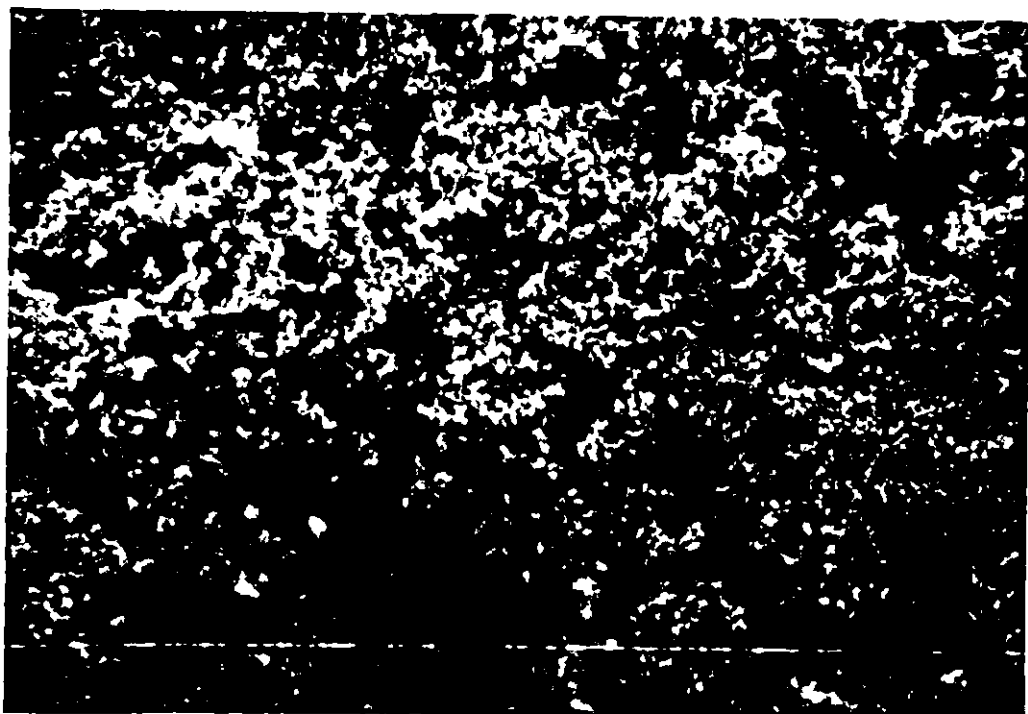(American carbon type). Magnification x 3,500.

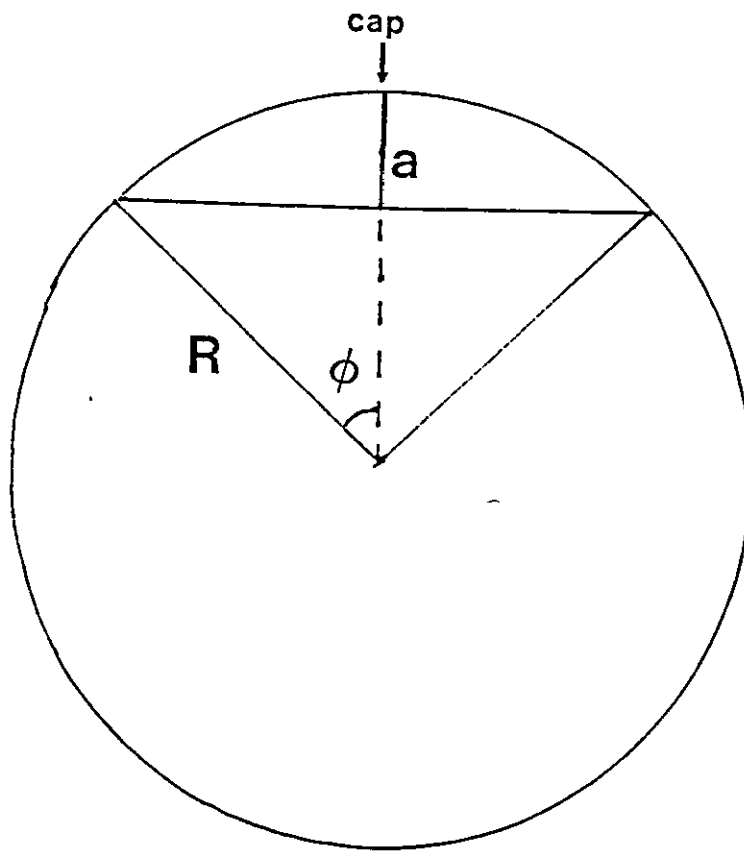Figure 10.5d As figure 10.5c, but with magnification x 7,500.

Figure 10.6   Diagram showing a spherical cap on the surface of
a sphere.

$$P(\text{a point not covered by n caps}) = \{1 - (1-\cos \phi)/2\}^n \quad (10.3.8)$$

$$P(\text{a point is covered}) = 1 - \{1 - (1 - \cos \phi)/2\}^n \quad (10.3.9)$$

. All points on a sphere are equivalent so the expected fractional coverage, η, by n caps is given by

$$\eta = 1 - \{1 - (1 - \cos \phi)/2\}^n \quad (10.3.10)$$

If it is now assumed that the number of nuclei on the surface of the sphere is given by a poisson distribution, then the probability of having n nuclei is

$$P(\text{n nuclei}) = \mu^n e^{-\mu}/n! \quad (10.3.11)$$

where μ is the mean number of nuclei.

So the expected coverage for any number of nuclei is given by

$$\eta = 1 - \sum_{n=0}^{\infty} \frac{\mu^n}{n!} e^{-\mu} \{1 - (1 - \cos \phi)/2\}^n \quad (10.3.12)$$

$$\eta = 1 - \sum_{n=0}^{\infty} \{(1+\cos \phi)\mu/2\}^n \frac{\exp(-(1+\cos \phi)\mu/2)}{n!} \exp(-(1-\cos \phi)\mu/2) \quad (10.3.13)$$

$$\eta = 1 - \exp(-(1-\cos \phi)\mu/2) \sum_{n=0}^{\infty} \{(1+\cos \phi)\mu/2\}^n \exp(-(1+\cos \phi)\mu/2)/n! \quad (10.3.14)$$

$$\eta = 1 - \exp(-(1-\cos \phi)\mu/2) \quad (10.3.15)$$

The perimeter, p, will be given by

$$p = \frac{\partial \eta}{R \partial \phi} \cdot 4\pi R^2 \quad (10.3.16)$$

$$\therefore \quad p = 4\pi R \frac{\partial}{\partial \phi} (1 - \exp(-(1-\cos \phi)\mu/2)) \quad (10.3.17)$$

$$p = -4\pi R \exp(-(1 - \cos \phi)\mu/2)(-\sin \phi \cdot \mu/2) \quad (10.3.18)$$

$$p = 2\pi R \mu \sin \phi \exp(-(1- \cos \phi)\mu/2) \quad (10.3.19)$$

The rate of reaction in a given plane distance x into the electrode is given by

$$k \; c \; (x) \; p \; (x)$$

where c(x) is the concentration and p(x) is the mean perimeter at this depth into the electrode, k is the potential dependent rate constant.

Thus the current as a function of time for the potentiostatic case and the potential as a function of time for the galvanostatic case can be derived as before. For the potentiostatic case the calculation of the current is allowed to continue until it has fallen to 1% of its maximum value and for the galvanostatic case the calculation is continued until constant current can not be maintained. This enables the total utilization as a function of depth to be calculated.

Figure 10.7 shows some potentiostatic plots and figure 10.8 shows the corresponding utilization-depth profiles. Figures 10.9 and 10.10 show the same for galvanostatic discharge.

Tables 10.3 and 10.4 show the total charged passed for each case.

10.4 Conclusions

Looking first at the potentiostatic plots, figures 10.1 and 10.7, it can be seen that in the simple model a falling transient results whereas with the model incorporating nucleation and growth the current starts at zero reaches a maximum and then returns to zero. As μ is increased, however, the behaviour does approach that of the simple model.

The utilization-depth profiles for the potentiostatic discharges, figures 10.2 and 10.8, show that as the value of k is increased the total utilization becomes less with only the front end of the electrode approaching full utilization.

The utilization that corresponds to just the amount of active species already present in the pores of the matrix at the beginning of the discharge is 100. This shows that for high values of k, very little has diffused into the electrode, and the diffusion limited current is negligible compared with the initial current or the maximum current in the nucleation and growth model, and so the discharge was stopped before complete utilization. The decision to stop the discharge when the current or potential falls below a certain value may seen arbitrary, but similar criteria are used in battery testing.

Fig. 10.7   Potentiostatic Discharge of the Randomly Packed Sphere Macrohomogeneous Model
Mean number of nuclei,10⁰
Current vs. Time rescaled by the rate constant k
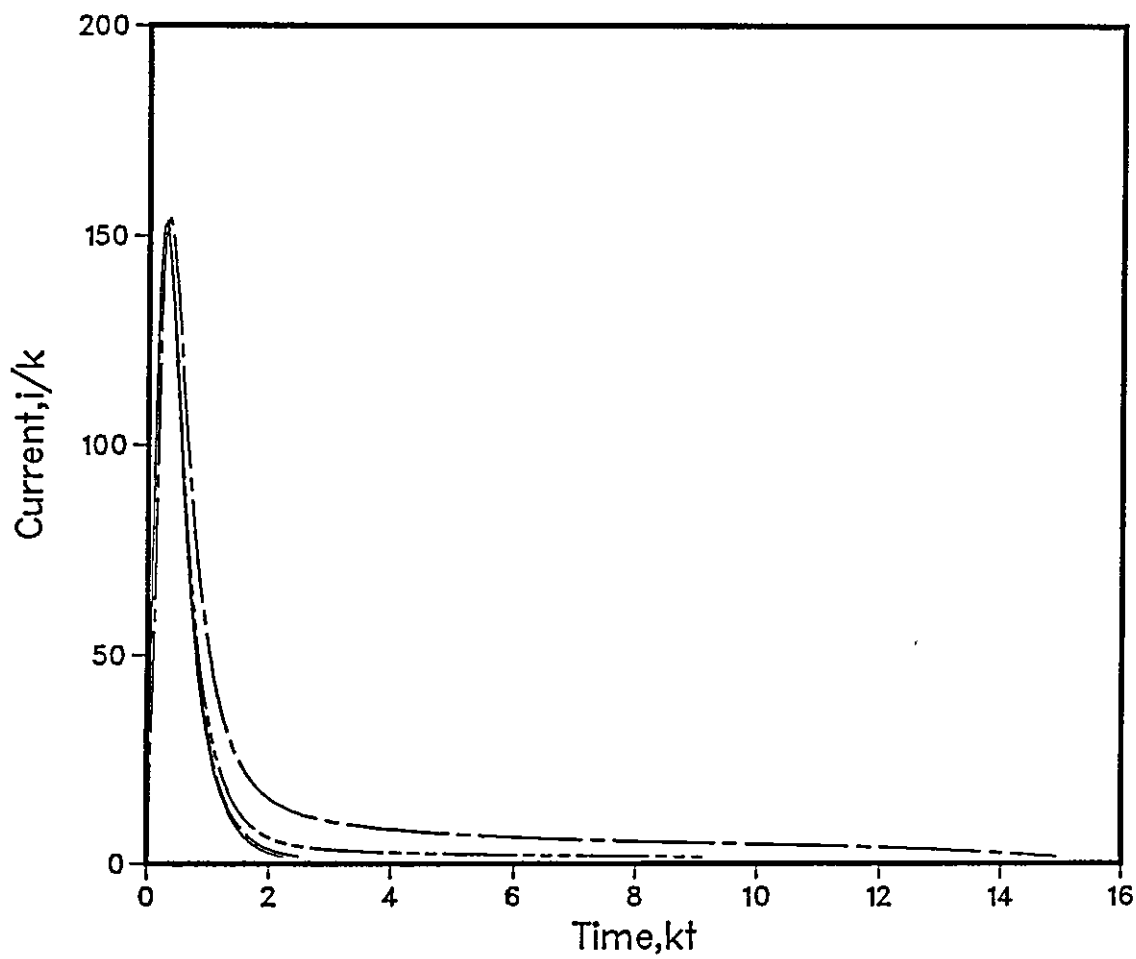
k=1.0 ————

k=0.1 —— —— ·

k=0.01 — — ——

k=0.001 ————

Fig. 10.8 Potentiostatic Discharge of the Randomly Packed Sphere Macrohomogeneous Model
Mean number of nuclei,10.0
utilization vs. depth into the electrode for various values of the current,]
maximum utilization at any point depth, x, into the electrode is 2.0
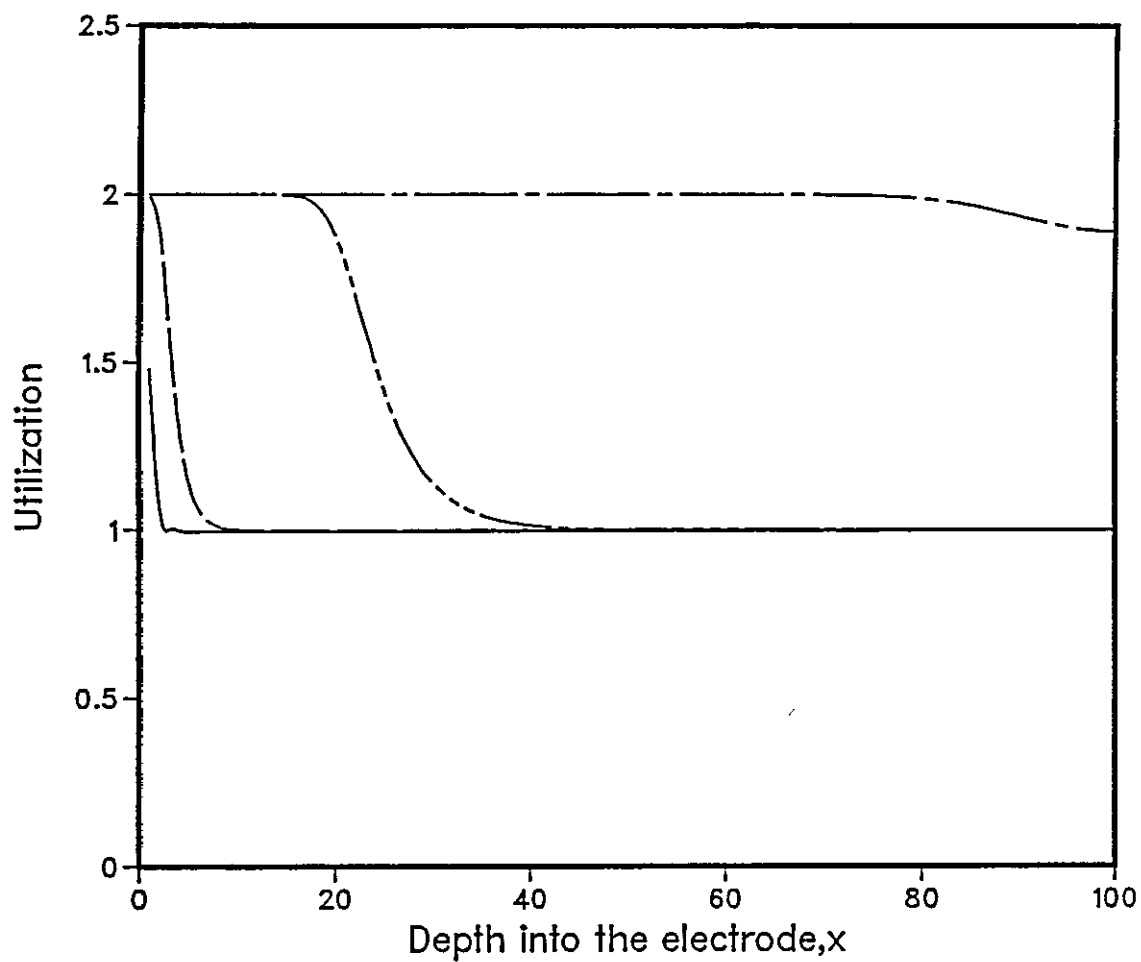
TABLE 10.3

Total charge passed for various values of the rate constant, k, and mean number of nuclei, μ. Full utilization corresponds to a charge of 200.

k	μ	Charge passed
1.0	1	99.9
0.1	1	102.3
0.01	1	114.7
0.001	1	126.3
1.0	10	100.1
0.1	10	102.8
0.01	10	124.5
0.001	10	198.6
1.0	100	99.7
0.1	100	101.0
0.01	100	107.3
0.001	100	178.2
0.0001	100	199.5
1.0	1000	99.5
0.1	1000	100.1
0.01	1000	102.1
0.001	1000	124.3
0.0001	1000	198.8

Fig. 10 9a   Galvanostatic Discharge of the Randomly Packed Sphere Macrohomogeneous Model
Mean number of nuclei 10.0
log(k) (potential) vs. Time

Fig. 10.9b   Galvanostatic Discharge of the Randomly Packed Sphere Macrohomogeneous Model
Mean number of nuclei 10.0
log(k) (potential) vs. Time

i=10.0

i=1.0

i=0.1

i=0.01

Fig. 10 10   Galvanostatic Discharge of the Randomly Packed Sphere Macrohomogeneous Model
Mean number of nuclei,10 0
utilization vs. depth into the electrode for various values of the current,i
maximum utilization at any point depth, x, into the electrode is 2.0
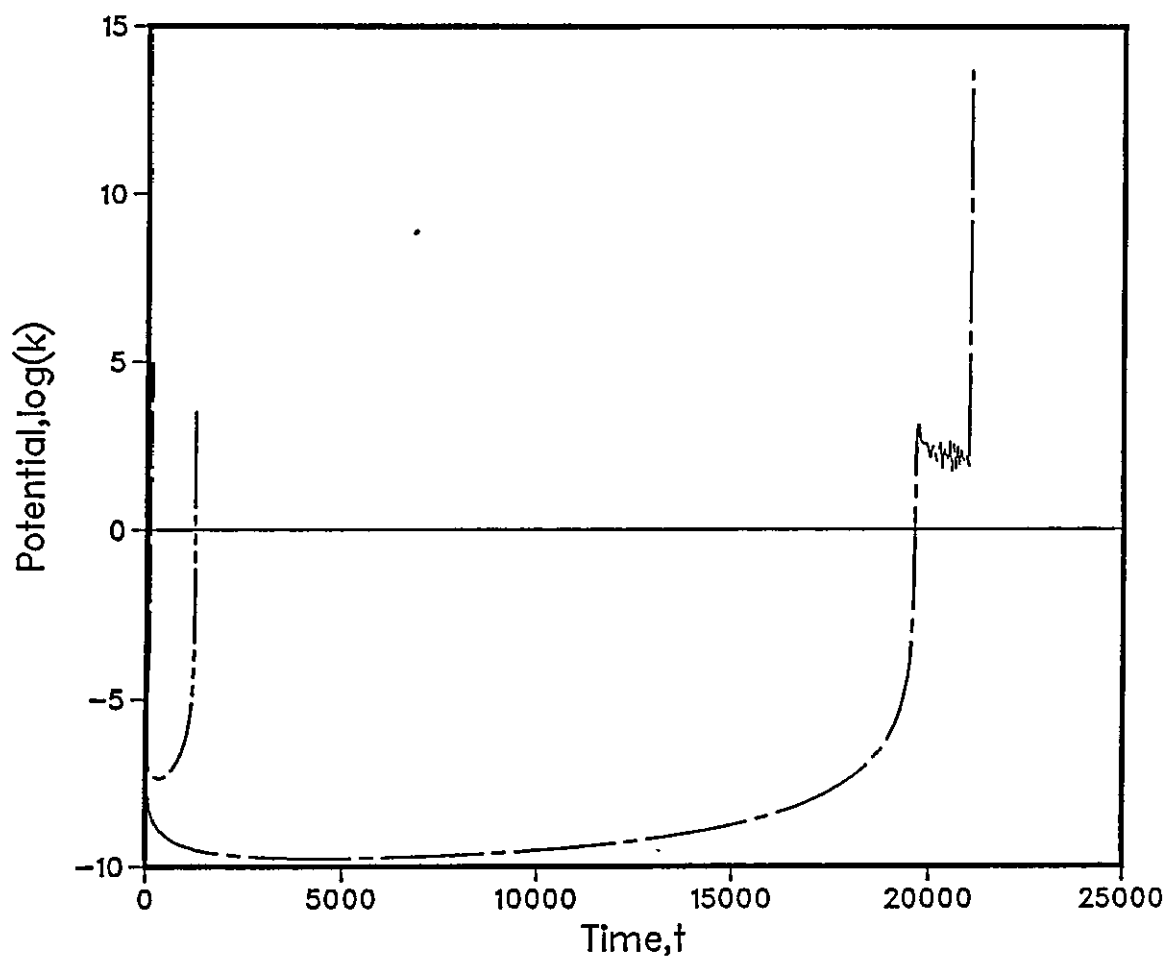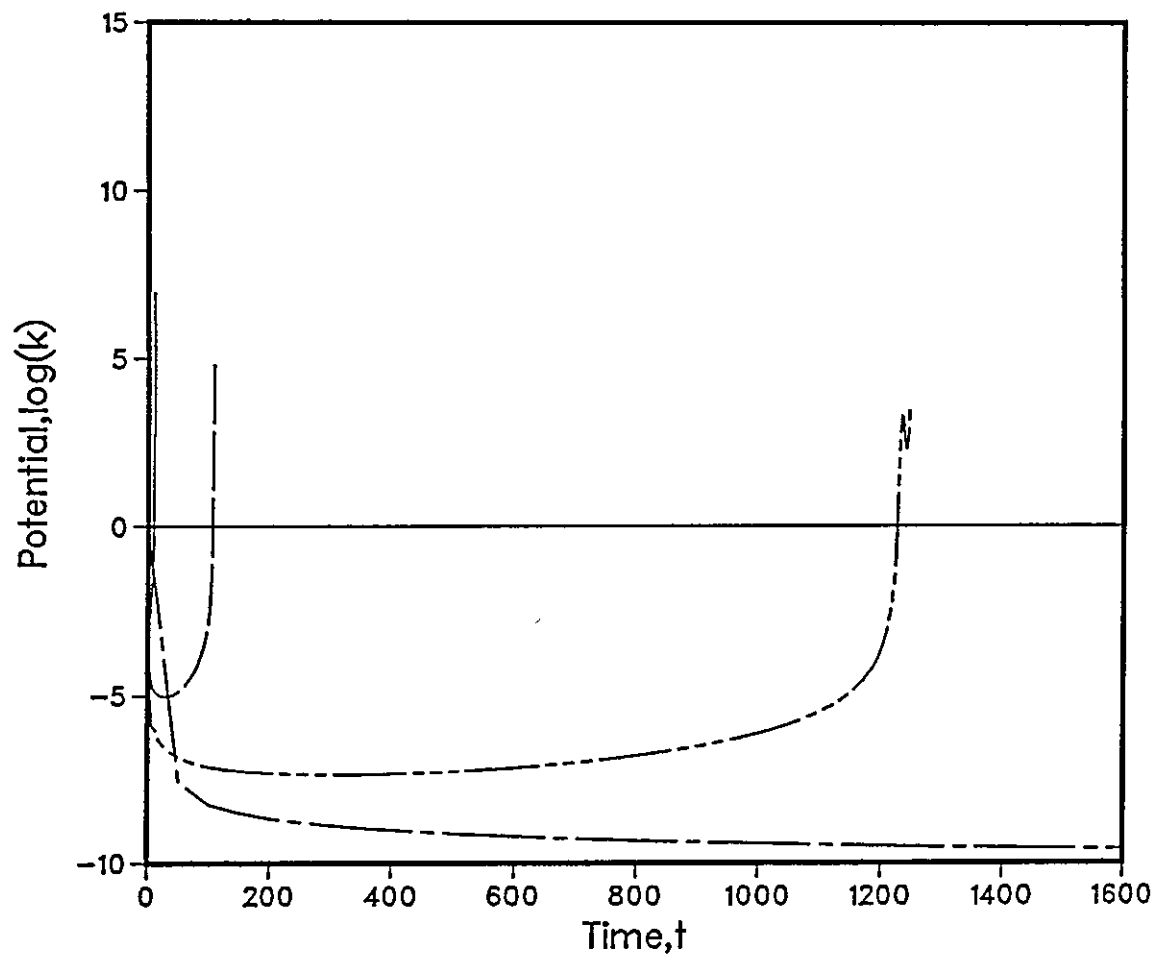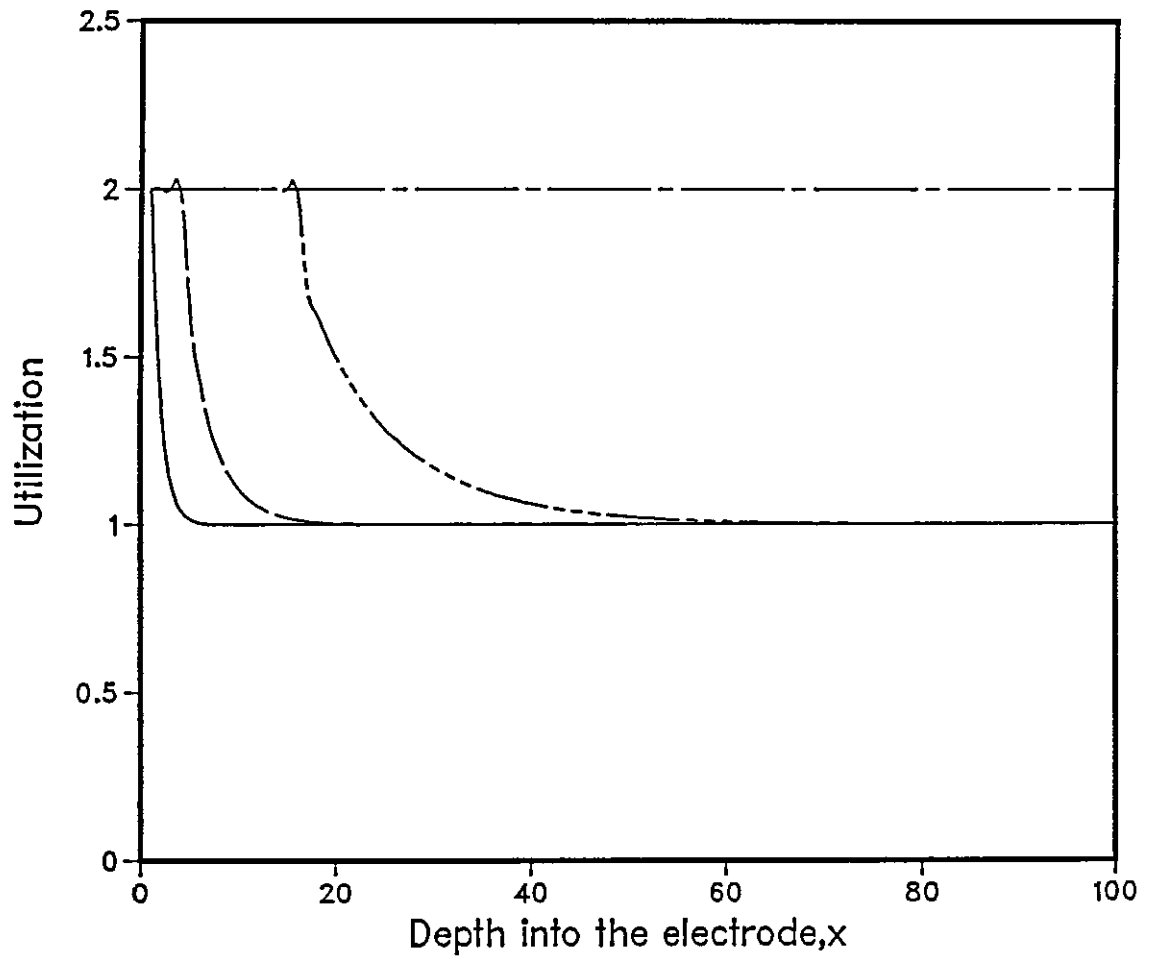
i=10.0 _____

i=1.0 __ __ __ .

i=0.1 ___ ___

i=0.01 ___ ___

TABLE 10.4

Total charge passed for various values of the current, i, and mean
number of nuclei, μ.   Full utilization corresponds to a charge of 200.

i	μ	Charge passed
10.0	1	100.8
1.0	1	102.7
0.1	1	109.7
0.01	1	126.4
10.0	10	101.6
1.0	10	106.1
0.1	10	122.9
0.01	10	199.99
10.0	100	101.6
1.0	100	106.1
0.1	100	118.2
0.01	100	199.99
10.0	1000	101.6
1.0	1000	106.1
0.1	1000	125.3
0.01	1000	199.99

Figures 10.3 and 10.9 show potential time plots for galvanostatic discharges.

The simple model, fig. 10.3, shows the potential stays fairly constant and then falls rapidly at the end of the discharge. The nucleation and growth model, figure 10.9, shows this behaviour and in addition a 'voltage delay' at the start of the discharge, because the reaction is limited by the small area of electrode surface available at the beginning of nucleation.

The utilization-depth profiles, figures 10.4 and 10.10 show similar trends as before.

Finally, if realistic values for the parameters could be inserted, the models would be useful in determining the effectiveness of the porous electrode at various potentials or currents during discharge. Or given easily measureable data like a current-time or potential-time plot an unknown parameter such as a_o, which is related to the effective porosity, could be found. This would enable effective porosities of different carbon types used in the cathode material to be evaluated from their respective current-time or potential time plots.

REFERENCES

[1]   J.P. Gabano, Lithium Batteries, Academic Press (1983).

[2]   W.F. Meyers, B. Bell and J.W. Simmons (1969) U.S. Pat. 3,
       423, 242.

[3]   D.L. Maricle and J.P. Mohns (1971) U.S. Pat. 3, 567, 515.

[4]   A.N. Dey (1977) Thin Solid Films, 43, 131.

[5]   M.J. Schaer and R.S. Meredith (1964) NOCL Report 597, Sixth
       Symposium on Ammonia Batteries.

[6] R.Lucas (1953) Organic Chemistry, p. 393, American Book Co.,
       New York.

[7]   A.N. Dey and R.W. Holmes (1979) J. Electrochem. Soc.,
       126, 10, 1647.

[8]   W. Behne, G. Jander and H. Hecht (1952) Z. Anorg. Allegen.
       Chem., 269, 249.

[9]   P. Bro, H. Y. Kang, C. Schlaikjer and H. Taylor (1975)
       Proceedings 10th IECEC, 432.

[10]   R. Bonnaterre and G. Cauquis (1971) J. Electroanal. Chem. &
       Interfacial Electrochem., 32, 215.

[11]   H. Helmholtz, Weid. Ann., 7 (1879) 377.

[12]   A. Gouy, J. Phys., Chem. 9 (1910) 457.

[13]   D. L. Chapman, Phil. Mag., 25 (1913) 475.

[14]   O. Stern, Z. Electrochem., 30 (1924) 508.

[15]   D.C. Grahame, Chem. Rev., 41 (1947) 441.

[16]   M.A.V. Devanathan, J. O'M Bockris and K. Müller, Proc.
       Roy. Soc., London, A274 (1963) 55.

[17]   A.N. Frumkin, Z. Physik. Chem., 164A (1933)121.

[18]   I.L. Cooper and J.A. Harrison, J. Electroanal. Chem.,
       66 (1975) 85.

[19]   Idem, Electrochim. Acta, 22 (1977) 519.

[20]   Idem, ibid., 22 (1977) 1361

[21]   Idem, ibid., 22 (1977) 1365

[22]   Idem, ibid., 23 (1978) 545

[23]   R. Parsons, in "Advances in Electrochemistry and Electrochemical
       Engineering, Volume 1", edited by P. Delahay, John Wiley
       Interscience, London, 1961.

[24]   H. H. Bauer, J. Eelctroanal. Chem., 16 (1968) 419.

[25]   W.A. Caspari, Z. Physik. Chem., 30 (1899) 89.

[26] T. Erdey-Gruz and M. Volmer, Z. Physik. Chem., 105A (1930) 203.

[27] W.A. Ledger and A.C. Riddiford, Nature, 194 4835, 1233 (1962).

[28] W. Nernst, Zeit. Phys. Chem., 47, 52 (1904).

[29] J.E.B. Randles, Discuss Faraday Soc., 1 (1947) 11.

[30] E. Warburg, Weid. Ann., 67, 493 (1899).

[31] F. Kruger, Z. Physik. Chem., 45, 1 (1903).

[32] J.H. Sluyters, Rec. Trav. Chim., 79 (1960) 1092.

[33] M. Sluyters-Rehbach, Thesis, Utrecht, 1963.

[34] J. Llopis and F. Colon, in "Proceedings of the Eighth Meeting of the C.I.T.C.E.", 1950, Butterworths, London, 1958, p. 414.

[35] R. de Levie, "Advances in Electrochemistry and Electrochemical Engineering" Volume 6, (edited by P. Delahay and C.W. Tobias) Interscience, New York (1967) p. 329.

[36] M. Hughes, S.A.G.R. Karunathilaka, N.A. Hampson and T.J. Sinclair, J. Appl. Electrochem., 12 (1982) 537.

[37] M. Hughes, S.A.G.R. Karunathilaka, R.T. Barton and N.A. Hampson, J. Appl. Electrochem. - in press.

[38] N.A. Hampson and M.J. Willars, Surface Technology, 7 (1978) 247.

[39] S. Kelly, N.A. Hampson, S.A.G.R. Karunathilaka and R. Leek, Surface Technology, 13 (1981) 349.

[40] M. Sluyters-Rehbach and J.H. Sluyters, in (Electro analytical Chem., Volume 4, Edited by A.J. Bard), Dekker, New York, (1970) p. 1.

[41] S.A.G.R. Karunathilaka, N.A. Hampson, R. Leek and T.J. Sinclair, J. Appl. Electrochem., 10 (1980) 799.

[42] S.A.G.R. Karunathilaka, N.A. Hampson, R. Leek, T.J. Sinclair and T.P. Hass, J. Appl. Electrochem., 11 (1981) 573.

[43] S.A.G.R. Karunathilaka, R. Leek, N.A. Hampson, M. Hughes and T.J. Sinclair, J. Appl. Electrochem., 13 (1983) 351.

[44] M. Hughes, S.A.G.R. Karunathilaka, N.A. Hampson and T.J. Sinclair, J. Appl. Electrochem., 13 (1983) 217.

[45] S.A.G.R. Karunathilaka, N.A. Hampson, M. Hughes, W.G. Marshall, R. Leek and T.J. Sinclair, J. Appl. Electrochem., 13 (1983) 577.

[46] M. Hughes, R.T. Barton, S.A.G.R. Karunathilaka and N.A. Hampson, J. Appl. Electrochem. (submitted for publication).

[47] S.C. Creason, J.W. Hayes and D.E. Smith, J. Electroanal. Chem., 47 (1973) 9.

[48] R. de Levie, J.W. Thomas and K.M. Abbey, J. Electroanal. Chem., 62 (1975) 111.

[49] H.B.S. Alcazar, A.N. Fleming and J.A. Harrison, J. Electroanal. Chem., 87 (1978) 339.

[50] A.A. Pilla, J. Electrochem. Soc., 117 (1970) 467.

[51] H.P. Van Leeuwen, D.J. Kooijman, M. Sluyters-Rehbach and
      J.H. Sluyters, J. Electroanal. Chem., 23 (1969) 475.

[52] M. Ichise, Y. Nagayanagi and T. Kojima, J. Electroanal. Chem.,
      70 (1976) 245.

[53] J.W. Cooley and J.W. Tukey, Math. Comp., 19 (1965) 297.

[54] J.W. Cooley, P.A.W. Lewis, P.D. Welch, "The Fast Fourier
      Transform Algorithm and its Applications", IBM Research
      Paper RC-1743, (1967).

[55] S.A.G.R. Karunathilaka, M. Hughes, R.T. Barton and N.A. Hampson,
      J. Appl. Electrochem., 15 (1985) 251.

[56] V. Manev, A. Nassalevska and R. Moshtev, Journal of Power
      Sources, 6 (1981) 337-345.

[57] G.J. DiMasi, Proc. 27th Power Sources Symposium, pp. 75-77 (1976).

[58] U.S. Army Specification Mil-B 49430 (E.R.)

[59] D. Eyre, M.O.D. Lithium Battery Safety Symposium, 1982.

[60] G.J. DiMasi and J.A. Christopulos, 1978 Power Sources Symposium
      - Lithium Batteries Session.

[61] A.N. Dey, J. Electrochem. Soc., 127 (1980) 1886.

[62] U.R. Evans, "Corrosion and oxidation of metals", 1960,
      Chapter VII, p. 222 (London: Edward Arnold).

[63] S.D. James, J. Power Sources, 10 (1983) 105-107.

[64] S.D. James, Proc. Symp. Lithium Batteries, Vol. 83-4,
      Electrochem. Soc., Inc., Newark, N.J. 1983, p. 74.

[65] P. Zlatilova, Y. Geronov and R. Moshtev, J. Power Sources,
      13 (1984) 327-334.

[66] R. Landsberg and H. Bartelt, Z. Electrochem., 61 (1957) 1162.

[67] N.A. Hampson and M.J. Tarbox, J. Electrochem. Soc.,
      110 No. 2 (1963) 95-98.

[68] N.A. Hampson, M.J. Tarbox, J.T. Lilley and J.P.G. Farr,
      Electrochemical Technology, Volume 2, No. 11-12 (1964) 309-313.

[69] T. P. Dirkse and N.A. Hampson, Electrochim. Acta, 16 (1971)2049.

[70] Idem. ibid., 17 (1972) 387.

[71] M.B. Lui, G.M. Cook and N.P. Yao, J. Electrochem. Soc.,
      128 (1981) 1663.

[72] R. Landsberg and M. Hollnagel, Z. Electrochem., 58 (1954) 680.

[73] K.I. Vetter, Electrochemische Kinetik, Springer, Berlin, 1961.

[74] C.J. Bushrod, Ph.D. Thesis, Loughborough University of
      Technology, 1973.

[75] C.J. Bushrod and N.A. Hampson, Br. Corros. J., 1971, Vol. 6, 87.

[76] N.Y. Lyzlov and I.A. Aguf, Sov. Electrochem., 17 (1981) 345.

[77] H.J.S. Sand, Phil. Mag., 1901, 1, 45.

[78] H. Eisenberg, H.F. Bauman and D.M. Brettner, J. Electrochem. Soc., 1961, 108, 909.

[79] N.A. Hampson and N.E. Spencer, Br. Corrosion J., 1968, 3, 1.

[80] A. Leef, A. Gilmour, Journal of Applied Electrochemistry, 9 (1979) 663.

[81] S.D. James, P.H. Smith, W.P. Kilroy, J. Electrochem. Soc., 130, No. 10, 1983, p. 2037.

[82] Kossel, Nachr. Ges. Wiss. Göttingen, 1927, 135.

[83] Stranski, Z. Physik. Chem., Leipzig, 136 (1928) 259.

[84] Erdey-Gruz and Volmer, Z. Physik. Chem., Leipzig, A 150 (1930) 203.

[85] M. Fleischmann and H.R. Thirsk, Advances in Electrochemistry, Volume III, edited by P. Delahay, Interscience Publishers Inc., New York, 1963.

[86] M. Avrami, J. Chem. Phys., 7 (1939) 1103; 8 (1940) 212; 9 (1941) 177.

[87] A. Kolmogorov, Izv. Acad. Nauk. SSSR, ser. math., 3, 355 (1937).

[88] U. Evans, Trans. Faraday Soc., 41, 365 (1945).

[89] R.D. Armstrong, M. Fleischmann and H.R. Thirsk, J. Electroanal. Chem., 11 (1966) 208.

[90] U.R. Evans, "The Corrosion and Oxidation of Metals", Edward-Arnold, 1960.

[91] W.J. Müller, Trans. Faraday Soc., 27 (1931) 737.

[92] E. Bosco and S.K. Rangarajan, J. Electroanal. Chem., 134 (1982) 225.

[93] R.G. Barradas, S. Fletcher and J.D. Porter, J. Electroanal. Chem., 80 (1977) 295.

[94] R.G. Barradas, F.C. Benson and S. Fletcher, J. Electroanal. Chem., 80 (1977) 305.

[95] S. Fletcher, D.B. Mathews, J. Applied Electrochem., 11 (1981) 1-6.

[96] R.G. Barradas, F.C. Benson, S. Fletcher and J.D. Porter, J. Electroanal. Chem., 85 (1977) 67.

[97] NAGFLIB : 2076/1839 : Mk. 11 : January 84.

[98] S. Webster, Ph.D. Thesis, Loughborough University of Technology, 1986.

[99] A. Winsel, Z. Elektrochem., 66, 287 (1962).

[100] J. Euler, W. Nonnenmacher, Electrochim. Acta 2, 268 (1960).

[101] J. Euler, Electrochim. Acta 8, 409 (1963).

[102] J.S. Newman, C.W. Tobias, J. Electrochem. Soc., 109, 1183 (1962).

[103] R.C. Alkire, E.A. Grens and C.W. Tobias, J. Electrochem. Soc., 116, 1328 (1969).

[104] J.S. Dunning, D.N. Bennion and J. Newman, J. Electrochem. Soc.,
 118, 1251 (1971).

[105] Z. Nagy and J. O'M. Bockris, J. Electrochem. Soc., 119, 1129 (1972).

[106] R. Alkire and B. Place, J. Electrochem. Soc., 119, 1687 (1972).

[107] E.A. Grens and C.W. Tobias, Ber. Buns. f. Physik. Chem.,
 68, 236 (1964).

[108] D. Simonsson, J. Electrochem. Soc., 120, 151 (1973).

[109] D. Simonsson, J. Appl. Electrochem., 3 (1973) No. 4, 261-270.

[110] idem. ibid., 4 (1974) No.2, 109-115.

[111] L. Lapidus, Digital Computation for Chemical Engineers,
 p. 169, McGraw-Hill, New York, 1962.